

Quantitative measurements of biological/chemical concentrations using smartphone cameras

by
Zhendong Cao

B.A.Sc., Simon Fraser University, 2016

Thesis Submitted in Partial Fulfillment of the
Requirements for the Degree of
Master of Applied Science

in the
School of Engineering Science
Faculty of Applied Science

© Zhendong Cao
SIMON FRASER UNIVERSITY
Fall 2018

Copyright in this work rests with the author. Please ensure that any reproduction or re-use is done in accordance with the relevant national copyright legislation.

Approval

Name: Zhendong Cao
Degree: Master of Applied Science
Title: Quantitative measurements of biological/chemical concentrations using smartphone cameras

Examining Committee: **Chair: Michael Sjoerdsma**
Senior Lecturer

Ash Parameswaran
Senior Supervisor
Professor

Pablo Nepomnaschy
Co-supervisor
Associate Professor
Faculty of Health Science

Glenn Chapman
Internal Examiner
Professor

Date Defended/Approved: November 16, 2018

Abstract

This thesis presents a smartphone-based imaging system capable of quantifying the concentration of an assortment of biological/chemical assay samples. The main goal of this thesis work is to construct an image database which characterizes the relationship between color information and concentrations of the biological/chemical assay sample. For this aim, a designated optical setup combined with image processing and data analyzing techniques was implemented. A series of experiments conducted on selected assays, including fluorescein, RNA Mango, homogenized milk and yeast have demonstrated that our proposed system estimates the concentration of fluorescent materials and colloidal mixtures comparable to currently used commercial and laboratory instruments. Furthermore, by utilizing the camera and computational power of smartphones, eventual development can be directed toward extremely compact, inexpensive and portable analysis and diagnostic systems which will allow experiments and tests to be conducted in remote or impoverished areas.

Keywords: smartphone; image database; image processing; color; fluorescence; scattering;

Acknowledgements

I would like to express much gratitude to my supervisor, Dr. Ash Parameswaran, for giving me the opportunity to explore so many new ideas and projects. Your steady guidance and endless patience throughout many challenges are much appreciated. I would also like to extend my gratitude to Dr. Pablo Nepomnaschy, Dr. Katrina Salvante and Dr. Glenn Chapman for their insight and guidance in fields of biochemistry and engineering optics.

This work could not have been completed without those who laid the foundations for my research and others that offered great assistance along the way. To David Yin, Steven Tseng, Shirley Liu, Katie Tse and the rest members of the Param's research group: Thank you.

Finally, I am grateful to my parents, friends and Jue Wu for your unwavering support and love throughout my studies. I could not have completed this journey without you!

Table of Contents

Approval.....	ii
Abstract.....	iii
Acknowledgements.....	iv
Table of Contents.....	v
List of Tables.....	ix
List of Figures.....	x
List of Acronyms.....	xiii
Chapter 1. Introduction.....	1
1.1. Background.....	1
1.2. Research Objective.....	4
1.3. Outline of the Thesis.....	5
Chapter 2. Literature Review.....	7
2.1. Absorption Spectrophotometry.....	7
2.1.1. Absorption and Scattering of Light.....	7
Absorption.....	7
Scattering.....	8
2.1.2. Spectrophotometer.....	10
2.2. Fluorescence Spectrophotometry.....	11
2.2.1. Fundamental Mechanism.....	11
2.2.2. Fluorescence-based Imaging.....	12
2.2.3. Instrumentation.....	12
2.3. Color-based Imaging.....	14
2.3.1. Color Vision.....	14
Hue, Saturation and Brightness.....	16
2.3.2. Color Models.....	17
RGB Color Model.....	18
HSV Color Model.....	19
Conversion Between Color Models.....	19
2.3.3. Color Space.....	21
2.3.4. Color Depth.....	22
2.3.5. Image Sensors.....	22
Chapter 3. Methodology.....	24
3.1. System Overview.....	24
3.2. Assay Preparation.....	25
3.2.1. Biomaterials and Chemicals.....	25
3.2.2. Serial Dilution.....	25
3.2.3. Sample Container.....	27
3.3. Hardware System.....	29
3.3.1. Light Source.....	29

Light-Emitting Diode (LED).....	29
Power Supply.....	30
LED Illuminance Testing.....	31
3.3.2. System with Minimal Components.....	32
Excitation Setup.....	32
Emission Setup.....	33
3.3.3. Image Detector.....	35
3.3.4. Enclosure Design.....	36
3.4. Data Collection.....	38
3.4.1. Image Datasets.....	38
3.4.2. System Parameters.....	39
Focus.....	39
Exposure Time and ISO Setting.....	40
3.4.3. Temperature.....	41
3.4.4. Assay Samples.....	42
3.5. Image Processing.....	42
3.5.1. Flowchart.....	42
3.5.2. Image Cropping.....	43
3.5.3. Noise Reduction.....	44
3.5.4. Locating the Region of Interest.....	45
3.5.5. Measurement Approaches.....	47
Approach 1: Ratio of Two Color Channels.....	47
Approach 2: Grey Scale Measurement.....	48
3.5.6. Data Analyzer.....	49
Detection limit.....	50
Sensitivity.....	50
Repeatability or Repetition Error.....	51
Measurement Error.....	51
3.6. Image Database.....	52
Chapter 4. Fluorescence-based Measurements.....	53
4.1. Fluorescein.....	53
4.1.1. Properties of Fluorescein.....	53
4.1.2. Experimental Setup.....	54
Sample Preparation.....	54
Hardware Setup.....	56
4.1.3. Image Acquisition Procedures.....	57
4.1.4. Image Processing Results.....	60
4.1.5. Data Analysis.....	64
4.1.6. Error Analysis.....	65
Light Source.....	65
Camera Focusing.....	66
Pipetting Errors.....	67
4.1.7. Image Database for Fluorescein.....	67

Input Condition:.....	68
Measurement Data:.....	68
Output Results:	68
4.1.8. Comparison	69
4.2. RNA Mango.....	71
4.2.1. RNA Mango Properties.....	71
4.2.2. Experimental Setup	73
4.2.3. Experimental Results.....	74
4.2.4. Comparison	76
4.3. Summary.....	77
Chapter 5. Scattering-based Measurements	78
5.1. Methods	78
5.1.1. Types of Mixtures	78
5.1.2. Light Interactions with Colloidal mixtures	79
5.1.3. Quantification Methods	80
Measuring the concentrations of biological samples by Absorbance	80
Measuring the concentrations of biological samples using our Imaging System.....	81
5.2. Homogenized Milk	82
5.2.1. Material Properties	82
5.2.2. Experimental Setup	83
Sample Preparation	83
5.2.3. Experimental Results.....	83
Measurements using a Spectrometer.....	83
Measurements using our Imaging System	84
Measurements using a Power Meter	86
5.2.4. Comparison	87
5.3. Saccharomyces Cerevisiae	88
5.3.1. Material Properties	88
5.3.2. Experimental Setup	89
5.3.3. Experimental Results.....	90
5.3.4. Comparison	92
5.4. Summary.....	93
Chapter 6. Conclusion and Future Work	95
6.1. Conclusion.....	95
6.2. Future Work.....	96
Appendix A. Designing a Microplate-based Imaging System.....	104
Appendix B. Determining the Optimized System Parameters for Image Acquisitions.....	107
Appendix C. Calibration of Spectral Sensitivity of iPhone 6	110
Experimental Setup:.....	111

Appendix D. Design of Automated Smartphone Imaging System..... 114

List of Tables

Table 3-1: Optical parameters of some popular smartphone cameras.....	35
Table 3-2: Fluorescence quantum yield of several chemicals.....	42
Table 3-3 [37]: Conversion from monochromatic light to RGB values.....	47
Table 4-1: Serial dilution table of fluorescein.....	55
Table 4-2: Description of each part in Figure 4.4.....	57
Table 4-3: Results summary of two measurement approaches (Fluorescein).....	64
Table 4-4: Plate reader measurement results at different exposure times (Fluorescein)	70
Table 4-5: Molarities of each serially diluted RNA Mango sample.....	73
Table 4-6: Illustration of each part in Figure 4.17.....	74
Table 4-7: Results summary of two measurement approaches (RNA Mango).....	76
Table 5-1: Physical properties of solution, colloid and suspension.....	78
Table 5-2: Concentrations of serially diluted homogenized milk samples.....	83
Table 5-3: Results compared by two measurement approaches (2% Milk).....	86
Table 5-4: Measurement results obtained by powermeter (2% Milk).....	87
Table 5-5: Concentration of serially diluted yeast samples.....	90
Table 5-6: Results compared by two measurement approaches (Yeast).....	91
Table 5-7: Measurement results obtained by powermeter (Yeast).....	92

List of Figures

Figure 1.1: Schematic of a typical plate reader.....	2
Figure 1.2: Schematic of a typical spectrophotometer.	3
Figure 2.1: Patterns of Rayleigh scattering and Mie scattering.	9
Figure 2.2: Schematic diagram of a typical spectrophotometer.	10
Figure 2.3 [12]: A simplified Jablonski diagram showing the transition of states of electrons during fluorescence process	11
Figure 2.4 [13]: Overview of a commercial fluorometer.....	13
Figure 2.5: Overview of a commercial plate reader	13
Figure 2.6: Visible portion of the electromagnetic spectrum.....	15
Figure 2.7 [16]: Normalized human retina cone response at each wavelength	15
Figure 2.8: Defining hue, saturation and brightness from the spectrum of light.....	17
Figure 2.9: RGB color model in Cubic coordinates	18
Figure 2.10: HSV color model in hexcone coordinates	19
Figure 2.11: CIE 1931 color space and the definition of some popular color spaces, including sRGB, Adobe RGB, ProPhoto RGB.....	21
Figure 2.12: Response to illuminance of digital image sensors	23
Figure 3.1: Engineering model of the entire system.....	24
Figure 3.2: Diluting a 0.1M fluorescein solution using 10 fold series.....	26
Figure 3.3 [21]: Transmission curves of cuvettes made from different types of materials	27
Figure 3.4: Polystyrene 96 well microplate	28
Figure 3.5: Spectrum plot of selected LEDs	30
Figure 3.6: Portable DC power supply	30
Figure 3.7: LED irradiance measurement setup	31
Figure 3.8: Standard deviation plot of the RGB pixel values measured from ten images	32
Figure 3.9: 405nm Laser diode excitation and fluorescence emission spectrums.....	34
Figure 3.10: 482nm cyan LED excitation and fluorescence emission spectrum.....	35
Figure 3.11: CAD model of the enclosure design	37
Figure 3.12: Geometry of the layout setup.....	37
Figure 3.13: Top view of the enclosure box	38
Figure 3.14: Process of acquiring image data.....	39
Figure 3.15 [33]: Illustration of the composition of a smartphone camera	40
Figure 3.16: Image processing flowchart	43
Figure 3.17: Calculation of the cropped image area	44
Figure 3.18: Region of interest from the cropped image	46
Figure 3.19 [39]: Emission spectrum of fluorescein	48

Figure 3.20: Illustration of repetition error, sensitivity, measurement error and detection limit	50
Figure 4.1 [38]: Excitation and emission spectrum of fluorescein	53
Figure 4.2 [40]: Emission spectrum of fluorescein at various temperatures	54
Figure 4.3 [41]: Fluorescence intensity of fluorescein at high concentrations, 1% corresponds to 3.8mM.....	55
Figure 4.4: Hardware setup for smartphone based fluorescence measurement	56
Figure 4.5: Variation of the signal when focusing at different spots in the middle dark region.....	58
Figure 4.6: Images acquired at different exposure time while keeping other conditions identical.....	59
Figure 4.7: Interface of ImageJ showing the selection of ROI and calculation of the average pixel values in this region	60
Figure 4.8: G/B ratio vs. molarity at 22°C.....	61
Figure 4.9: Gray scale value vs. molarity at 22°C	61
Figure 4.10: Results at 10uM and 100uM obtained from both our system and spectrometer	63
Figure 4.11: Fluorescence intensity at different temperatures, measured by G/B ratio (Fluorescein).....	63
Figure 4.12: Fluorescence intensity at different temperatures, measured by grey scale value (Fluorescein).....	64
Figure 4.13: Serially diluted fluorescein sample prepared in 96 well plate	69
Figure 4.14: Measurement results of the fluorescein test using a VICTOR X5 plate reader	70
Figure 4.15: Comparison of response curves of the smartphone based system and commercial platereader.....	71
Figure 4.16: Absorption and emission spectrum of RNA Mango.....	72
Figure 4.17: Hardware setup for RNA Mango experiment; each part is labeled and explained in Table	74
Figure 4.18: Detected image of a 500nM RNA Mango sample	74
Figure 4.19: G/B ratio vs. molarity measured at 22°C (RNA Mango)	75
Figure 4.20: Grey scale value vs. molarity measured at 22°C (RNA Mango).....	75
Figure 4.21: Comparison of response curves of the smartphone based system and spectrophotometer	76
Figure 5.1 [44]: Scattering effects of milk at different concentrations	79
Figure 5.2 [47]: Phases in a bacterial culture measured with OD	81
Figure 5.3 [50]: Microscopic view of fat particles in homogenized milk	82
Figure 5.4: Scattered light spectrum of homogenized milk at 0.125% and 2%.....	84
Figure 5.5: G/B ratio vs fat concentrations of milk, measured at 22°C (2% Milk).....	85
Figure 5.6: Grey scale value vs fat concentration of milk, measured at 22°C (2% Milk) .	85
Figure 5.7: Optical density vs fat concentration of milk measured by powermeter	87

Figure 5.8: Comparison of response curves of the smartphone based system and power meter (fat concentration in homogenized milk)	87
Figure 5.9 [52]: <i>Saccharomyces cerevisiae</i> under electronic microscope	88
Figure 5.10 [54]: Typical yeast growth curve, measured by absorbance at 600nm red laser beam	89
Figure 5.11: G/B ratio vs. concentration, measured at 22°C (Yeast).....	91
Figure 5.12: Grey scale value vs. concentration, measured at 22°C (Yeast)	91
Figure 5.13: OD vs concentration, measured at 22°C.....	92
Figure 5.14: Comparison of response curves of the smartphone based system and power meter (yeast)	93

List of Acronyms

CAD	Computer-aided Design
CCD	Charge Coupled Device
CIE	Commission Internationale e l'éclairage
CMOS	Complementary Metal-oxide Semiconductor
PMT	Photo-multiplier Tube
OD	Optical Density
DSLR	Digital Single-lens Reflex
FOV	Field of View
FWHM	Full Wave Half Maximum
GFP	Green Fluorescence Protein
ISO	International Organization for Standardization
LED	Light Emitting Diode
ROI	Region of Interest
UV	Ultraviolet

Chapter 1.

Introduction

1.1. Background

The development of smart phones in recent years have rapidly transformed the way we interact with the physical world and communicate with other people. Advancements in integrated circuit technology have also substantially increased smartphones' computational power and memory, making it possible to integrate different functionalities on a single smartphone. For example, the complementary metal-oxide semiconductor (CMOS) image sensors on smartphones have met the needs of acquiring high definition images. Nowadays, smart phones have led a large consumerism market. Ericsson Mobility Report shows that worldwide smart phone subscriptions had reached 3.9 billion in 2016 and are expected to hit 6.8 billion by 2022 [1] (compared to world population estimates of 7.9 billion by 2022). These numbers suggest that smart phones are widely popular and are becoming a must-have item for almost every person.

With applications extending across communication, photography, computation and health care, the possibilities offered by smart phones seem endless. The demand for associated products and applications is growing continuously. The use of smart phones for digital imaging is a good example. The rapid improvement in quality and light sensitivity of CMOS sensors in smart phones, combined with the low-power high performance processor with the capability of performing complex computations [2], have extended imaging capabilities of phone cameras from simple or leisure photoshoots to biological and medical imaging applications. Research has shown that, by equipping them with a well-designed portable microscopy platform, smartphones are able to detect and analyze the fluorescence images associated with a number of bio-markers ranging from viruses to molecules [3], [4]. These findings have inspired the use of phones as the primary imaging system for several new biomedical applications.

In the life sciences, biological samples are collected in order to measure the concentrations of various compounds of interest, including hormones, proteins, and enzymes. To quantify the compounds of interest, two types of common detection methods are adopted by different types of analytical laboratory instruments. The first detection method is based on fluorescence and the second method is based on absorption. In terms of the typical fluorescence-based microplate reader, it detects biological or chemical markers within samples placed in microplates based on fluorescent signals emitted by these markers [5]. Figure 1.1 shows the diagram of a typical fluorescence-based microplate reader system. A standard 96-well plate is used for preparing diluted fluorophore assays and will be placed into the plate reader. The instrument usually contains a spatial translation stage to control the movement of the optical system. The optical system includes a special light source for illumination, lens for reshaping beam path, filters or monochromators to select appropriate wavelengths and a photo-multiplier tube (PMT) to amplify the intensity of the emitted light. The analog output of the PMT will be converted to digital signals and sent to a computer for further analysis.

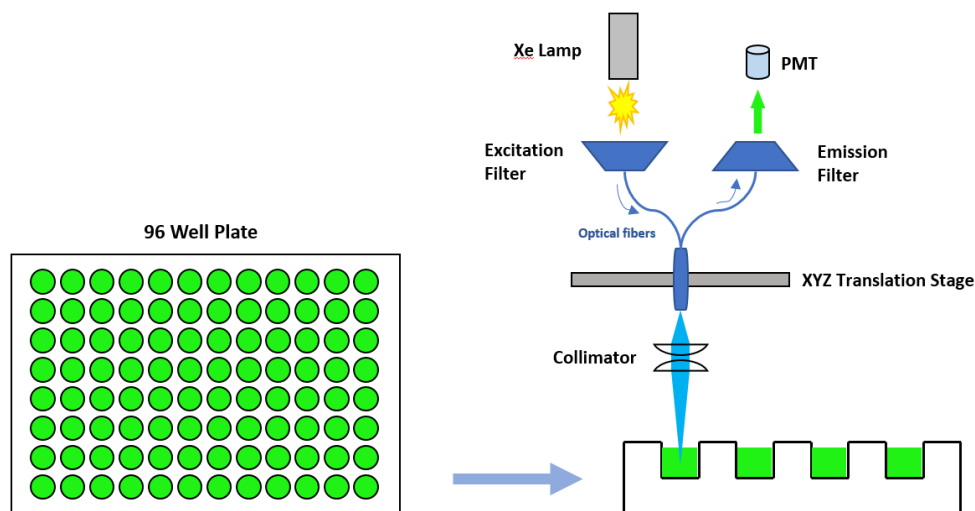
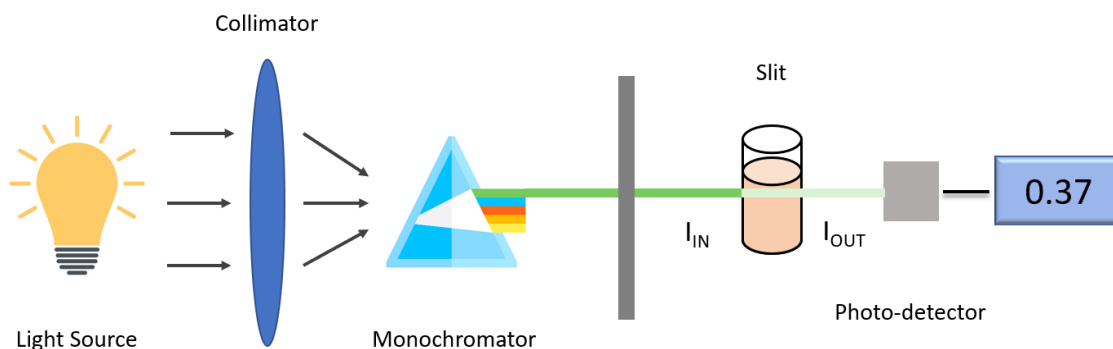


Figure 1.1: Schematic of a typical plate reader

The second well-known instrument in life sciences laboratories is based on absorbance readings. (Figure 1.2.). Specifically, a spectrophotometer measures the absorbance of light intensity when light passes through the sample solution. The monochromator, which is made from a prism or grating, splits the light into beams of

differentiated wavelengths; the desired range of wavelengths can be captured by adjusting the aperture to allow only select beams to pass through the slit. Output light intensity is monitored by placing a photocell detector along the path where photons exit the sample cuvette. The ratio between output and input light intensities characterizes the optical density (O.D.) of the sample.



Using a monochromator which splits wavelength of the light source, the optical system of the spectrometer generates monochromatic light with specific wavelength and intensity I_{IN} , which incidents to the compound of interest and exits with the same wavelength but attenuated intensity I_{OUT} . Output reading is the optical density of the compound of interest ranges from 0 to 1, and higher value indicates a strong absorption of the compound of interest at the given wavelength.

Figure 1.2: Schematic of a typical spectrophotometer.

Fluorescence-based microplate readers have impressively high sensitivity and specificity in terms of their detection capability. For instance, the Victor 3 plate reader developed by PerkinElmer can detect and quantify the fluorescence of fluorescein with concentrations in pico-molar or even lower range, which makes the device suitable for applications such as DNA, RNA and protein quantification [6]. Absorbance-based spectrophotometers are less sensitive than fluorescence-based instruments. Measuring with O.D. does not discriminate between the sample of interest and contaminants that absorb wave of the same length. However, with less mechanically moving parts, absorbance-based spectrophotometry devices are easier to use and require minimal maintenance to keep devices running smoothly [7].

Even though these instruments are designed to be highly sensitive and accurate, they sacrifice portability, and their costs are also very high. A standard microplate reader occupies about half of an office table, and it needs a computer and wall AC power for

operation. Moreover, the price of a brand-new machine can easily exceed \$30,000. Therefore, such instruments are usually placed and maintained in laboratory environments or research centers but are extremely unlikely to be used in field applications, remote areas or economically impoverished environments.

Compared to any standard spectrophotometer or plate reader used in laboratories, a smart phone-based detection and analysis system will have numerous advantages in terms of device portability, cost and ease of operation. The entire system can be extremely compact, inexpensive and battery powered. The smart phone itself can serve as a computing station for data analysis and, thus, a separate computer is no longer needed. With a phone-based detection and analysis system, quantitative measurements of several biological samples can be performed in an easier and cheaper way, allowing researchers to conduct biological experiments in the field or remote areas. Therefore, the development of a phone-based system to quantify compounds of interest and a comprehensive comparison between such a system and existing commercially-available instruments will be the major focus of this research.

1.2. Research Objective

The overall objective of this research is to investigate the performance of a smart phone-based system for quantitative measurements of bio/chemical samples when the full hardware and software potentials of the smart phone are utilized. Specific objectives include:

- To survey the different types of bio/chemical compounds and samples that can be detected and quantified by this system
- To evaluate the engineering performance of the system including detection limit, sensitivity, precision and accuracy
- To investigate the possibility of design modifications for reducing cost and enhancing performance
- To explore applications in which the advantages of this system can be best utilized

To achieve these objectives, I conducted a study of the validity and practicality of the measurement results obtained from various customized smart phone-based biomedical imaging and analysis models. Keeping in mind the importance of maintaining the system's low cost, portability and compactness to enhance usability in the field and remote areas, effort was focused on establishing experiment models and determining optimal points engineering performance, popularity and adaptability to various sites and situations.

1.3. Outline of the Thesis

The thesis is structured in six chapters. Chapter one provides an introduction. Chapter two reviews the theoretical background and engineering mechanism of conventional fluorescence-based and absorbance-based imaging systems. Also discussed are the significance, advantages and potential limitations of the two imaging systems using the standard instruments used in most life sciences labs, the microplate reader and the spectrophotometer, as examples. The approach of imaging and quantifying biological/chemical compounds using RGB color space will also be illustrated in this chapter.

Chapter three describes the systematic approach of developing a smart phone-based imaging and analysis system for biological applications, in general. Methods employed in the current work, including the establishment of theoretical models, design of the optical system, preparation of bio/chemical assays, setup of hardware apparatus, acquisition and processing of image data and validation of experimental results will be presented in detail.

Chapter four and chapter five present the experimental work. Chapter four focuses on fluorescence-based measurements whereas chapter five will be on absorption-based measurements. The implementation and methods of the experiments and the outcome results will be presented in detail. Furthermore, the compatibility and engineering performance of our system on each application will be summarized at the end of each chapter. The first three objectives proposed in the Research Objective section (Section 1.2) will also be addressed.

Chapter six draws conclusions of this research. The possibility of the further enhancement of the system will also be discussed to address the final research objective outlined in Section 1.2.

Chapter 2.

Literature Review

This chapter reviews two methods that are commonly used in life science, microbiology and chemistry for quantitative measurements of compounds of interest, including hormones, proteins and enzymes, in different types of samples, including serum, plasma, urine, saliva, water and cell culture media. I will first review the absorption-based method and then the fluorescence-based spectrophotometry methods. This chapter will also discuss color theory and, investigate the possibility of using colors as an alternative approach for quantification of some biomaterials. The potential challenges, advantages and limitations of the color-based approach in comparison with the spectroscopy-based approaches mentioned above will be addressed.

2.1. Absorption Spectrophotometry

Spectrophotometry is a useful method to quantitatively measure the concentrations of compounds of interest based on the amount of light they absorb when a beam of light at certain wavelength passes through the sample. In this section, we will review some fundamental topics of spectroscopy including absorption and scattering of light and the mathematical model developed for quantifying absorption and scattering. The principle and mechanism of a standard spectrophotometer and its applications in biological and chemical fields are also reviewed.

2.1.1. Absorption and Scattering of Light

Absorption

Absorption and scattering are two phenomena that can occur when photons or electromagnetic waves interact with a matter. Absorption takes place when the energy of a photon is taken in and transformed into the internal energy of the material with which it is interacting. According to the Beer-Lambert Law [8], the absorbance is proportional to the concentrations of the attenuating compounds in the sample, therefore the concentration of

the compound within the sample can be quantitatively determined by measuring the absorbance or optical density of the sample. Assuming the predominant mechanism of interaction with a sample is absorption without scattering, when a monochromatic light, which contains only a single wavelength enters into the sample from one side, the intensity of the transmitted light detected from the other side (output) can be expressed as,

$$I(\lambda) = I_0 e^{-\mu_a(\lambda) \cdot z} \quad (1)$$

where

I_0 is the intensity of the incident monochromatic light

$\mu_a(\lambda)$ is the absorption coefficient of the sample that is wavelength dependent

z is the distance penetrated by the incident light.

From equation (1), absorption factor will become a constant value and therefore the absorbance A at a certain wavelength is given by:

$$A = \log_{10} \frac{I(\lambda)}{I_0} = \log_{10}(e^{-\mu_a \cdot z}) \quad (2)$$

In microbiology, monitoring the absorbance of growing cultures is a common method to quantify various important culture parameters like cell concentration, biomass production or changes in the cell morphology [9].

Scattering

The phenomenon of scattering occurs when the straight trajectory of light particles is deviated due to the distribution and geometry of particles within the sample. Two types of scattering are classified based on the change in photon energy. If the photon energy remains the same before and after it passes through the sample, the scattering is referred as elastic scattering. In contrast, inelastic scattering occurs when a portion of the photon energy is absorbed by the sample, causing a change in energy level of the exiting photons [10]. In this chapter, inelastic scattering will not be reviewed since it is beyond the scope of this research.

Depending on the geometry of the scattered particles, elastic scattering can also be classified into two sub-types: Rayleigh and Mie scattering. Rayleigh scattering describes scattering from molecules and tiny spherical particles whose diameters are much smaller than the wavelength of visible light. The scattered intensity measured on the output side of the sample along the incident light beam is calculated by [11]:

$$I = I_0 \frac{8\pi^4 N \alpha^2}{\lambda^4 R^2} (1 + \cos^2 \theta) \quad (3)$$

where

I_0 is the intensity of the incident light

N is the number of scatters

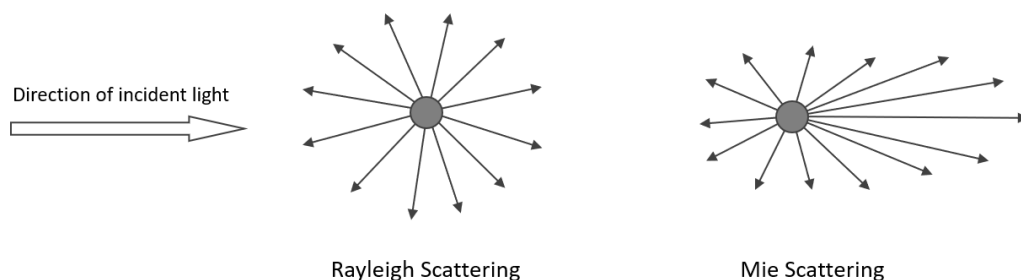
α is the polarizability

λ is the wavelength

R is the distance between the scatterer and observer

θ is the scattering angle.

The Rayleigh scattering model becomes invalid when the scattering particles become larger than approximately 1/10 of the wavelength of the incident light. In this situation, the Mie scattering model predominates. As illustrated in Figure 2.1, Mie scattering produces a pattern with a sharper and more intense forward lobe for larger particles.



The scattered light of Rayleigh scattering is uniformly distributed in radial outwards direction whereas it is more concentrated in direction of incident light for Mie scattering

Figure 2.1: Patterns of Rayleigh scattering and Mie scattering.

2.1.2. Spectrophotometer

A spectrophotometer is an instrument that quantifies the concentration of compounds based on the absorption of the sample in which they are contained. The absorbance of the sample at each wavelength is measured by the wavelength selection mechanism of the machine.

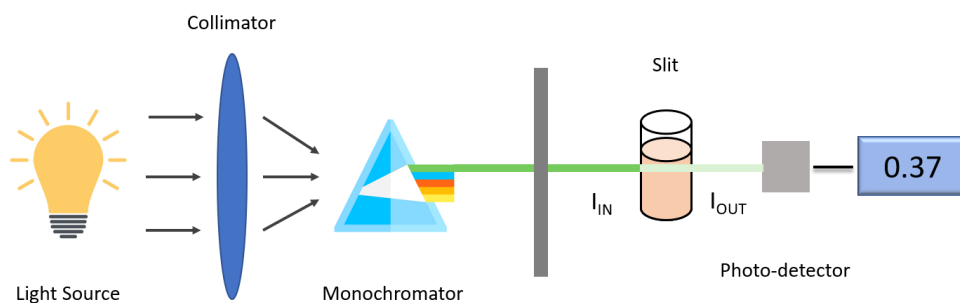


Figure identical to Figure 1.2, and is reproduced here for simplicity of reading

Figure 2.2: Schematic diagram of a typical spectrophotometer.

Referring to the schematic diagram in Figure 2.2, a lens with appropriate focal length is used to collimate the light source into a straight and parallel beam which, once passed through the monochromator, will be split into differentiated wavelengths or colours. Only the desired wavelength can traverse through the wavelength selection slit and react with the sample solution in the cuvette. A photodetector is placed on the other side of the cuvette to measure the light intensity exiting from the cuvette. The absorbance of the sample can then be measured using equation 2, once the intensities of the input light and output light are known.

This wavelength selection mechanism eliminates the wavelength dependence of the absorption coefficient, thus allowing a precise measurement of absorbance at each wavelength. To establish a profile of the absorbance of the sample at different wavelengths, a wavelength selection slit on a moveable mechanical platform is usually installed with small step-size tuning.

2.2. Fluorescence Spectrophotometry

2.2.1. Fundamental Mechanism

Fluorescence occurs when a specimen absorbs radiation (light) at one wavelength and subsequently emits light at a different wavelength. The mechanism of photon absorption and reemission can be explained by the Jablonski diagram as shown in Figure 2.3. At room temperature, most molecules occupy the lowest energy level of the ground state S_0 . Once sufficient energy from incident photons is absorbed, these molecules are elevated to the vibrational levels of second excited state S_2 . Molecules at this higher vibrational level of excited states lose their excess energy rapidly until they reach the excited state S_1 . From S_1 , molecules relax from excitation and fall back to the ground state S_0 , emitting their energy in the form of fluorescence.

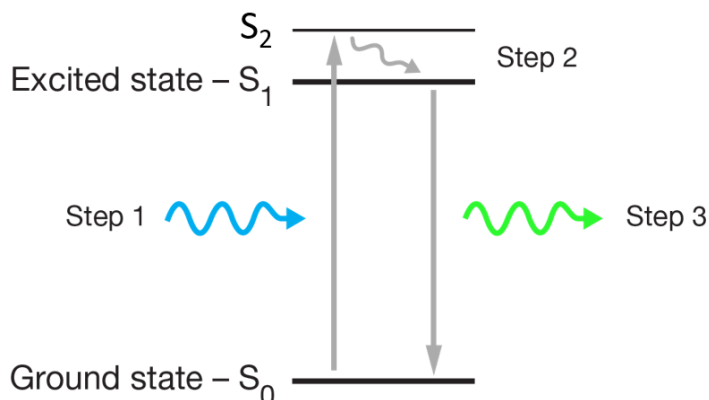


Figure 2.3 [12]: A simplified Jablonski diagram showing the transition of states of electrons during fluorescence process

Fluorescence emission takes place immediately after the absorption of the excitation light, usually in the range of nano seconds. The emitted photons have longer wavelengths compared to the excitation photons. The difference in the wavelengths at maximum spectral intensities between emission and excitation is known as the *stoke shift*. The *stoke shift*, which usually ranges from 10nm to 50nm, allows the fluorescent object to be distinguished and detected.

2.2.2. Fluorescence-based Imaging

The essential task of almost any fluorescence-based measurement is to separate the weaker emitted light from the excitation light. Only the emission light should reach the signal detector for further processing and analysis.

To excite the specimen, a typical fluorescence-based spectroscopy system uses a monochromator to obtain the desired excitation wavelength. Compared to a laser, which only provides monochromatic light at one specific wavelength, e.g., 462nm, 472nm, 488nm, or 520nm, a wavelength selection system with monochromator can precisely tune the excitation light to the specific wavelength at which the sample maximally absorbs the excitation radiation. Following the same logic, another monochromator is placed at the output emission side to selectively allow only the desired emission wavelength to reach the photo detector.

Though monochromators are very precise in terms of wavelength selection, they are expensive and bulky. Alternatively, some more cost effective instruments use optical filters as substitutes. To isolate a particular wavelength from a light source, a pair of sharp-edge-filters are required. The emission filter must be chosen to have a bandwidth that will allow the specific emission wavelength to pass through and attenuate all the remaining wavelengths.

2.2.3. Instrumentation

Two typical instruments used in spectrophotometry are fluorometers and microplate readers, which have distinctive photometry mechanisms. In a fluorometer, the sample solution is often prepared in a highly transparent cuvette. The excitation light source is placed orthogonal to the detection mechanism to minimize the noise from the input (excitation) light, as shown in Figure 2.4. The path length of a cuvette is typically standardized to 1cm.

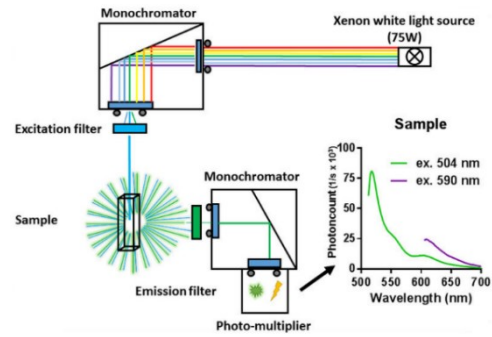
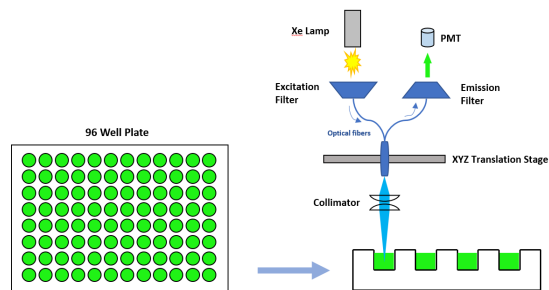


Figure 2.4 [13]: Overview of a commercial fluorometer

On the other hand, plate readers use microplates (transparent plastic plates containing small sample wells, often ranging from 6 to 384 wells) as the sample assay containing platform. A standard microplate reader and its photometry mechanism can be seen in Figure 2.5. For each measurement, light is directed through each well vertically from the bottom, and the detection mechanism is placed above the plate. In this setup, the path length in a microplate well is dependent on sample volume.



A commercial platereader is equipped with a translation stage allowing the optical system reads the information of each well of the test plate.

Figure 2.5: Overview of a commercial plate reader

Another alternative interpretation of Beer-Lambert's Law declares that the absorbance (A) of a material is determined by the equation [14]:

$$A = \epsilon bC \tag{4}$$

where

ϵ is the molar absorptivity,

b is the path length

C is the concentration of the sample solution.

Consequently, the measurement result for an identical solution in a cuvette-based fluorometer could be different from a microplate because of the difference in path length. Due to their design, microplate readers are typically used to quantify fluorescence intensity for a large number of samples in a single experiment. On the other hand, fluorometers use monochromators, which select wavelengths more freely and precisely compared to filters. Therefore, the precision and specificity of fluorometers for molecular detection is extremely high.

2.3. Color-based Imaging

Recognition and interpretation of colors play a vital role in establishment of humans' visualization system. The physics behind colors may carry tremendous information that reflects the properties of an object. There are many situations where people perceive an object by its color. However, the process of interpreting colors within the human brain is highly subjective and less accurate. For applications wherein higher accuracy and consistency are required, the process of color interpretation/determination needs be further refined by a well-established digital imaging system where appropriate color models, color space and image sensors are used.

2.3.1. Color Vision

Light, or the visible portion of the electromagnetic wave that lies within 380nm to 780nm, can be described using colors. As shown in Figure 2.6, colors in this visible range can be roughly categorized as violet, blue, cyan, green yellow, orange and red. The spectrum of colors outside the visible range are referred to as black, and the sum of all possible colors appear as white light.

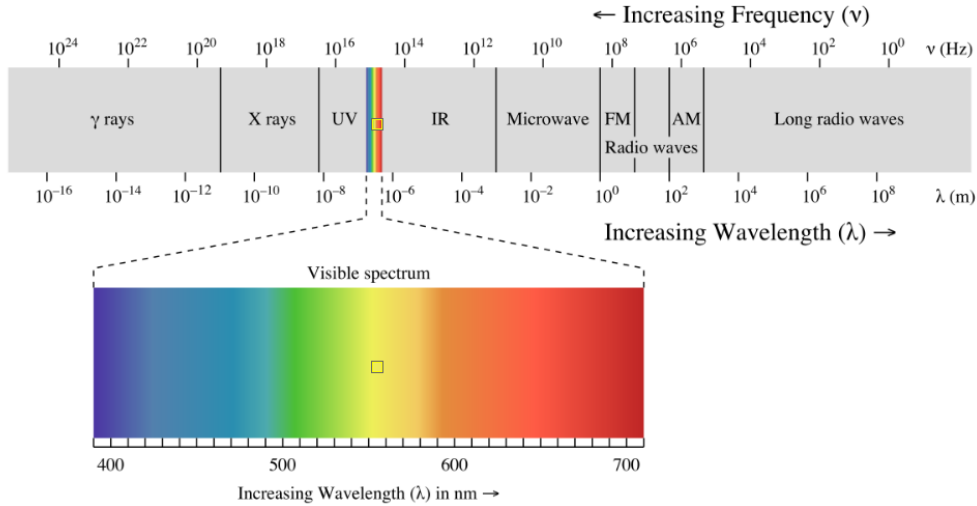
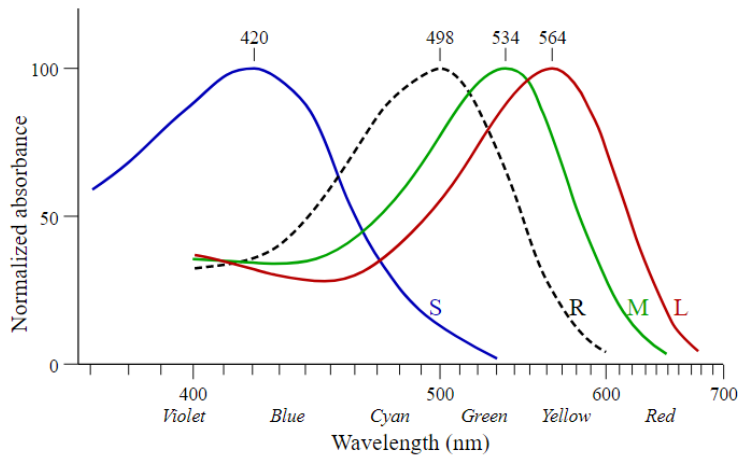


Figure 2.6: Visible portion of the electromagnetic spectrum

The perception of color is derived from the stimulation of photoreceptor cells known as cones and rods in the retina of the human eye. Three types of cones are identified according to their spectral sensitivities: short (S), medium (M) and long (L) types [15]. As shown in Figure 2.7, these cones sense color using three broad bands that roughly correspond to blue, green and red, respectively.



Blue, green and red curve are the response curve of cones for short, medium and long types respectively. And the black dotted curve is human's retina response curve based on the overall effects of the cones; thus humans' retina is most sensitive to wavelength around 500nm, which is green color.

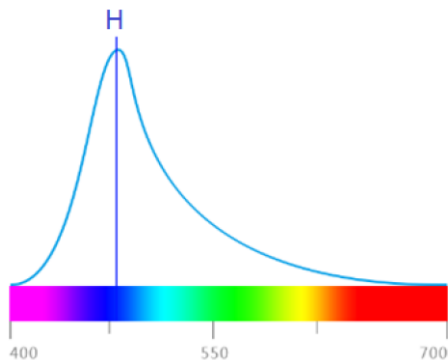
Figure 2.7 [16]: Normalized human retina cone response at each wavelength

Color can be categorized as monochromatic or polychromatic. A monochromatic color is the interpretation of only a single wavelength of light, whereas polychromatic color is the mixture of multiple wavelengths. When we see a color, the image received by our brain is the resultant combination of the responses from the three cones of our retina. This sensing mechanism allows us to perceive millions of different colors; however, our retinas cannot distinguish between monochromatic and polychromatic colors.

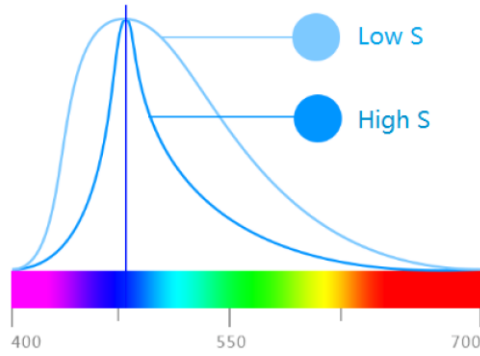
Hue, Saturation and Brightness

Humans' recognition of colors is largely built on the perception of three important properties of color: hue, saturation and brightness. Literally, hue is the major property of color in which people can instantly tell whether the color they see is red, yellow, green or blue. Saturation refers to the density or thickness of a color. The color of fountain pen ink, for example, is highly saturated, while adding water will reduce its saturation. Brightness is essentially related to the varying of magnitudes of light spectrum.

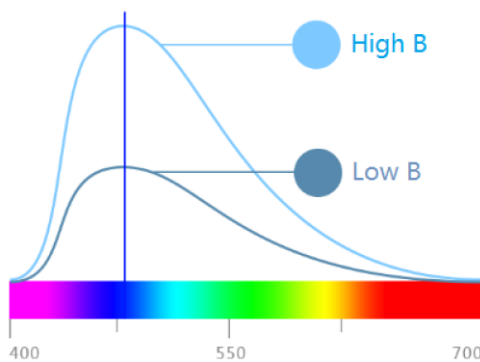
A quantitative definition of Hue, Saturation and Brightness using light spectrum is illustrated by the three graphs in Figure 2.8. Any color we see, either monochromatic or polychromatic, is due to the reflected photons within visible wavelengths that are received by our eyes, hence we can always define a color from the light spectrum.



(a) Hue is defined at the position at which the spectrum of light reaches to maximum



(b) Saturation is determined by the bandwidth of the light spectrum, with more narrow bandwidth corresponding to higher saturation



(c) Brightness is determined by the magnitude of the light spectrum

Figure 2.8: Defining hue, saturation and brightness from the spectrum of light

2.3.2. Color Models

Humans' perception of color can be highly subjective and personal. It is postulated that people have different brain reactions to specific visual stimuli, thus different people may see the same illuminated object or light source in different ways. To represent colors in a precise and reproducible manner, color models have been developed to precisely define and quantify colors. A color model is an abstract numerical system for describing color using a combination of three main basic colors known as the primary colors.

Various color models have been developed for specific applications. As humans, we may define a color by its Brightness, Hue and Colourfulness. A computer may recognize a color based on Red, Green and Blue channels [17]. There is no doubt that each color space has its own advantages and drawbacks for different applications. For brevity,

in this chapter, we emphasize two popular color models, the RGB color model and the HSV color model, that are particularly relevant for this research.

RGB Color Model

The most famous RGB color model is an additive color model with three primary colors: Red (R), Green (G) and Blue (B). This model is based on the theory that all visible colors can be created from the linear combination of R, G, and B. Mathematically, the RGB color model can be fully defined by a three-dimensional Cartesian cube as shown in Figure 2.9.

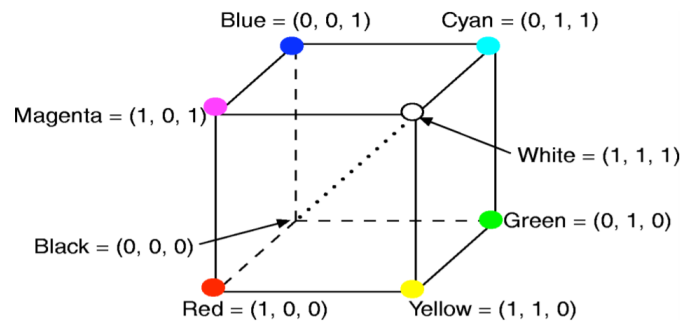


Figure 2.9: RGB color model in Cubic coordinates

In the normalized Cartesian coordinate system, the three primary colors Red, Green and Blue are located at the end position on each axis. The other common colors, such as magenta, yellow, and cyan can be found on the other four endpoints of the cube. The main diagonal maps to the values in gray scale. Additionally, Black is defined when none of the primary color components are present and white is defined when all the primary color components reach to maximum value.

The RGB color model is the prevalent choice for computer graphics because the machine interprets the desired color by simply adding the portions from each primary color channel. That is, any point within the Cartesian cube in Figure 2.9 can be easily and quickly located once the R,G,B values are given. However, dealing with “real world” images with the RGB system is not very efficient. For example, it is difficult for a common person to perceive that [RGB: 1, 0.5, 1] is pink, and it is even more difficult when they are presented with [RGB: 0.3, 0.7, 0.4] (which happens to be green).

HSV Color Model

A more intuitive color model that was developed to approximate the way humans perceive and interpret colors is the HSV color model, where H, S and V stand for Hue, Saturation and Value (which is the same as Brightness). There are also alternative examples to HSV including HSL (lightness) and HIS (intensity). A graphical illustration of the HSV model is given in Figure 2.10.

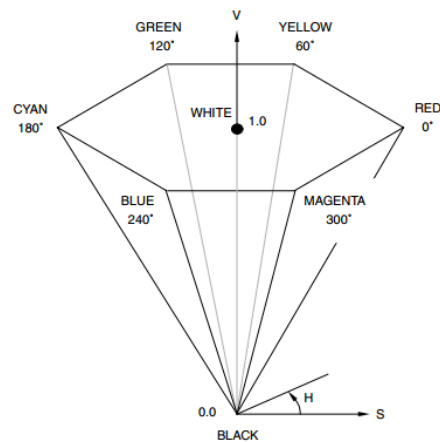


Figure 2.10: HSV color model in hexcone coordinates

With this color model, we can easily tell the main color of the object based on Hue (H) value. The other two channels, Saturation and Value determine the how deep and bright the color appears to be. For example, [HSV: 240°, 100%, 100%] indicates the color is a deep and bright blue, while [HSV: 90°, 70%, 30%] represents a green-yellowish color that is less dense and relatively dark, which easily relates to a dark green color.

Conversion Between Color Models

Mathematically, the RGB color model can be transformed to the HSV color model and vice-versa. To transfer the color [RGB: R, G, B] to HSV, the process is given by:

$$C_{\max} = \max(R, G, B)$$

$$C_{\min} = \min(R, G, B)$$

$$\Delta = C_{\max} - C_{\min}$$

Hue (H) Calculation:

$$H = \begin{cases} 0 & \text{if } C_{\max} = 0 \\ \left(60 \times \frac{G - B}{\Delta} + 360\right) \bmod\% 360 & \text{if } R = C_{\max} \\ 60 \times \frac{B - R}{\Delta} + 120 & \text{if } G = C_{\max} \\ 60 \times \frac{R - G}{\Delta} + 240 & \text{if } B = C_{\max} \end{cases}$$

Saturation (S) Calculation:

$$S = \begin{cases} 0 & , & C_{\max} = 0 \\ \frac{\Delta}{C_{\max}} & , & C_{\max} \neq 0 \end{cases}$$

Value (V) or Brightness Calculation:

$$V = C_{\max}$$

And the process of converting [HSV: H, S, V] where $0 \leq H \leq 360$, $0 \leq S \leq 1$ and $0 \leq V \leq 1$ to RGB color model is given as:

$$C = V \times S$$

$$X = C \times \left(1 - \left| \left(\frac{H}{60} \right) \bmod\% 2 - 1 \right| \right)$$

$$m = V - C$$

$$(R', G', B') = \begin{cases} (C, X, 0), & 0 \leq H < 60 \\ (X, C, 0), & 60 \leq H < 120 \\ (0, C, X), & 120 \leq H < 180 \\ (0, X, C), & 180 \leq H < 240 \\ (X, 0, C), & 240 \leq H < 300 \\ (C, 0, X), & 300 \leq H < 360 \end{cases}$$

$$(R, G, B) = ((R' + m), (G' + m), (B' + m))$$

2.3.3. Color Space

While color model is a mathematical description of how a color is defined in a coordinate system, it does not indicate what the actual color is. For example, by giving [RGB: 100%, 0,0], we know this color only contains the primary color red, but we do not know its exact redness unless we are given its color space. Color space is the implementation of a color model based on the Commission internationale de l'éclairage (CIE) standard. The famous color space system developed by CIE in 1931, the color shaded area as shown in Figure 2.11, classifies colors based on the human visual system.

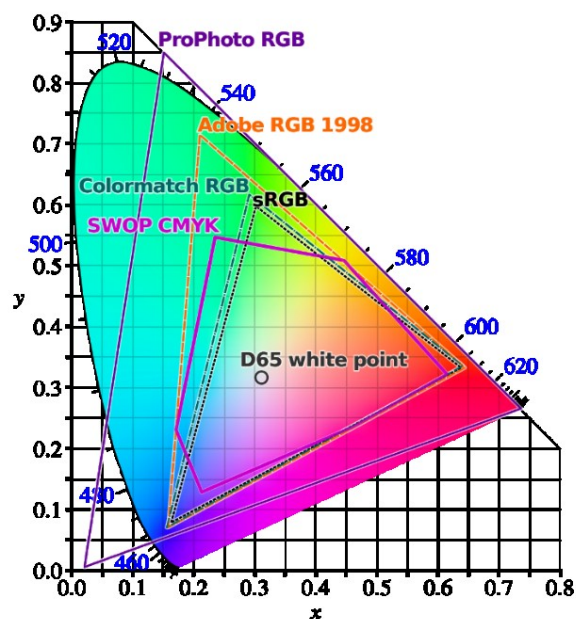


Figure 2.11: CIE 1931 color space and the definition of some popular color spaces, including sRGB, Adobe RGB, ProPhoto RGB...

There are also other subset color spaces such as sRGB and Adobe RGB 1998 developed to adapt the CIE 1931 standard for certain digital devices. Using the CIE standard we can specify any color in terms of its CIE co-ordinates and hence be confident that a CIE defined color will match another with the same CIE definition. Using the CIE 1931 standard we can perform transformations to convert a color from one color space to another.

2.3.4. Color Depth

Color depth indicates the maximum number of possibly distinguishable colors for an imaging device. Color depth has a unit of n-bit color and the total maximum number of colors for an n-bit color device is:

$$\# \text{ of colors} = 2^n$$

Higher color depth gives a smoother transition of colors across the image and also allows more information details to be captured. Most of the current smart phone cameras, such as those in iPhones, Huaweis, and Samsungs, have 24-bit color depth. Therefore 8-bit is assigned for each of the R, G, B components. With 8-bit color depth per channel, the camera is able to distinguish over 16 million colors. In general, human eyes can only detect about 10 million colors, thus 24-bit color depth is also referred to as true color.

2.3.5. Image Sensors

Human vision is a base for conventional imaging. Human eyes exhibit a non-linear response to change in brightness. When our visual system registers a doubling in brightness, the actual light brightness may not have actually doubled. In fact, human eyes have a logarithmic response to the change in brightness, which means our eyes have much higher sensitivity to changing brightness in darker environments [18]. This characteristic means our eyes are much better than digital cameras in detecting small differences in the brightness in a dark environment or scene. Quantifying the actual level of brightness with our eyes, however, is far from practical and usually gives a false result due to this non-linear response.

Digital image sensors such as CMOS or Charge Coupled Device (CCD) sensors detect light purely based on the number of photons hitting the photodetector. Therefore the resultant output, or the pixel value, is truly proportional to the actual light brightness. Figure 2.12 shows the linear response of the CMOS sensors on digital cameras, and this linearity makes digital image sensors more reliable than the human eye when quantitative measurements are needed.

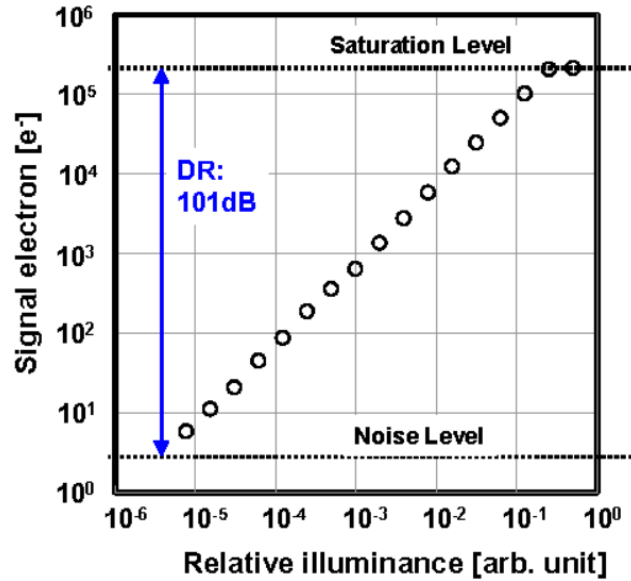


Figure 2.12: Response to illuminance of digital image sensors

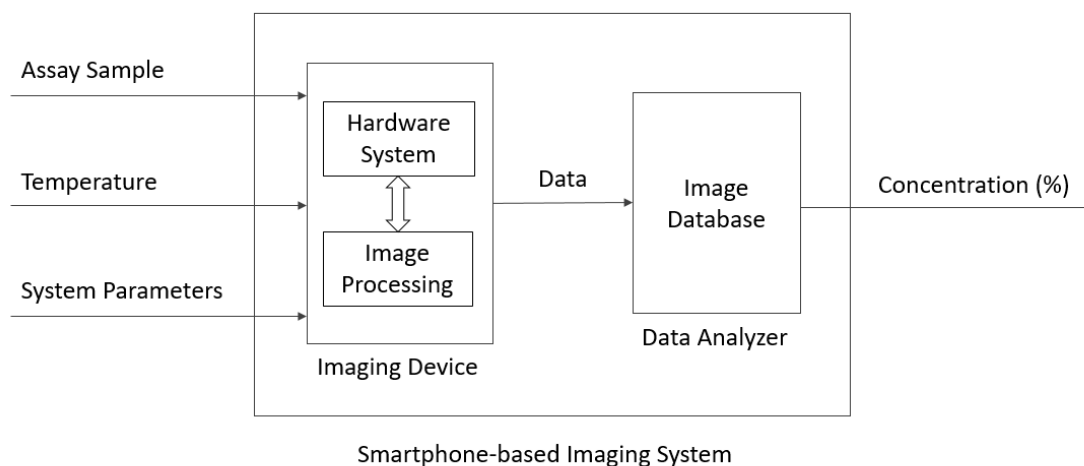
Given that most smartphone cameras have sufficient color depth and a wide bandwidth that covers the range of the human visible light spectrum, we have evidence to hypothesize that the colors of a visible object can be precisely recorded through a smartphone, and that the recorded images can be further processed to give quantitative results that are meaningful and easily interpretable. These hypotheses will be validated in the following chapters based on a systematic experimental step and observed results.

Chapter 3.

Methodology

3.1. System Overview

The general functionality and engineering model of the smartphone imaging system is represented in Figure 3.1. In its simplest form, the entire system can be represented as an imaging device and a data analyzer. To quantify the concentration of compounds within a sample, the system takes several input parameters including the assay type, smartphone settings, spectrum of the light source and temperature. These input quantities allow data to be generated from the imaging device, and with a pre-established database, the concentration of the compound within the sample can be estimated.



The smartphone-based imaging system is mainly composed by an imaging device and a data analyzer. The imaging device includes both hardware and image processing algorithm, generates raw image data from the input conditions, which mainly include the assay sample to be tested, temperature and system parameters such as camera settings and spectral information of the light source. The data analyzer is a mathematical function which intakes the image data and outputs a value that gives the best approximation of the sample concentration.

Figure 3.1: Engineering model of the entire system

3.2. Assay Preparation

3.2.1. Biomaterials and Chemicals

In this study, we focus on chemical and biological assays that are in liquid state. Solutions with various concentrations can be obtained using serial dilutions. For all dilutions, water is used as the solvent. Particularly, two types of assay samples are involved in this research:

Type 1: Fluorescent materials, namely:

- Fluorescein (Section 4.1)
- RNA Mango (Section 4.2)

Type 2: Liquid colloids, namely:

- Homogenized Milk (Section 5.2)
- *Saccharomyces Cerevisiae* (Section 5.3)

This assortment of materials was chosen because their interactions with light are observable. Fluorescent materials will glow when they are illuminated with the light source containing specific wavelengths that trigger the excitation process. Liquid colloids, due to the large size of the particles, may cause scattering of light. Reactions of both fluorescence and scattering can be visualized and thus can be recorded and analyzed by smartphones.

3.2.2. Serial Dilution

Dilution is an important technique in many areas of experimental biology and chemistry. Serial dilution decreases the stock solution by the same proportion in each successive step. Compared to other forms of dilution, serial dilution has much easier operating procedures, and it allows the relative concentrations to be plotted on a logarithmic scale.

The stock solution in this research is measured in Molar concentrations, or Molarity which is denoted as M. The Molarity of a sample is calculated by:

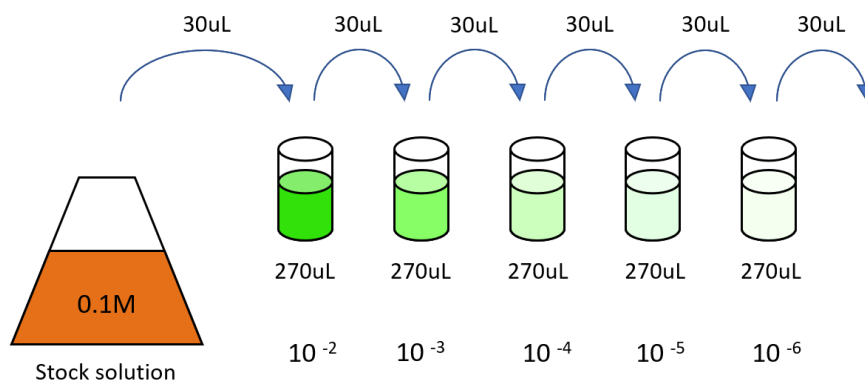
$$\text{Molarity}(M) = \frac{\text{moles of solute (n)}}{\text{Liters of solution (V)}} \quad (5)$$

Where moles of solute (n) is:

$$\text{moles of solute (n)} = \frac{\text{mass of the solute (m)}}{\text{molecular mass}} \quad (6)$$

Based on equation (5) and (6), we can easily calculate the amount of solute and solvent required to obtain a stock solution with desired molar concentration. For example, to make 100mL of 0.1M fluorescein solution, given that its molecular mass is 376.3g/mol [19], we need to dissolve 3.76g of sodium fluorescein into 100 mL distilled water.

Once the stock solution is prepared, we can perform serial dilutions to create solutions of desired known concentrations. Generally, before designing an efficient dilution series, we need to consider the range of concentrations required, that is, the highest and lowest concentrations needed to contain the values expected in the sample of unknown concentration. For example, Figure 3.2 shows the procedure when diluting a 0.1M fluorescein solution using a 10-fold serial dilution wherein the final volume of each dilution solution is 270uL.

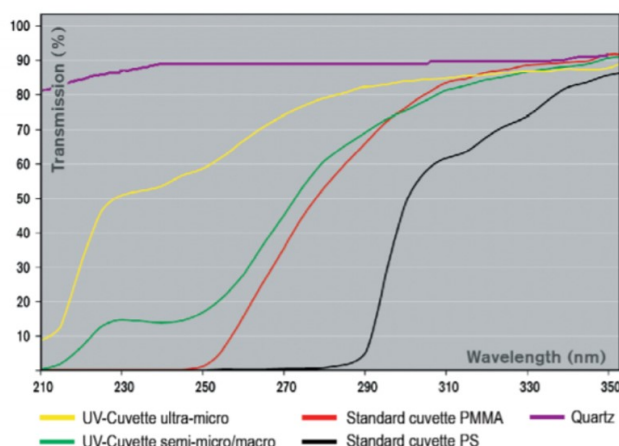


The last arrow in the figure is to keep the last one having the same volume as previous diluted ones. In this serial dilution example, the final serially diluted volume in each container will be 270uL except that the last one is 300uL, so 30uL will be removed from the last container to keep all volumes at 270uL.

Figure 3.2: Diluting a 0.1M fluorescein solution using 10 fold series

3.2.3. Sample Container

Two types of sample containers commonly used for holding assay liquid are cuvettes and microplates. Both containers can be used for preparing and visualizing solutions due to their high optical transmittance. However, microplates and cuvettes are designed for different photometry methods. Cuvettes can be made from plastic, glass and quartz. Quartz cuvettes usually have larger transmission bandwidth and higher optical transmittance, particularly in the ultraviolet region [20]. According to the transmission plot shown in Figure 3.3, quartz cuvettes have a higher bandwidth than plastic cuvettes and are, therefore, better suited for applications when an ultraviolet light source is involved.



Cuvettes made in quartz have exceptionally wide transmission bandwidth therefore is ideal for experiments involving deep ultraviolet light source. If the excitation light is mainly in visible portion (>380nm) then using standard plastic cuvettes is preferred due to lower cost

Figure 3.3 [21]: Transmission curves of cuvettes made from different types of materials

Quartz micro-cuvettes will be used for all the experiments in our research. Quartz cuvettes are not disposable and are more expensive than other cuvette types. Therefore, we need to pay particular attention while handling them. Researchers should always wear latex gloves to prevent the oil from fingers from sticking to the cuvette body. Also, the cuvettes should be held and placed gently while conducting experiments due to their fragility.

Another commonly used sample container are microplates. The most widely-used format is the standard 96-well plate shown in Figure 3.4. A 96-well plate has 8 rows and 12 columns of wells, which allows 96 samples to be tested at the same time. While preparing samples, multichannel pipettes are also available to improve liquid handling efficiency and precision.

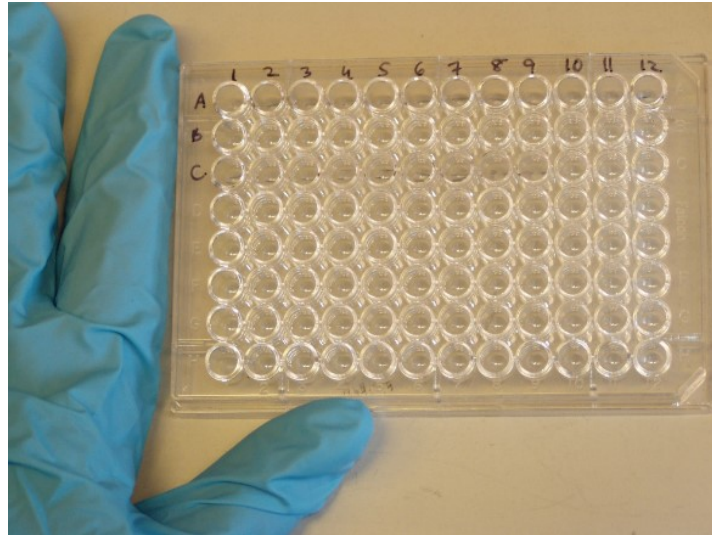


Figure 3.4: Polystyrene 96 well microplate

Both cuvettes and microplates can be used to contain the sample assay due to their high transparency of light. Using microplates as the sample container is an efficient way when dealing with multiple assay samples since it allows up to 96 samples to be quantified and analyzed with a single setup. However, designing a microplate compatible hardware system requires sufficient volume of the enclosure box to fully accommodate the plate, translational stage and electronics. In Appendix A, a process of designing a prototype of microplate-based smartphone image device is illustrated. This prototype allows multiple samples to be tested in one run, but the volume of the entire device can easily exceed 600 in^3 by only achieving axial (instead of planar) movement, and operation of the mechanical parts requires about 2W of electrical power. Obviously, the volume and power consumption are not preferred as a portable device. Using cuvettes as sample container is a more ideal choice for designing a portable system. A cuvette occupies less than 1/10 volume of a microplate. Also, moveable parts are not necessary when measuring small quantity of test samples, hence making the optical setup simpler and less expensive.

Nevertheless, a cuvette-based device is less efficient as it allows much fewer samples to be tested at the same time.

3.3. Hardware System

3.3.1. Light Source

Light-Emitting Diode (LED)

Technically, any light source with a wide spectrum can be used to excite and visualize a sample for a bio-assay. However, our system is also constrained by other factors, including the unit cost, device portability and compatibility with smartphones. In the majority of spectrofluorimetry systems, arc lamps and xenon flash lamps are used as the excitation light source because of their continuous and wide spectral bandwidths [22]. Both of these light sources, however require AC power to operate and are, therefore, not suitable for our design requirements. In general, choosing the appropriate light source is crucial, and the following requirements also need to be met:

- The spectrum of the light source must cover the range to excite the sample;
- The light source must be power efficient;
- The light source must be compact and portable;
- The light source should be inexpensive;
- The emitted light must be very stable.

Two types of light sources that satisfy the above requirements are light emitting diodes (LEDs) and laser diodes. LEDs come in a variety of wavelengths, so it is possible to find an appropriate LED to excite different types of samples (Figure 3.5). LEDs are also inexpensive, consume very little power, and have minimum photobleaching effects [23]. Unlike LEDs, lasers produce monochromatic light, which simplifies the mathematical modelling process. The high irradiance collimated output light of lasers also maximizes the intensity of fluorescent light emitted by the fluorophore [24]. However, the strong intensity of the laser beam may easily cause photobleaching, thus decreasing the number of active fluorophores. Another concern is that laser diodes are more expensive than LEDs,

particularly shorter wavelengths. As a general consideration, LEDs were chosen as the primary light source for our system.

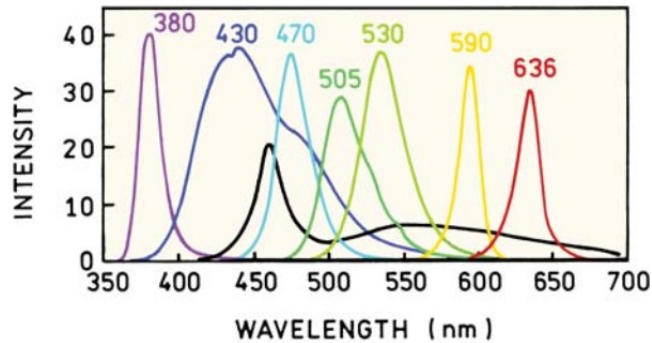


Figure 3.5: Spectrum plot of selected LEDs

Power Supply

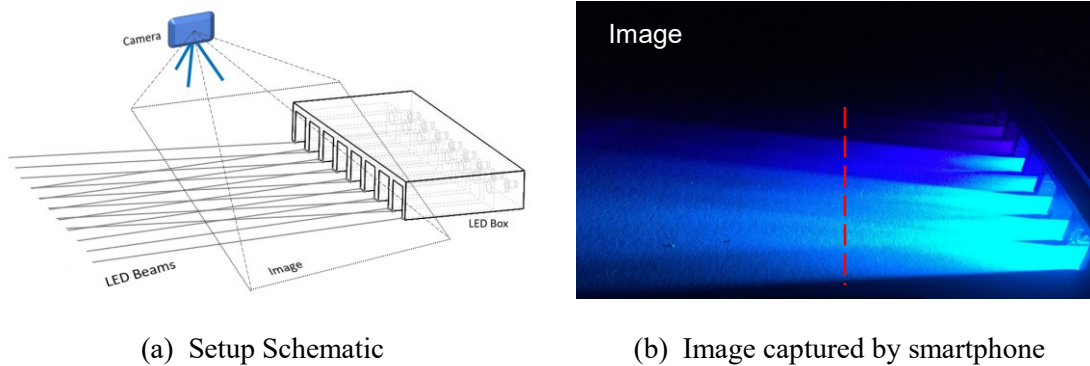
A power supply with highly stable DC output is crucial to our fluorescence experiment since the irradiance of LED is directly proportional to its feeding electrical power. As a portable device, we built a LM2577 based low-wattage power supply with effective DC output range from 3 to 28V as shown in Figure 3.6. LM2577 is a step-up converter with less than 1% of output ripple voltage at its normal operation conditions [25]. The device can be powered by battery cells and last for at least 3 hours at normal operation, thereby enabling its use in the remote areas where a power source is unpredictable or not available.



Figure 3.6: Portable DC power supply

LED Illuminance Testing

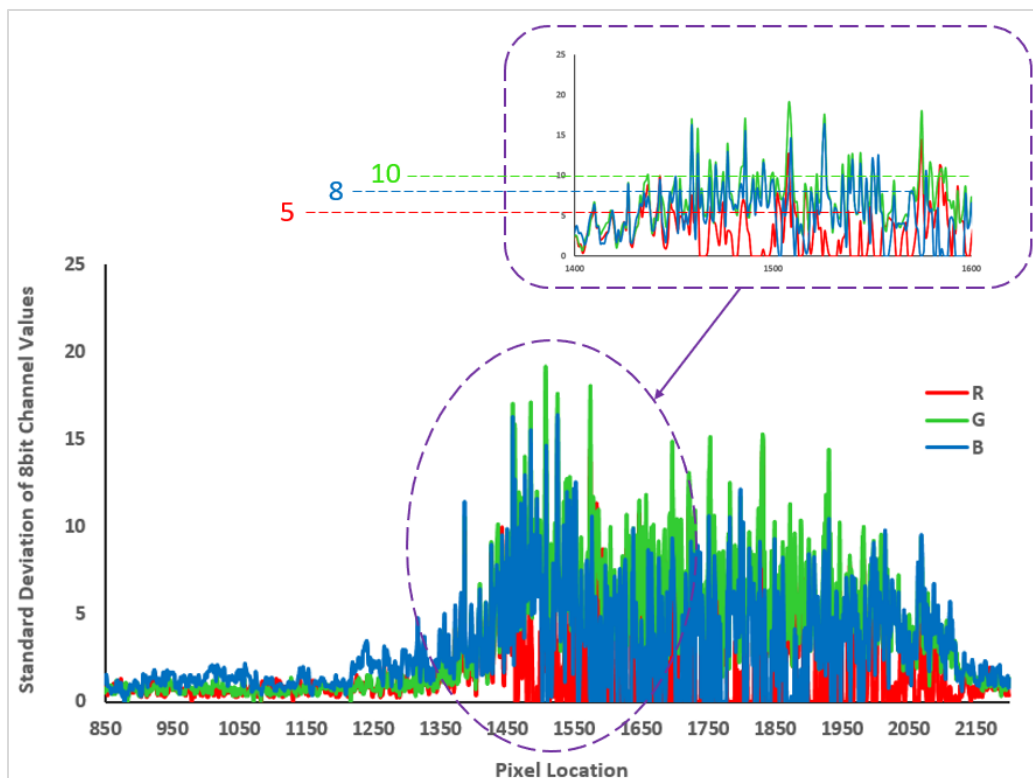
Having a steady and stable light source is crucial for the hardware system. Fluctuations in light intensity will directly affect the amount of fluorescence produced, resulting in noisy output signals. To quantify the signal quality of LEDs, we set up a smartphone based measurement system as shown in Figure 3.7 (a) and (b).



In (a), the LED box contains 3 blue LEDs (peak wavelength: 450nm) and 5 cyan LEDs (peak wavelength: 482nm). We powered up the LED box using our power supply set to 5V. The smartphone (iPhone 6) is securely mounted at the holder aside in order to take pictures of the scattered light of LEDs on the table. Once the images are repetitively acquired, we compare the RGB pixel values at the same location throughout the images. The pixel location chosen in this experiment is the highlighted by the red dot line in (b).

Figure 3.7: LED irradiance measurement setup

The entire experiment is conducted in a dark room to isolate the light noise from room illumination or other light sources. A smartphone camera is set to burst mode to continuously capture images. With this setup, ten images are taken sequentially such that the relative position of each pixel across all images remain unchanged. Using Matlab we interpreted the RGB values at the marked region (identified by the red dotted line) in Figure 3.7 (b) and compare their values in all ten images.



Horizontal axis is the pixel location of the image. The region of interest is shown in Figure 3.7(b), from row 1100 to 2200, at column 1550 (pixel location). The dimension of all images is 2448 x 3264 pixels. Vertical axis is the standard deviation of the 8-bit channel value ranging from 0 to 255. We zoomed in vertical scale (0 to 25) since deviations are small.

Figure 3.8: Standard deviation plot of the RGB pixel values measured from ten images

The above plot (Figure 3.8) shows that a constant light signal exhibits a slight fluctuation based on the interpretation of the RGB values from the phone camera. Based on the plot in Figure 3.8, the average fluctuation of the light source quantified by pixel values of the smartphone is about 5 for Red, 10 for Green and 8 for Blue respectively.

3.3.2. System with Minimal Components

Excitation Setup

As reviewed in section 2.2, the purpose of using a monochromator or optical filter for the excitation light source is to select the particular wavelength in which the absorption of the compound within the specimen reaches a maximum; in this manner, the peak excitation wavelength of the compound within the sample can be precisely determined.

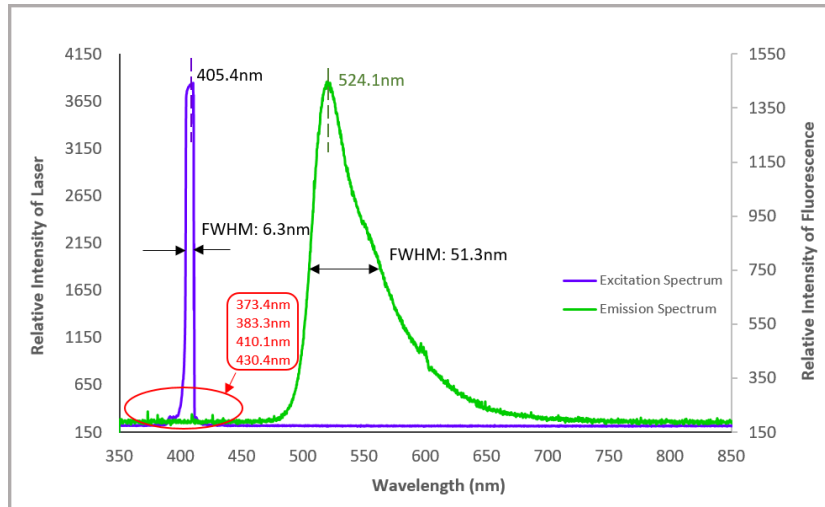
Importantly, the main objective of our system is to establish a quantitative relationship between the fluorescence intensity and the compound concentrations of interest. To this end, having steady and consistent illumination throughout all tests is important. For this purpose, we are not very particular about the LED spectrum as long as its peak wavelength is reasonably close to the peak excitation wavelength of the compound of interest in the sample.

Emission Setup

To suppress the unwanted wavelength generated by the incident excitation light, a monochromator or optical filter is often placed at the emission side of the entire optical setup [26]. In a cuvette-based system we follow the convention to place the detection unit in an orthogonal direction to the incident light to minimize the sensitivity to scattered light noise picked up by the detector [27]. At this stage we wanted to determine the portion of unwanted scattered light picked up by the detector. we designed two experiments to quantify the effects of the actual detected noise to the fluorescence signal. The spectrum of both excitation and emission spectrum will be measured using a spectrometer (Model: SPM-002-E).

Experiment 1:

We used a 405nm monochromatic laser diode as shown in blue in Figure 3.9 to excite a 2mL fluorescein sample prepared in a semi-micro cuvette. The molar concentration of the sample was 1uM. When the fluorescein sample glows, we used a lens to collimate the scattered output light in the direction orthogonal to the incident beam into a spectrometer and obtained the spectrum of the output (emission) light as shown in green in Figure 3.9.

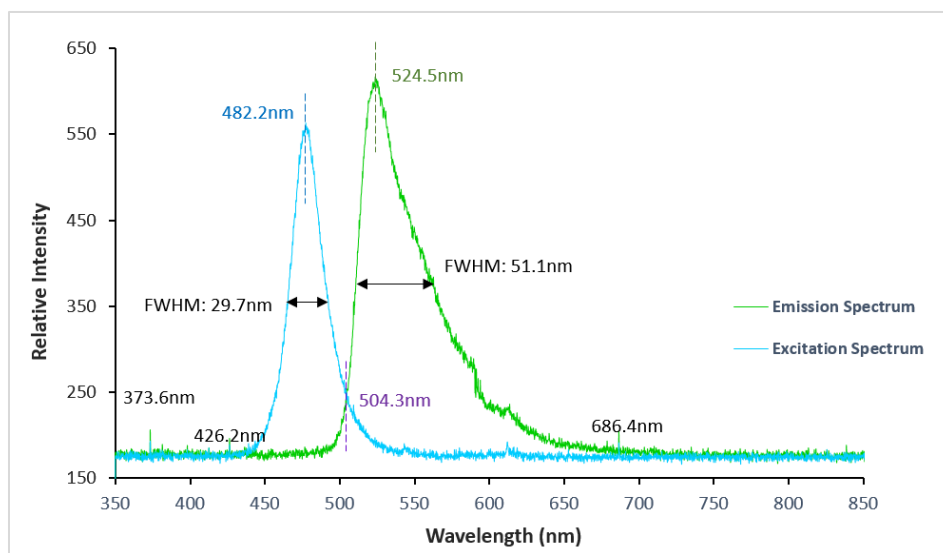


Different exposure times are used while measuring Laser spectrum and fluorescence spectrum. If using the same exposure time, the magnitude of the Laser spectrum will be much higher than fluorescence spectrum

Figure 3.9: 405nm Laser diode excitation and fluorescence emission spectra

Experiment 2:

In this experiment we excited the same fluorescein sample with a cyan LED of which the spectrum is shown in blue in Figure 3.10. The wavelength of the LED was 482.2nm, and it had a full width half maximum (FWHM) of 29.7nm. The emitted light is collected and sent to the spectrometer using the same manner as in experiment 1. The emission spectrum is shown in green in Figure 3.10.



Different exposure times are used while measuring LED spectrum and fluorescence spectrum. If using the same exposure time, the magnitude of the LED spectrum will be much higher than fluorescence spectrum

Figure 3.10: 482nm cyan LED excitation and fluorescence emission spectrum

From the two emission spectrum plots, we observed that the detected output light for both setups are almost identical despite the tiny difference of the peak wavelengths and FWHMs. In both experiments, multiple spikes are observed for wavelengths below 450nm. Since fluorescein does not have any fluorescence emission below 470nm [28], we infer that the spikes below 470nm are due to the scattering of the input light source. Fortunately, the magnitudes of these noise spikes are so small that they can be simply ignored. The results from the above experiments suggest that the output light seen by the detector contains insignificant amount of interference light from the input source, even without the presence of optical filters.

3.3.3. Image Detector

CMOS image sensors are typical devices to convert received light signals into electric signals. Due to its low power consumption, high read-out speed and small size, CMOS image sensors are common in cellphone cameras [29] [30]. Table 3-1 lists the camera features of several popular smartphones.

Table 3-1: Optical parameters of some popular smartphone cameras

Smartphones	Color Depth	Effective Pixels	Aperture	FOV_X (degree)	FOV_Y (degree)
iPhone 6	24	8 MP	f/2.2	63.7	45
iPhone 4s	24	8 MP	f/2.4	54.5	37.8
Huawei Mate 9	24	12 MP	f/2.2	67.4	47.9
Vivo X5	24	13 MP	N/A	N/A	N/A
Samsung Galaxy S9	24	12 MP	f/2.4	69.4	49.6
HTC 10	24	12 MP	f/1.8	69.4	49.6

All smartphones listed above have 24-bit color depth, or 8-bit per each channel. Field of view (FOV) is the angle through which the camera can detect light. These angles are used to calculate the relative positions of each component for enclosure design. In this thesis work, the main smartphone used for all imaging and processing is iPhone 6, which

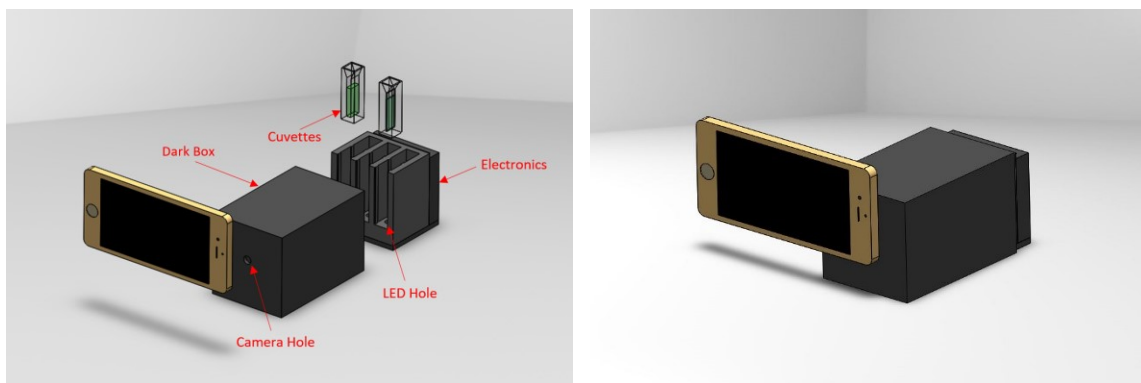
uses a back-illuminated CMOS image sensor featuring 1.5 μm generation pixels fabricated by Sony [31]. The back-illuminated CMOS image sensor allows more light to be captured by the same chip area therefore enhances performance under low-light condition.

3.3.4. Enclosure Design

To complete the hardware design, we need to build an enclosure that accommodates all components. Based on the properties of each component described above, the enclosure should meet the following requirements:

- Fits to the dimension of standard cuvettes;
- Mounts LEDs such that light can directly illuminate samples;
- Blocks all backlight from the external environment;
- Allows the smartphone camera lens to capture the internal setup;
- Provides a reference color for image acquisition and processing.

Figure 3.11 is the Computer Aided Design (CAD) model illustrating the enclosure system. Two identical LEDs are mounted vertically into the two LED holes (left and right) giving an upward illumination towards the samples. Once the cuvettes are in position, the entire housing will be fully enclosed by the dark box to prevent ambient light leaking inside the enclosure. Users can turn on the device from the electronics module on the backside and align the smartphone camera to the camera hole at the front face for observation and imaging, see Figure 3.11 (b).

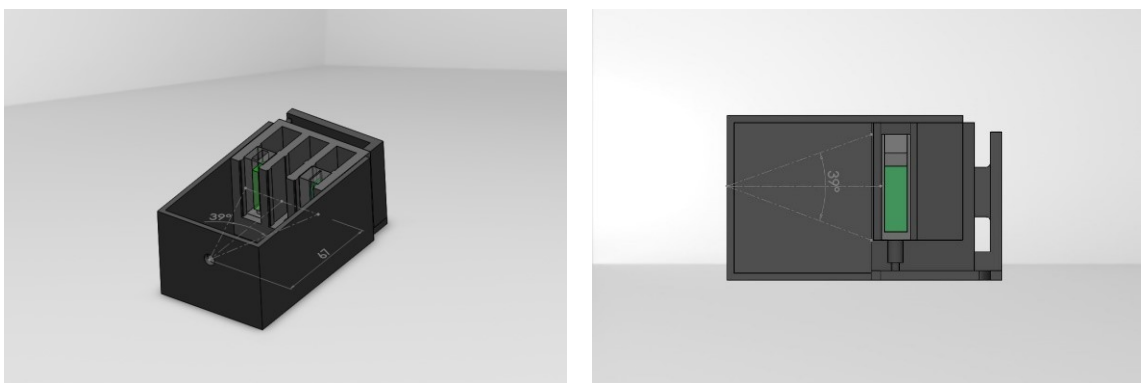


(a) Positioning of Each Unit

(b) Ready to Test Device Setup

Figure 3.11: CAD model of the enclosure design

The exact geometry of the set up can be visualized in the sectional views of the device as shown in Figure 3.12 (a) and (b). To ensure the region of interest is covered by all smartphone cameras listed in Table 3-1, the distance between the smartphone camera and cuvettes is 67 mm and the horizontal angle and vertical angle from the camera to the two edges of the cuvettes are both 39 degrees. Also, the relative position for each component is constant; therefore we crop out the unused portion of the image to reduce the amount of computation for image processing.



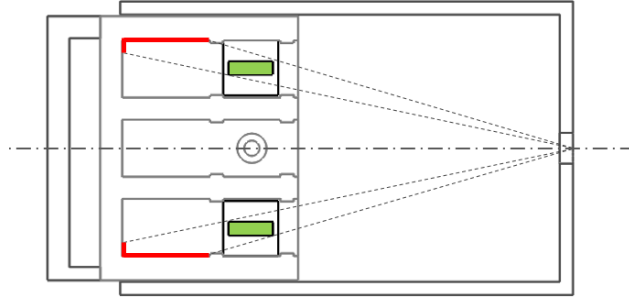
(a) Horizontal Angle

(b) Vertical Angle

Figure 3.12: Geometry of the layout setup

Using the right-angle positioning layout prevents the image detector (smartphone camera) detecting excitation photons while LEDs are illuminating the sample. Another important design factor for the enclosure is the sidewall around cuvettes. When LEDs are illuminating, some amount of incident photons will hit the surface of sidewall and produce

scattered light. The optical path, as indicated by the dashed lines in Figure 3.13, shows that the scattered light in the red highlighted region will be picked up by the image detector.



The dashed lines and red highlighted region indicate the scene captured by the image detect which contains useful information of the sample to be tested

Figure 3.13: Top view of the enclosure box

In the region of the image detected by the camera, the pixel value $g(x,y)$ can be expressed as:

$$g(x,y) = f(x,y) + \eta(x,y) \quad (7)$$

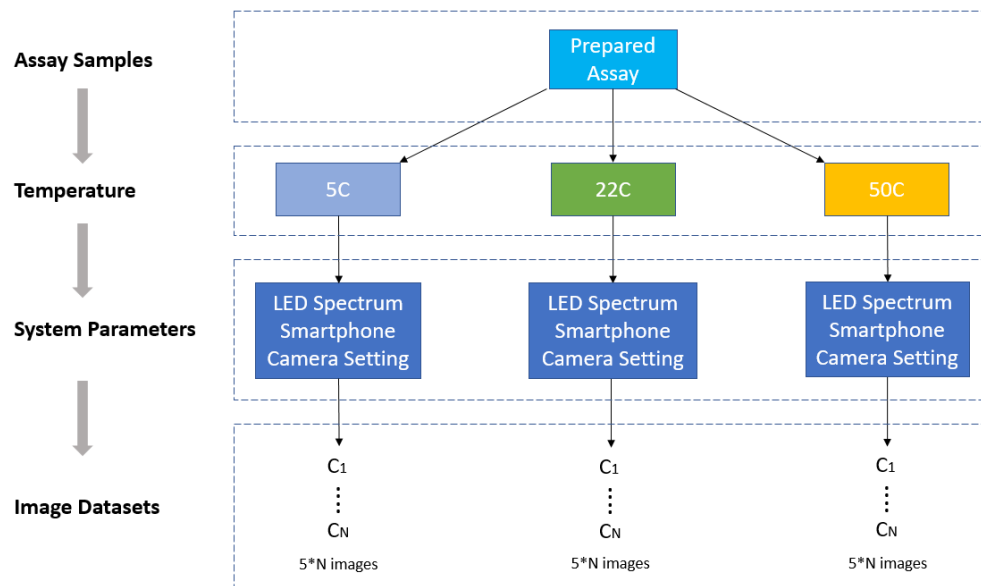
where $f(x,y)$ is the pixel value of the fluorescent output light, $\eta(x,y)$ is the pixel value representing the scattered light on the side walls. It should be noted that $f(x,y)$ is related to the concentration of the sample whereas $\eta(x,y)$ is a constant that is determined by the input light source only. At very low concentrations where the intensity of the interested signal is low, $f(x,y)$ is negligible and can be eliminated. Therefore $g(x,y)$ will approaches the constant value of $\eta(x,y)$. The phenomenon when $g(x,y)$ no longer responds to the changing of concentrations can be used as a condition to determine the detection limit of the system.

3.4. Data Collection

3.4.1. Image Datasets

Once the sample and hardware setup are prepared, the next step is collecting image data to be interpreted. The manner in which we collect the image data is structured as

shown in Figure 3.14. Each sample will be tested under 5°C, 22°C and 50°C to simulate possible indoor and outdoor ambient conditions. For each temperature, we acquired images of different sample concentrations at each of the control parameters including LED intensity, smartphone types, exposure time, focus and ISO settings.



Samples at each temperature are prepared by dissolving the solute in 5°C, 22°C and 50°C of water respectively. At each concentration, 5 images will be respectively taken which will be further used for image processing. An interval of 2-3 seconds is given between capturing each image to prevent the CMOS sensors heats up (which may contribute to additional noise). The entire process should be repeated at least three times, to allow calculating for maximum and minimum errors.

Figure 3.14: Process of acquiring image data

3.4.2. System Parameters

Focus

As shown in Figure 3.15, a smartphone makes use of a voice coil motor to move the camera module to adjust the focus. Unlike most digital single-lens reflex (DSLR) cameras, smartphone cameras do not have physical shutters in their optical paths. The exposure time of a smartphone is achieved by setting the time intervals in which its image sensor remains active to accumulate signal produced by the incident (focused) image [32].

In fact, the smartphone image sensor always sees the incident image. In other words, it is continually exposed.

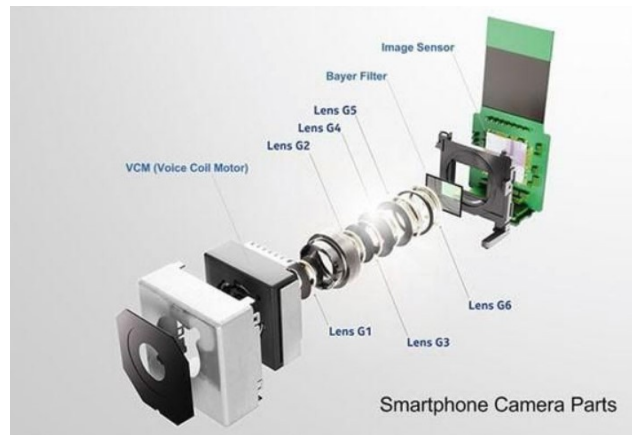


Figure 3.15 [33]: Illustration of the composition of a smartphone camera

Many smartphones have both automatic and manual options to adjust focus and exposure for photography. An auto-adjustment algorithm might be particularly useful for people with less knowledge of photography. However, auto-adjustment should be avoided in our application. The main reason is that the color information of each image is dependent on exposure value. Since we do not know the exact algorithm implemented by the phone camera, the interpretation of the image data is complex. In this situation, the most reasonable solution is to adjust the settings manually. This will allow us to establish a consistent reference for the experiment.

Exposure Time and ISO Setting

The exposure time, ISO and aperture, sometimes called the “exposure triangle”, used to capture the static image of interest can affect experimental results. ISO controls the gain, or the sensitivity of the camera to the light incident on the image sensor. Exposure time is the duration for which the image sensor stays active to the exposed light. The relationship between pixel value of the captured image and luminance of the object is modeled as follows [34]:

$$N_d = \left(\frac{K_c}{f_s^2} \right) (tS)L_s \quad (8)$$

where the quantities are

K_c Calibration constant for the camera

t Exposure time in seconds

f_s Aperture number

S ISO setting in seconds

L_s Luminance of the scene

The only sources of light in our system are from the LEDs and the fluorescent light emitted by the compound in the sample solution. Given the condition that LED intensity remains constant, the change in luminance, L_s , is mainly due to sample emission, which is related to the concentration of the compound of interest. Identical smartphones are used for each set of the experiment, thus the calibration constant and aperture are fixed numbers. Eventually, the only two quantities in this equation that may vary are the ISO setting, S , and exposure time, t . To establish a relationship between image sensor output and fluorescence intensity, ISO and exposure time should be manually adjusted to a set of fixed values for each experimental step.

3.4.3. Temperature

Temperature influence the transitions of electrons between first excited state and higher vibrational states due to the change in vibrational level of the ground state [35]. Consequently, fluorescence intensity is temperature dependent. The three temperatures we choose in the experiment, 5°C, 22°C and 50°C cover the typical indoor and outdoor temperature conditions where our final product would be used. The effects of temperatures below 0°C were not investigated since water is frozen at these temperatures, making it difficult to run bio-assays based on liquid specimens. Temperatures above 50°C are not conducive for humans to conduct any tests or experiments. 22°C represents typical working environments.

3.4.4. Assay Samples

As mentioned in Section 3.1, all samples were in liquid state and prepared in micro-liter quartz cuvettes. Fluorescence quantum yield affects the quantification of the compound of interest. Quantum yield, Φ is defined as:

$$\Phi = \frac{\text{\# photons emitted}}{\text{\# photons absorbed}} \quad (9)$$

Table 3-2 lists a set of materials with different quantum yields [36]. Materials with higher quantum yield can produce stronger fluorescence intensity compared to low quantum yield materials, resulting in different characteristic curves. For each type of material/sample to be tested, we needed to establish a database that was based on the image processing results at specific system parameters.

Table 3-2: Fluorescence quantum yield of several chemicals

Sample	Quantum Yield
Fluorescein in 0.1 N NaOH	0.90
p-Terphenyl in cyclohexane	0.95
Flavin mononucleotide (FMN) in water	0.26
Flavin adenine dinucleotide (FAD) in water	0.03
Nicotinamide adenine dinucleotide (reduced, NADH) in water	0.03
Wild type green-fluorescent protein (GFP)	0.79
Enhanced green-fluorescent protein (eGFP)	0.64
Enhanced yellow-fluorescent protein (eYFP)	0.61
Enhanced cyan-fluorescent protein (eCFP)	0.39
Enhanced blue-fluorescent protein (eBFP)	0.24
Discosoma red-fluorescent protein (DsRed)	0.70

3.5. Image Processing

3.5.1. Flowchart

Image data collected at different conditions were processed using several steps (Figure 3.16). In this stage, image processing was implemented using Matlab and ImageJ. Acquired raw images will be cropped first to reduce the amount of computational work. Repetitive images will be averaged to minimize the noise occurred from the CMOS sensor.

The region of interest (ROI) will be located based on the layout geometry, and the ROI was segmented for color analysis.

The system uses RGB color model for fluorescence signal measurement. Particularly, the RGB colors are interpreted in two ways and used as two measurement approaches for the same image data: 1) the ratio of two channels and 2) grey scale value (average pixel value of three channels). Response curves that give direct visual representation of the relationship between fluorescence signals and sample concentrations will be plotted for each measurement approach. These curves are useful for analysis and provide quantitative results that can be compared and validated against a commercially available instrument used in a life sciences laboratory.

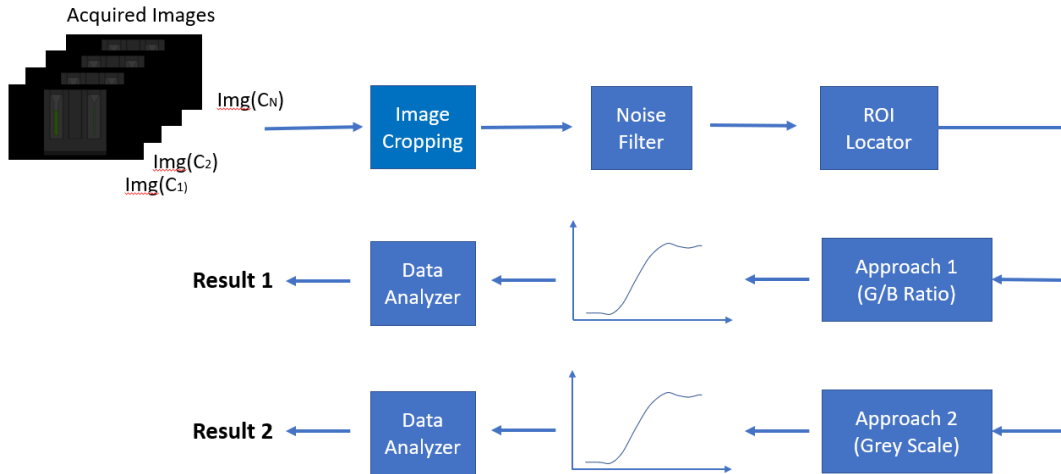


Figure 3.16: Image processing flowchart

3.5.2. Image Cropping

The regions in the image that do not carry useful information can be excluded from computation in order to reduce processing time. Since the relative position of the phone camera and sample holders are fixed, we can calculate the exact location of boundary pixels of the ROI. As shown in Figure 3.17, any camera with larger than 39 degrees in both horizontal and vertical angle of view can cover the signal region. Thus if the horizontal and vertical angle of views are α and β degrees, the actual useful portion of the image that is bounded by the width W and height H can be calculated as:

$$W = X * \frac{39}{\alpha} \quad (10)$$

$$H = Y * \frac{39}{\beta} \quad (11)$$

Where X and Y are the horizontal and vertical number of pixels respectively. Since all of the phone cameras listed in Table 3-1 have larger than 39 degrees of viewing angle, the region in which all activity takes place will always be covered within the field of view of the camera, as shown in Figure 3.17. In software implementation, computations are restricted within the cropped region.

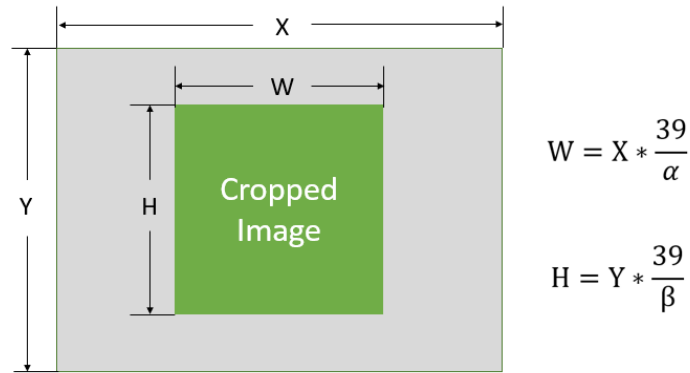


Figure 3.17: Calculation of the cropped image area

3.5.3. Noise Reduction

Reduction of noise improves the signal quality and will increase the sensitivity of the results. In our system, the majority of the noise is contributed by the LED light source and the CMOS sensor of the digital camera. The noise at different pixels from these two sources can be either correlated or uncorrelated. In our modeling we treated noise values at different pixels as being independent. Thus the observed pixel value at any coordinate $g(x,y)$ can be expressed as:

$$g(x,y) = f(x,y) + \kappa(x,y) + \eta(x,y) \quad (12)$$

In this equation, we treat $f(x,y)$ as the pixel value of the main constant portion of the illuminated object, that is, the emission light coming from the assay sample. We also let $\kappa(x,y)$ be the fluctuation of the LED light source and treat $\eta(x,y)$ as the random thermal noise of the CMOS sensor in smartphone.

Suppose we acquire N images for each measurement and take the average of the N images during processing. The new pixel value at each point will be given as:

$$\bar{g}(x,y) = \frac{1}{N} \sum_{i=1}^N g_i(x,y) \quad (13)$$

Equation 13 can be further expanded as:

$$\begin{aligned} \bar{g}(x,y) &= \frac{1}{N} \sum_{i=1}^N [f_i(x,y) + \kappa_i(x,y) + \eta_i(x,y)] \\ &= \frac{1}{N} \sum_{i=1}^N f_i(x,y) + \frac{1}{N} \sum_{i=1}^N \kappa_i(x,y) + \frac{1}{N} \sum_{i=1}^N \eta_i(x,y) \end{aligned}$$

Since $f(x,y)$ is assumed to be constant across the images, this equation can be further rearranged as:

$$\bar{g}(x,y) = f(x,y) + \frac{1}{N} \left\{ \sum_{i=1}^N \kappa_i(x,y) + \sum_{i=1}^N \eta_i(x,y) \right\} \quad (14)$$

In equation 14, the noise from CMOS sensor will be averaged based on the number of images acquired. We will use burst mode to take consecutive images for each measurement to ensure the CMOS noise is suppressed.

3.5.4. Locating the Region of Interest

The ROI contains all the information needed to interpret the experimental result. Figure 3.18 gives an example of an image acquired by the smartphone camera. The regions outlined by red dotted lines indicate the location where the assay samples are contained.

The activities of excitation and emission take place only within these regions, therefore, they should be isolated as the ROI for further image processing.

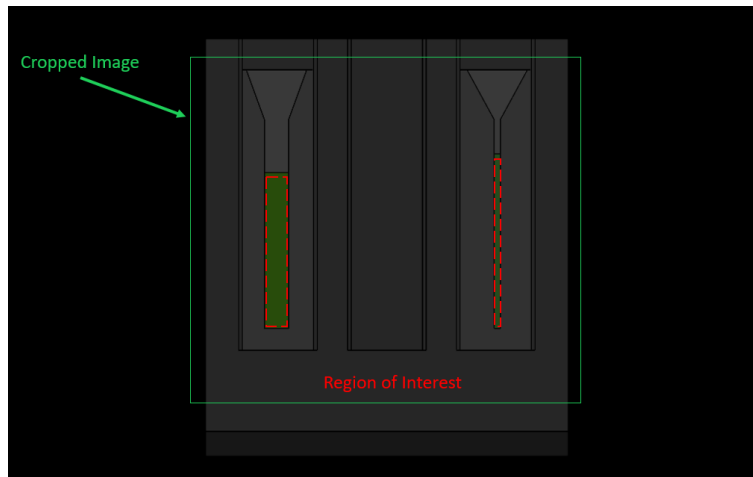


Figure 3.18: Region of interest from the cropped image

To establish the ROI we used three approaches based on our implemented hardware and enclosure design. They are:

- Manual Selection
- Geometrical Method
- Image Segmentation

Manual selection can be easily implemented using the image processing software ImageJ, which allows users to manually select the region on the image for data analysis. The geometrical method is based on the fact that the relative position among all parts of the enclosure are known and fixed during the test, therefore, the pixel location of the ROI can be calculated using geometric calculations. With image segmentation, a color threshold is set to filter out undesired pixel clusters. At this stage in research, we use the manual selection approach to locate the ROI. However, for very large volume data processing the other two methods are preferred.

3.5.5. Measurement Approaches

Approach 1: Ratio of Two Color Channels

Table 3-3 gives the formula to convert monochromatic wavelength to RGB values. This table indicates that red channel is most sensitive to 580-700nm range of wavelength, green channel is most sensitive to 490-580nm and blue channel is most sensitive to 410-490nm.

Table 3-3 [37]: Conversion from monochromatic light to RGB values

Wavelength Interval	Normalized RGB Value
410-440nm	$R = 0.19 - 0.19 * \frac{440 - Wavelength}{30}$ $G = 0$ $B = 1$
440-490nm	$R = 0$ $G = 1 - \frac{490 - Wavelength}{50}$ $B = 1$
490-510nm	$R = 0$ $G = 1$ $B = \frac{510 - Wavelength}{20}$
510-580nm	$R = 1 - \frac{580 - Wavelength}{70}$ $G = 1$ $B = 0$
580-640nm	$R = 1$ $G = \frac{640 - Wavelength}{60}$ $B = 0$
640-700nm	$R = 1$ $G = 0$ $B = 0$
700-780nm	$R = 0.35 - 0.65 * \frac{780 - Wavelength}{80}$ $G = 0$ $B = 0$

Since we did not install a narrow band emission filter in the system setup, the fluorescence signal detected by the smartphone camera is a polychromatic signal with a spectral range that may cover multiple effective color channels of the camera. Figure 3.19 is the emission spectrum of fluorescein. The spectrum is wide and covers all color channels of the camera. Practically, we use the ratio of two color channels which have the most overlap regions to the output light to determine the relative fluorescence intensity. therefore in this case we will use the Green and Blue channels.

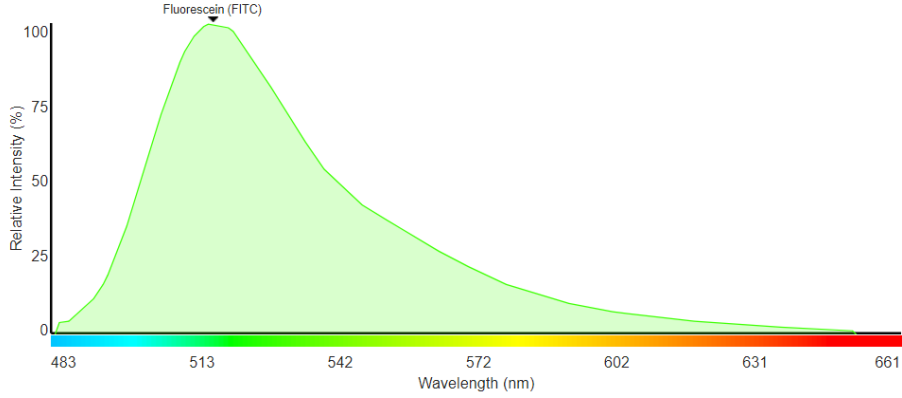


Figure 3.19 [39]: Emission spectrum of fluorescein

For a specific ROI with size of $M \times N$ pixels, the ratio of two channels (e.g. Green and Blue channels) can be calculated as:

$$G/B \text{ Ratio} = \frac{\sum_{i=1}^M \sum_{j=1}^N p(g)_{i,j}}{\sum_{i=1}^M \sum_{j=1}^N p(b)_{i,j}} \quad (15)$$

where $p(g)_{i,j}$ and $p(b)_{i,j}$ are the 8-bit green and blue pixel values at location (i, j) .

One advantage of using this approach is that the measurement is less affected by changes in camera exposure time. If the measurement result is based only on a single channel (e.g. Green), using different exposure times changes the total radiation received by the CMOS sensor, thus causing a shift of channel values. However, when using two color channels, the change in radiation energy received by each color channel can be effectively cancelled when their ratio is considered. This phenomenon is further explained in Appendix B.

Approach 2: Grey Scale Measurement

Grey scale is used as another measuring approach to estimate the fluorescence intensity. Essentially, grey scale value is the average value of the Red, Green and Blue channel values, which mathematically can be expressed as:

$$\text{Grey Scale Value} = \frac{1}{M \times N} \sum_{i=1}^M \sum_{j=1}^N \frac{p(r)_{i,j} + p(g)_{i,j} + p(b)_{i,j}}{3} \quad (16)$$

Specifically, we conducted an experiment to calibrate the spectral sensitivity of iPhone 6 as illustrated in Appendix C. The experimental result shows that using G/B ratio is most sensitive while measuring spectrum around 550nm, which overlaps the output fluorescent signal of the samples. Also, measurement with G/B ratio is more sensitive to the phase shift of the light spectrum, particularly when the spectrum covers the sensitive range of Green and Blue color pixels of the CMOS sensor. For approach 2 (grey scale values), the output value is determined by all color channels of the smartphone, thus it is more sensitive to detect the intensity change of visible light. The drawback of approach 2 is that it only tells the change of light intensity but provides no information about the phase of the spectrum.

3.5.6. Data Analyzer

Measurement approaches with both G/B ratio and grey scale should exhibit consistency in terms of intensity measurement. By plotting the response curves at different concentrations, we can determine the quantitative results for each measurement. These results can characterize the performance of our system, including important parameters such as detection limit, sensitivity, repeatability and accuracy. Figure 3.20 helps to illustrate these definitions pictorially.

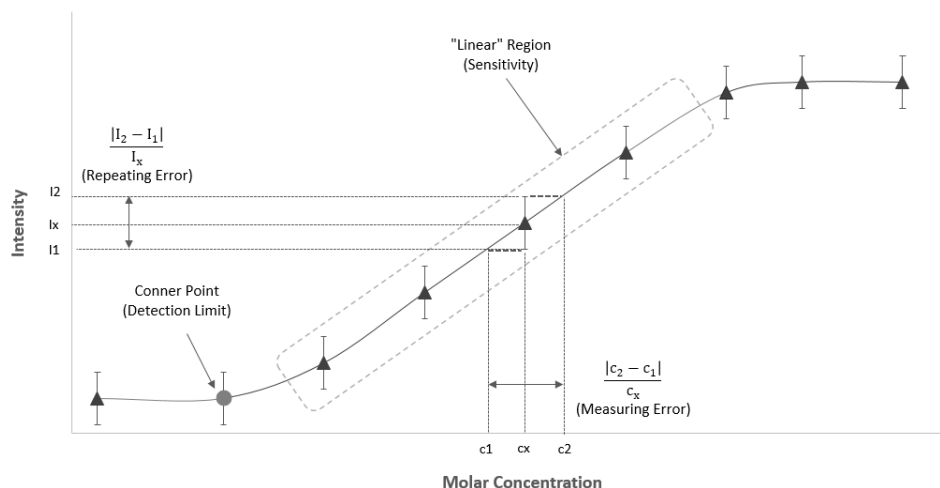


Figure 3.20: Illustration of repetition error, sensitivity, measurement error and detection limit

Detection limit

In this context, detection limit refers to the lowest concentration at which the fluorescence signal can be picked up and quantified by the system. The detection limit of the system is identified by the change in slope in the response curve (Figure 3.20). More precise determination of detection limit can be accomplished with more data points along the intensity versus molar concentration response curve.

Sensitivity

Typically, the expectation of any measurement system is to exhibit high sensitivity above the detection limit. To be sensitive the intensity value of the device should change consistently in response to changes in concentration. The linear region of the response curve in Figure 3.20 indicates the range of concentrations within which the system is sensitive. To quantify sensitivity, we use a linear curve fitting method to model the function mathematically in this region. For consistency, the curve fitted line should have an R-square value of at least 0.95. The slope or gradient of the curve in the sensitive region is defined as sensitivity. Though the slope is linear in the above descriptive graph, it can also be exponential, logarithmic, or follow even more complex functions depending on the prosperities of the assay.

Repeatability or Repetition Error

Repeatability is an important index to evaluate the precision and measuring consistency of our system. Repeatability is a parameter characterizing the closeness of the agreement for the system responses obtained from successive measurements under the same test conditions. By generating response plots from multiple experiments under the same conditions, repeatability can be represented by the vertical error bar on the response curve. In Figure 3.20 for measuring an unknown solution with concentration c_x , repeatability is defined as:

$$\text{Repeating Error} = \left(\frac{|I_2 - I_1|}{I_x} \right) \times 100\% \quad (17)$$

where I_x is the intensity of c_x , I_1 and I_2 are intensities corresponding to the lower and higher concentrations respectively. High repeatability means the system is very precise and consistent, therefore indicates a small difference between I_1 and I_2 for various experiments. Typically, repeatability has no units and will be denoted as a percentage.

Measurement Error

Similar to repeatability, errors in measurement can be estimated. Accuracy of measurement can be defined as the closeness between the result obtained by our device and the true value expected from the measurement. Since the measuring target of our device is concentration, the accuracy of a measured concentration c_x is defined as:

$$\text{Measuring Error} = \left(\frac{|c_2 - c_1|}{c_x} \right) \times 100\% \quad (18)$$

where c_1 and c_2 are the two concentration values corresponding to the lower error bar and higher error bar of the point being measured. For a measurement to be accurate, the value of accuracy should be small. For example, $(10 \pm 5\%)$ nM is relatively more accurate than $(10 \pm 20\%)$ nM. Since the error bars for each sample point may vary, we will accommodate the worse case result as the overall resolution of the entire system.

3.6. Image Database

Implementation of our quantification system requires a database that converts data from the imaging device to concentrations of the sample. The imaging device and the data acquisition system generate a series of output data containing:

- Assay information
- Temperature
- Smartphone, LED power, Exposure Time, ISO settings
- Channel Ratio Value, grey scale value

The system takes the above information and outputs the closest concentration determined by using the database. This database is established from the test results conducted for known sample concentrations at given conditions. For an actual experiment when the sample concentration is unknown, the system will perform reverse mapping based on the pre-established test results. The accuracy and precision of the measurement can be improved by repetitively collecting a large volume of test results. This can be achieved by designing a modified hardware system that allows data from multiple samples to be simultaneously and continuously collected and processed. A more detailed design is illustrated in Appendix A.

Chapter 4.

Fluorescence-based Measurements

4.1. Fluorescein

4.1.1. Properties of Fluorescein

Fluorescein is an organic chemical compound that is commonly used as fluorescent dye. Fluorescein has high molar absorptivity at 480 nm, high fluorescence quantum yield and good water solubility, which makes it very useful for detection and optical imaging. As shown in Figure 4.10, fluorescein has a relatively wide fluorescence emission spectrum where the full wave half maximum (FWHM) is about 50 nm and peak emission of 516 nm. The emitted spectrum shows a green dominant color.

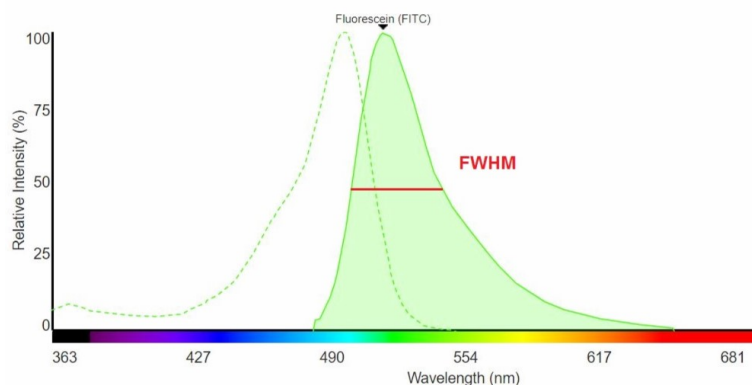


Figure 4.1 [38]: Excitation and emission spectrum of fluorescein

The molar mass of fluorescein is $332.31\text{g}\cdot\text{mol}^{-1}$, which can be used to determine the exact molar concentration in an aqueous solution. Researchers have found that both pH value and temperature can affect fluorescence intensity while other conditions are held constant [39]. In this research we use water as the only solvent to keep pH value at 7.0 for all experiments.

Temperature is also a factor in our measurement, and this can vary depending on the experimental environment. As explained in Sec 2.2.1, fluorescence emission is generated from the process where molecules from higher vibrational energy level falls back

to the ground state. Changes in temperature affect the vibrational energy of molecules. As a result, the fluorescence output will be temperature dependent. Figure 4.2 shows the emission spectrum of fluorescein from 25°C to 100°C. The plot indicates that fluorescein generates a stronger emission signal at higher temperatures.

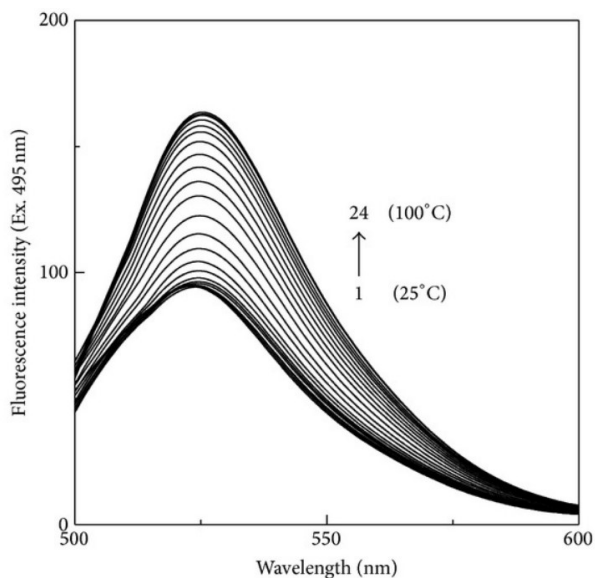


Figure 4.2 [40]: Emission spectrum of fluorescein at various temperatures

4.1.2. Experimental Setup

Sample Preparation

Diluted fluorescein samples are prepared in cuvettes. The cuvettes we used are reusable quartz micro-cuvettes with full capacity of 1.05mL volume. Exact concentration of the sample solution was determined by using precision microliter pipettes and careful serial dilutions.

In normal backlight conditions, fluorescein of concentrations above 10 μ M can be visualized with the naked eye. A special excitation light source must be applied to visualize lower concentration fluorescein solutions. In the experiment we used 10-fold serial dilutions to obtain different sample concentrations. The concentrations of diluted fluorescein solution are listed in Table 4-1.

Table 4-1: Serial dilution table of fluorescein

Serial Number	Molarity (nM)
1	100000
2	10000
3	1000
4	100
5	10
6	1
7	0.1
8	0.01

At higher concentrations, probabilities of collision between fluorophores and molecules increase dramatically thus suppressing the intensity of fluorescence signal, which is also known as the effect of quenching. Quenching affects the emission intensity significantly during the experiment. Literature reports that the fluorescence intensity of fluorescein loses proportionality at concentrations higher than $200\mu\text{M}$ as shown in Figure 4.3 [41]. Therefore, the maximum molarity of fluorescein being tested in this experiment is limited to $100\mu\text{M}$.

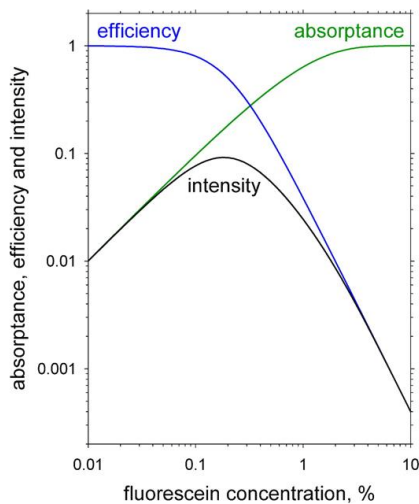
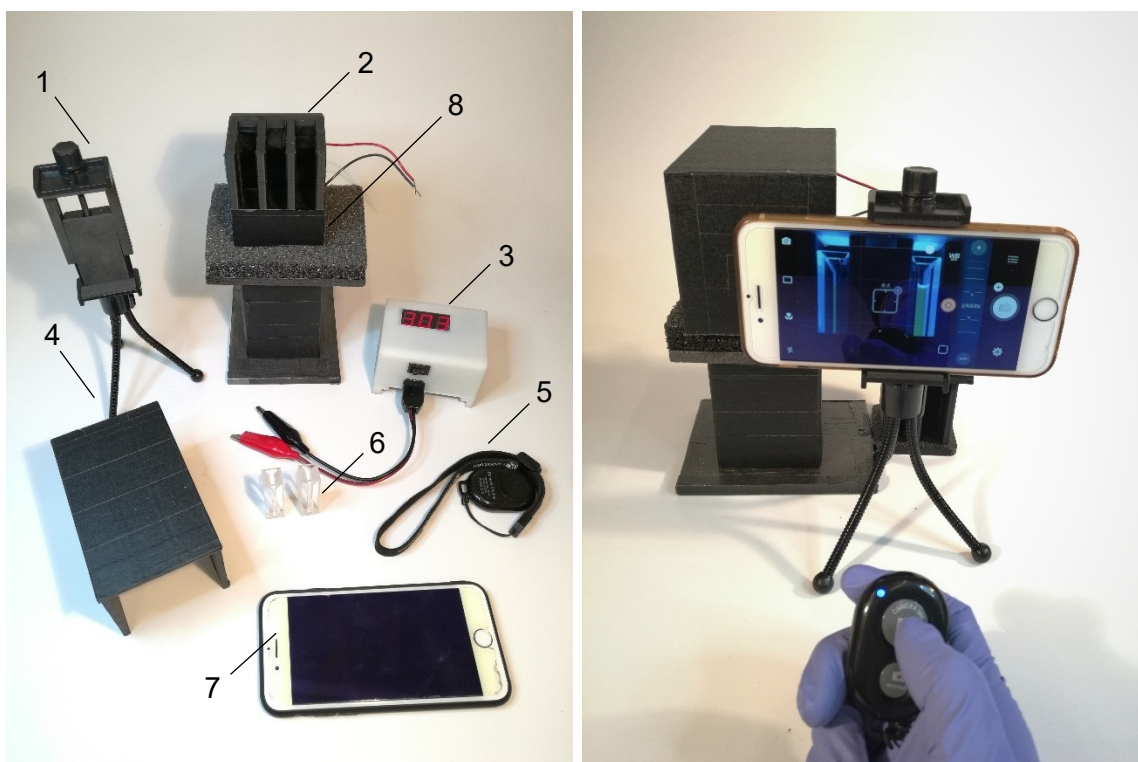


Figure 4.3 [41]: Fluorescence intensity of fluorescein at high concentrations, 1% corresponds to 3.8mM

Hardware Setup

The device setup is illustrated in Figure 4.4. Figure 4.4 (a) shows all of the necessary assortment of apparatus required for the experiment. All parts are labeled in Table 4-2. Figure 4.4 (b) is the setup when all components are assembled. The power supply used for the experiment is adjusted to 3V. The smartphone should be placed tight against the dark box to ensure ambient light does not leak into the enclosure. To acquire an image, we used the remote snapshot controller to prevent shake, which could result in blurred images.



Description of each labeled part is illustrated in Table 4-2

Figure 4.4: Hardware setup for smartphone based fluorescence measurement

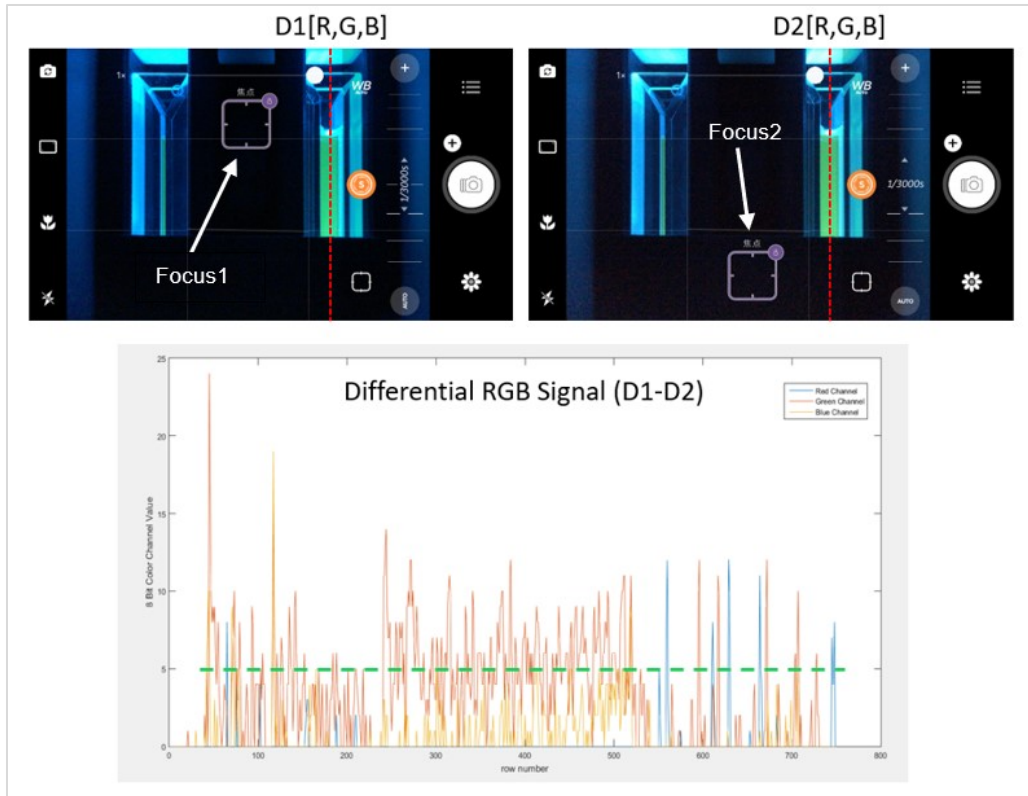
Table 4-2: Description of each part in Figure 4.4

Label	Name	Description
1	Smartphone Holder	Holds a smartphone and place it to desired position
2	Cuvette Chamber	3D printed; Maximum capacity: 3 cuvettes
3	Portable Power Supply	Self-built power supply, provides constant voltage
4	Dark Box	3D printed; Blocks light from external environment
5	Snapshot Controller	Wireless snapshot controller
6	Cuvettes	Quartz microcuvettes with 1mL volume
7	Smartphone	iPhone 6, used for imaging
8	Cuvette Chamber Stand	Elevate the Dark Box to accommodate phone position

4.1.3. Image Acquisition Procedures

Due to the availability of iPhones, for all experiments we primarily use iPhone 6 as the image detector though other brands of smartphones would work equally well. We downloaded a phone App that allows manual adjustment of focus and exposure during camera mode.

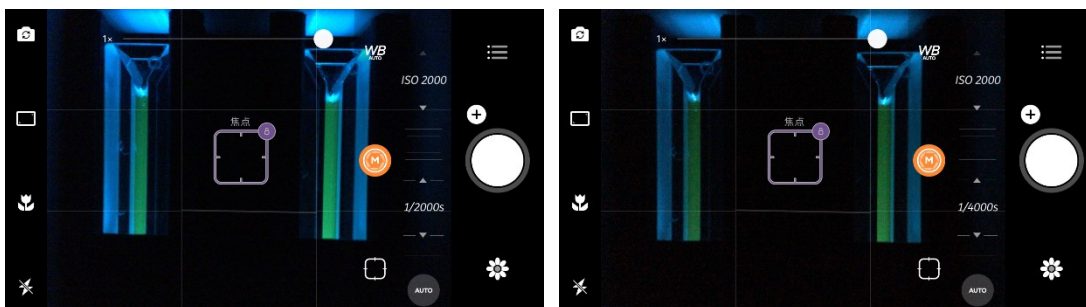
Choosing a steady and consistent reference point during image acquisition is crucially important since it provides a constant reference for all measurements. The most feasible choice for reference point is the black region located in the central area of the enclosure since the RGB values across this region exhibit minimal change. In Figure 4.5, we focused at the top and bottom dark region respectively, and the exposure time and ISO setting for both images are fixed at 1/3000 and 2000. The differential signal on the red highlighted region is plotted below. The experimental result shows that the average variation is around 5 (the total range is 255) for each color channel, and this variation can be further reduced if multiple images are taken.



The focus of one image was on the middle-top region and middle-bottom for the other image. We exported the RGB pixel values over the red highlighted region in both images and then plotted their difference. The green dash line in the plot region approximates the average difference of the two images in terms of pixel values

Figure 4.5: Variation of the signal when focusing at different spots in the middle dark region

LED intensity, exposure time and ISO setting can affect the pixel values of the acquired image. For example, Figure 4.6 shows the two images with the same ISO setting but different exposure times. The color differences from the images can be easily visualized even if the LED intensity and sample concentrations are not changed. Similar situations can also occur when other input parameters are varied. It is possible to create a database recording all possible output images when different input conditions are given, but this process is tedious and time consuming, particularly at this stage of research where most operations are conducted manually.



Left image was acquired at ISO2000, exposure time 1/2000s; right image was acquired at ISO2000, exposure time 1/4000s

Figure 4.6: Images acquired at different exposure time while keeping other conditions identical

Measurements based on the ratio of two channels are less affected by changes in system parameters such as LED intensity, ISO settings and exposure time since the change of values in each color channel can be effectively canceled when their ratio is taken. Therefore, we are prompted to find a set of specific parameter settings where the output produces minimum deviation. Consequently, image data collected using these settings has higher repeatability. The pre-test results in Appendix B, show settings that satisfy these conditions for measurements based on the ratio of the Green channel and the Blue channel:

{LED: 3V, ISO Setting: 2000, Exposure Time: 0.25ms to 0.6ms}

Once the diluted sample assay and hardware apparatus are prepared, the actual image acquisition is conducted according to the following procedures:

- 1) Store the assay sample in 22°C (room temperature)
- 2) Set LED supply voltage to 3V
- 3) Focus onto the black region of the Cuvette Chamber, located in the middle of the scene
- 4) Set ISO to 2000
- 5) Set exposure time to 0.5ms
- 6) Acquire five consecutive images for each concentration measurement
- 7) Repeat steps 2 to 6 for sample temperature at 5°C and 50°C, respectively

4.1.4. Image Processing Results

Once images are collected, they are processed with Matlab and ImageJ. The first important step for image processing is to minimize noise generated from the fluctuations of LED illuminance and the CMOS sensor of the smartphone. Using the noise reduction method mentioned in section 3.5.3, we average the repetitive mages acquired for each measurement. Next, we use ImageJ to manually locate the ROI in the image and calculate the average RGB pixel values in this region as shown in Figure 4.7.

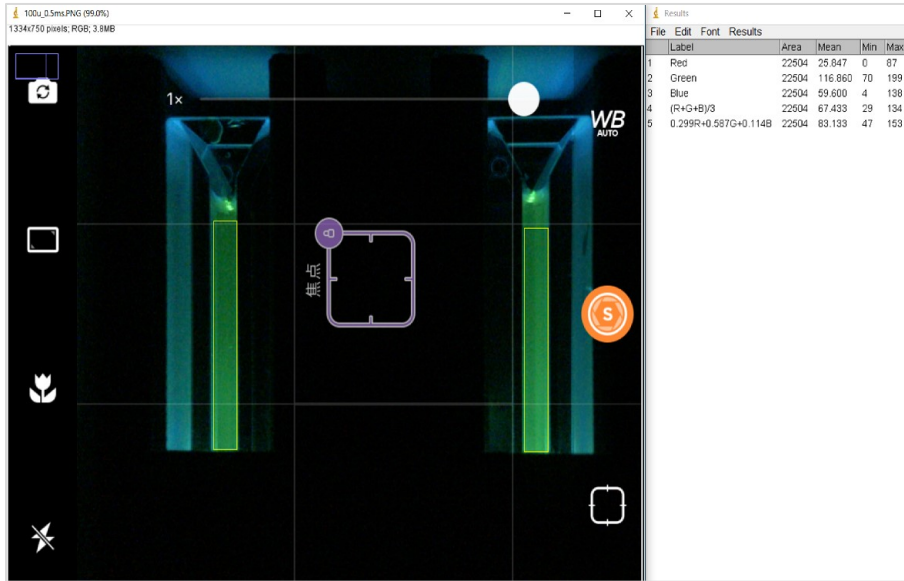
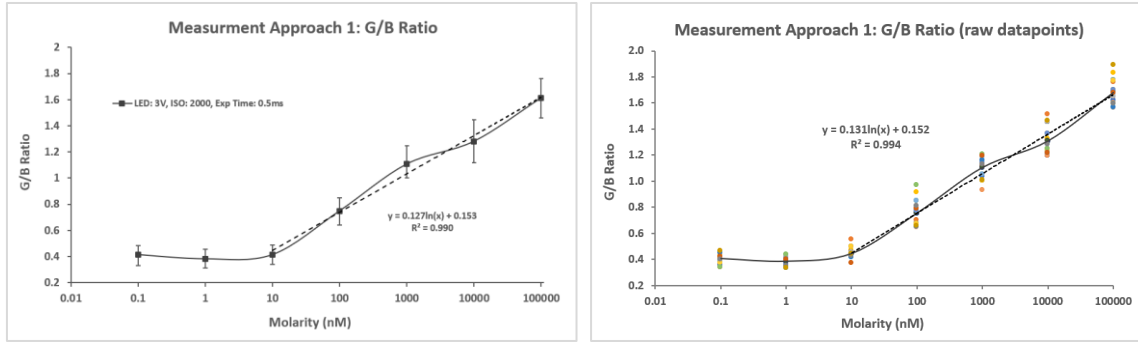


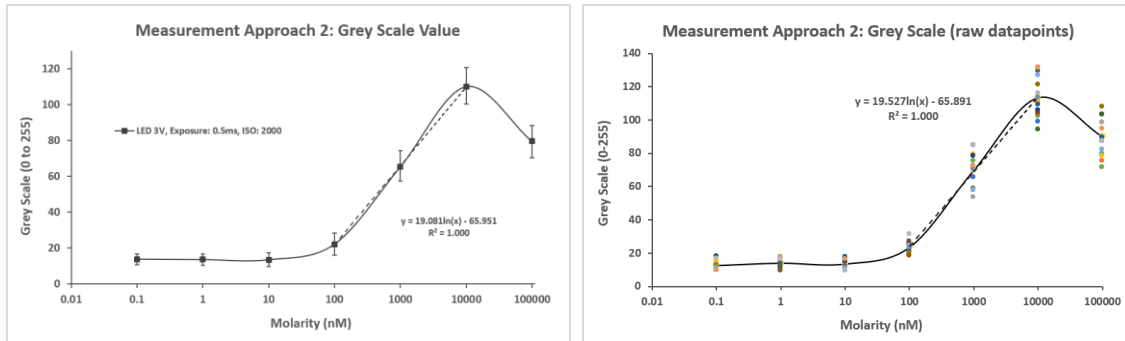
Figure 4.7: Interface of ImageJ showing the selection of ROI and calculation of the average pixel values in this region

By repeating this process for each measurement, a complete RGB dataset corresponding to each sample concentration for varying (known) testing environments can be established. From the RGB dataset, we use the ratio of Green and Blue channel (G/B ratio) and grey scale value as two measurement approaches and plot them against sample concentrations in Figure 4.8 and Figure 4.9, respectively.



In left plot, image data of G/B ratio were first averaged and then plotted against molar concentrations; in right plot, raw image data of G/B ratio were used to plot against molar concentrations. In comparison, plotting with G/B ratio raw data gives a higher R² value which makes the fitting curve matching to the datapoints more closely, but this way may result in higher error bars since image data without averaging are more noisy. In this stage where the data volume is not huge, we will use the left plot (average raw image data then plot) for G/B measurement, but need to keep in mind that if the volume of data increases, the right plot gives more accurate results.

Figure 4.8: G/B ratio vs. molarity at 22°C



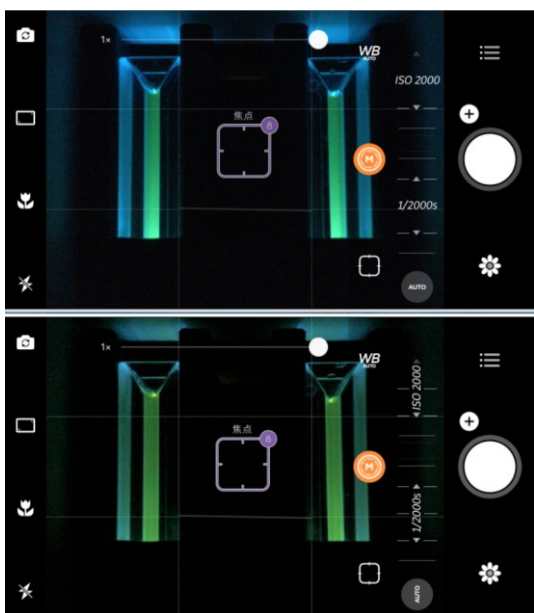
In left plot, image data of Grey Scale value were first averaged and then plotted against molar concentrations; in right plot, raw image data of Grey Scale value were used to plot against molar concentrations. In comparison, plotting with Grey Scale ratio raw data gives a higher R² value which makes the fitting curve matching to the datapoints more closely, but this way may result in higher error bars since image data without averaging are more noisy. In this stage where the data volume is not huge, we will use the left plot (average raw image data then plot) for Grey Scale measurement, but need to keep in mind that if the volume of data increases, the right plot gives more accurate results.

Figure 4.9: Gray scale value vs. molarity at 22°C

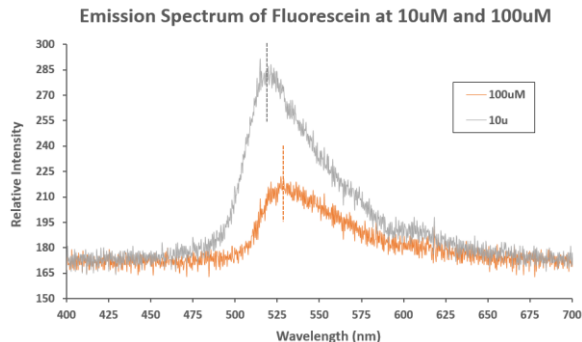
From both of the plots, the intensity reading of the system (vertical axis) exhibits a positive correlation for molarity in range of 10nM to 10μM. Using curve fitting techniques, the response curves can be approximated by logarithmic functions as indicated on the plots.

At 10nM, both measurement approaches begin to lose sensitivity and therefore 10nM can be treated as the detection. For lower concentrations, the emitted fluorescence output signal of the sample is extremely faint and the background noise dominates.

The first obvious disagreement between the two measurement approaches occurs at 100 μ M. In Figure 4.8, G/B ratio is still increasing at this concentration. Higher G/B ratio indicates a larger portion of green spectrum in the total output. In Figure 4.9, the response curve drops at 100 μ M, which means the output intensity also drops. In Figure 4.10 (a) and (b), the difference between 10 μ M and 100 μ M in terms of color and spectrum can be more easily visualized: 10 μ M (upper image) has stronger intensity and shorter peak wavelength, therefore the image is brighter and more blue; 100 μ M (lower image) has lower weaker spectrum magnitude, but the peak wavelength is longer, thus the image appears darker but more green.



(a) Image Data



(b) Spectrum Data

In (a), the upper image is for 10uM and lower image for 100uM. It can be observed that 100uM is greener than 10uM but not as bright as 10uM. This observation can be further consolidated by comparing the spectral plot in (b), which shows that the peak wavelength of 100uM sample fluorescence spectrum is larger but the magnitude is smaller than 10uM sample.

Figure 4.10: Results at 10uM and 100uM obtained from both our system and spectrometer

By comparing the image data in Figure 4.10 (a) to the spectrometer data plot (b), we found both measurement approaches give valid results: from 10 μ M to 100 μ M, the emission spectrum shifts right and its magnitude also drops. This phenomenon can be explained by the inner filter effects of fluorophores caused by the increasing possibility of collisional quenching at high concentrations. To avoid confusion and further complexity involved with detecting high concentrated samples, we set the upper limit detection range of our system to 10uM.

Measurement results at low and high temperatures are plotted in Figure 4.11 and 4.12. The response curves indicate a slight influence on the output readings at different temperatures. However, the trend of the response is the same across the tested temperatures. Therefore, based on the measurement results, we can state the effect of temperature within the range from 5°C to 50°C is minimal, which is advantageous for the development of our product.

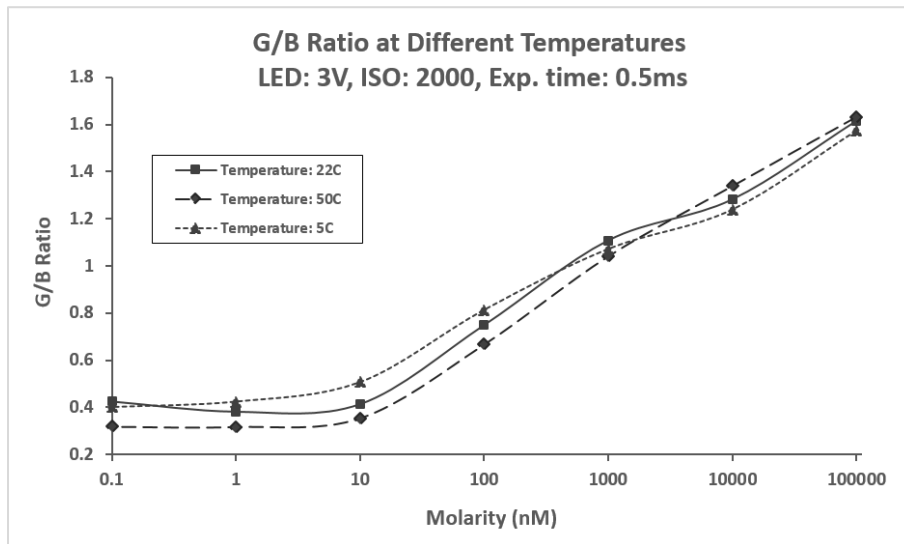


Figure 4.11: Fluorescence intensity at different temperatures, measured by G/B ratio (Fluorescein)

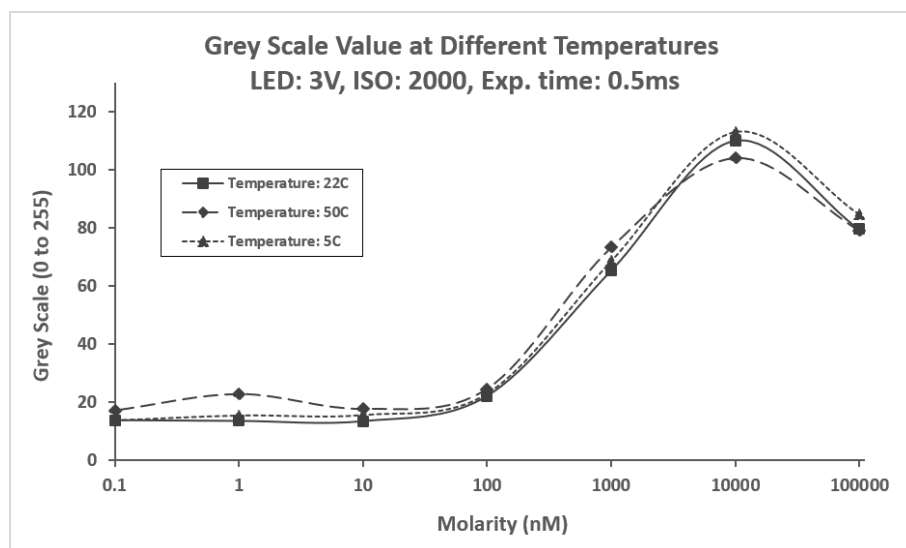


Figure 4.12: Fluorescence intensity at different temperatures, measured by grey scale value (Fluorescein)

4.1.5. Data Analysis

In Table 4-3, we listed some parameters representing the characteristics of the smartphone imaging system with the two measurement approaches.

Table 4-3: Results summary of two measurement approaches (Fluorescein)

	G/B Ratio	Grey Scale
Detection Limit	10nM-10uM	10nM-10uM
Max Repeating Error	42.8%	56.1%
Average Repeating Error	29%	38%
Sensitive Range*	10nM – 10uM	100nM – 10uM
Sensitivity	0.13/10-fold	19.08/10-fold

* Sensitive Range indicates the range of molarity in which a well-defined response curve can be found with a R value of 0.95 or higher.

By comparing the results of the two measurement approaches listed in Table 4-3, the advantages and drawbacks for each approach can be evaluated. The first observation is that Approach 1 (G/B Ratio) has smaller repetition errors than Approach 2 (Grey Scale). Smaller repetition error corresponds to higher repeatability, which implies the measurement results are more precise. Another advantage with Approach 1 is its larger

sensitivity range. In this range, a logarithmic function can be defined to closely fit the response curve, and it is also possible to find the inverse function of the fitted curve. For example, in Figure 4.11 the fitting curve for G/B Ratio is modeled as:

$$y_1 = 0.13 \ln(x_1) + 0.15 \quad (19)$$

where y is the G/B ratio value and x is molarity. By finding the inverse function of the above equation, the estimated concentration or molarity y_2 can be calculated by the relation:

$$y_2 = 0.315e^{7.69(x_2)} \quad (20)$$

where x is the G/B ratio measured by the system using Approach 1. Regardless of the repetition error and sensitivity range, Approach 2 has much higher sensitivity in the region from 100 nM to 10 μ M. In this region the fitted curve and its inverse function can be expressed as:

$$y_3 = 19.08 \ln(x_3) - 66.5 \quad (21)$$

$$y_4 = 32.63e^{0.0524(x_4)} \quad (22)$$

By comparing the characteristic curves of the two systems above, equation 22 (the Grey Scale approach) gives a more precise mapping from intensity to concentration than equation 20 (the G/B approach).

4.1.6. Error Analysis

Light Source

Light source is a crucial part of our device. Any fluctuation or instability of the LED irradiance will directly affect the output, thereby producing errors in the measurements. Mathematically, we express the actual RGB values as:

$$R = r + \delta r$$

$$G = g + \delta g$$

$$B = b + \delta b$$

where r , g , b are the 8-bit channel values given by the smartphone raw image data, and the fluctuation of the light source is approximated as $\delta r = 5$, $\delta g = 10$, $\delta b = 8$ based on our pre-test results in Section 3.2.1. As the intensity of the emission light is weaker than that of the excitation light, the maximum fluctuation of the output signal should not exceed δr , δg and δb . Using the error propagation formulas, the propagated error for each measurement approach is:

$$\text{Error \% (G/B)} = \sqrt{\left(\frac{\delta g}{g}\right)^2 + \left(\frac{\delta b}{b}\right)^2} \times 100\% \quad (23)$$

$$\text{Error \% (Grey Scale)} = \sqrt{(\delta r)^2 + (\delta g)^2 + (\delta b)^2} \times 100\% \quad (24)$$

Equation 23 and 24 estimate the measurement errors due to the light source at each point, which allows us to calculate the propagation error for G/B and grey scale at each concentration. For example, at 100nM, the propagations error for G/B and grey scale are $\pm 12\%$ and $\pm 15\%$ respectively.

Camera Focusing

Another process that introduces errors is manual focusing. We would like to use a constant black region of the image as the reference ground, and this is implemented by focusing onto the steady and smooth black region of the enclosure for each acquisition. Since focus is set manually, tiny displacements while setting focus locations each time cannot be avoided. According to the differential signal plot in Section 4.1.3, RGB errors caused by manual focusing will be approximately $\delta r = 0.5$, $\delta g = 5$ and $\delta b = 1$. Again, when we use 100nM as an example, the propagated error for G/B and Grey Scale approaches will be $\pm 4.7\%$ and $\pm 5.1\%$, respectively.

Pipetting Errors

The pipettes used while preparing assay samples also introduce errors. Two pipettes we are using while preparing assay samples have nominal volume of 1000uL and 10uL and each of them can produce $\pm 2\%$ relative error based on each pipet's nominal volume. Typically, from the stock solution of 0.1 M to the target concentrations in the measurement, two or three rounds of dilution are needed. For example, the process of making a 100nM solution is given as:

$$0.1\text{M} \times \left[\frac{10\text{uL}}{10\text{uL} + 990\text{uL}} \right] \left[\frac{10\text{uL}}{10\text{uL} + 990\text{uL}} \right] \left[\frac{10\text{uL}}{10\text{uL} + 990\text{uL}} \right] = 100\text{nM}$$

and the error propagation of the above dilution process is then calculated as:

$$3 \times \frac{\sqrt{\left(\frac{0.2}{10}\right)^2 + \left(\frac{\sqrt{0.2^2 + 19.8^2}}{1000}\right)^2}}{0.01} \times 100\% = 8.4\%$$

Thus, the actual concentration may have $\pm 8.4\%$ fluctuation from the target 100nM concentration. The actual pipetting error may be slightly higher since this calculation does not include the pipetting error associated with making the original stock solution.

By simply adding the errors calculated from each section, the total error for 100nM will be $\pm 25.1\%$ for G/B ratio and $\pm 28.5\%$ for Grey Scale. In actual experimental data, the repetition error of 100nM is $\pm 21.4\%$ for G/B ratio and $\pm 28.1\%$ for Grey Scale, which are within the expected error range.

4.1.7. Image Database for Fluorescein

The processed image data collected from multiple sets of experiments helps to construct a database of fluorescein results. As a final constituent of the system, the sole functionality of the image database is to map the measurement results based on pixels values to assay concentrations or molarities. Based on the system diagram illustrated in Section 3.1, the database for fluorescein is constructed as follows:

Input Condition:

1. Assay sample: Fluorescein
2. System Parameters:
 - Light Source: 482nm Cyan LED
 - Smartphone: iPhone 6
 - LED: 3V, ISO Setting: 2000, Exposure Time: 0.25ms to 0.6ms
3. Temperature: 5°C to 50°C

Measurement Data:

Data acquired from the imaging device are the measured results of G/B ratio and grey scale values which are denoted as:

$$G, B \text{ Ratio: } M \pm m$$

$$\text{Grey Scale Value : } N \pm n$$

where m and n are the average repeating error of each measurement approach, which is 29% and 38% in this stage; these values may vary slightly as the number of samples is further increased.

Output Results:

For our system, each measurement produces a pair of data, M and N , which will be used to approximate the molarity of the sample according to the following three cases:

Case 1: If $0.8 < M \leq 1.4$, it means the molarity is within 100nM to 10uM. In this range using grey scale value is demonstrated to be more accurate, thus the concentration y with maximum and minimum possible uncertainties is calculated as:

$$y(\text{max, min}) = 32.63e^{0.0524(N \pm 38\%)} \quad (25)$$

Case 2: For $0.4 < M \leq 0.8$, molarity is within 10nM to 100nM, and the concentration should be approximated by G/B ratio, thus we have:

$$y(\max, \min) = 0.315e^{7.69(M \pm 29\%)} \quad (26)$$

Case 3: For $M < 0.4$ and $N < 20$, the molarity is 10nM, which is lower than the detection limit of our system.

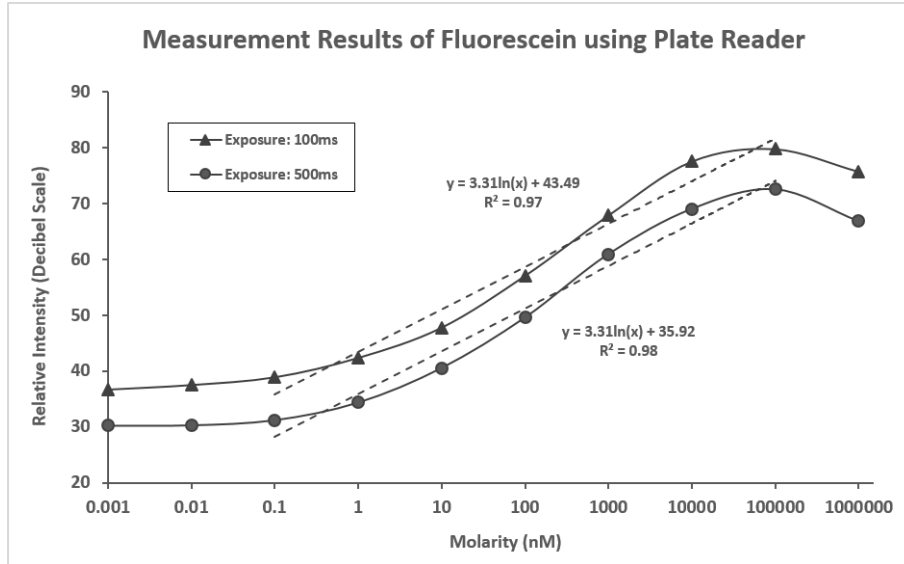
4.1.8. Comparison

The experimental results obtained from our device were compared with a commercial plate reader (VICTOR™ X5 Multilabel Plate Reader). As shown in Figure 4.13, a black 96 well plate is used to prepare fluorescein samples. With this setup, crosstalk among adjacent wells can be effectively eliminated. A 10-fold serial dilution is applied across each well starting with a 0.1M fluorescein stock solution in the leftmost well that appears reddish in Figure 4.13. For the 12th well in each row, we used water as a control reference for the test.



Figure 4.13: Serially diluted fluorescein sample prepared in 96 well plate

Measurement starts from the fifth well of each row (10μM) to compare with the results of the smartphone system. We used two exposure times, 0.1s and 0.5s. The fluorescence intensities measured at each concentration are plotted in Figure 4.14. It is noticeable that changing the exposure time shifts the entire curve but does not affect the detection limit and sensitivity of the system.



The vertical axis of the curves is in decibel (dB) scale, which is calculated as $10 \cdot \log(P_{out}/P_{in})$. Using this scale, we can use curve fitting method to determine a linear trendline with a constant slope for each curve, which is 3.31 for both curves as shown in figure. Error bars are not shown in the plot for clarity of the figure.

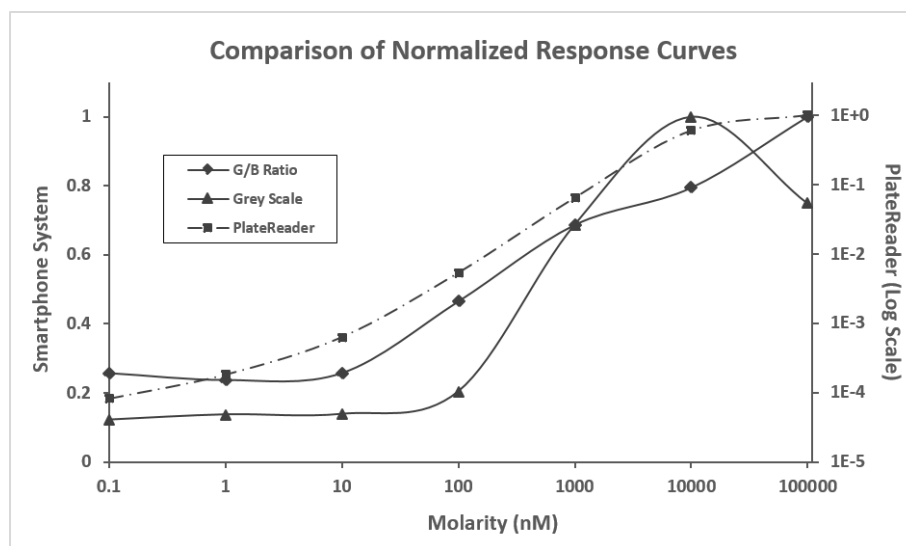
Figure 4.14: Measurement results of the fluorescein test using a VICTOR X5 plate reader

Table 4-4: Plate reader measurement results at different exposure times (Fluorescein)

	Exposure: 100 ms	Exposure: 500 ms
Detection Limit	0.1nM	0.1nM
Max Repeating Error	88.9%	76.3%
Average Repeating Error	64%	68%
Sensitive Range	0.1nM-100uM	0.1nM-100uM
Sensitivity (dB)	3.31dB/10-fold	3.31dB/10-fold

Both Maximum Repeating Error and Average Repeating Error are computed based on the measurement results of eight samples (8 rows of the 96 well plate)

The response curves of the plate reader tend to be linear within the sensitive region from 10nM to 100µM in log-log scale, whereas for our smartphone-based imaging device the response is linear in linear-log scale. Due to the differences in the detection and processing mechanisms, it is not surprising that the two systems exhibited different response curves. Nevertheless, we can extract information such as detection limit, sensitivity and repeatability from each graph and compare the performance of the two systems. To this end, we used merged two plots in one graph in Figure 4.15 for comparison.



The axis scale for smartphone system is Log-Linear scale for platereader it is Log-Log scale.

Figure 4.15: Comparison of response curves of the smartphone based system and commerical platereader

The plot shows that the plate reader can detect much lower concentrations than the smartphone imaging device. This is mainly due to the photomultiplier embedded in the plate reader that amplifies the number of emission photons. For the smartphone imaging device, the detection limit is largely constrained by the photon sensitivity and color depth of the smartphone camera. However, in the range where both systems exhibit high sensitivity [10nM to 10 μ M], the smartphone-based imaging sensor gives more accurate and precise results in terms of quantifying concentrations.

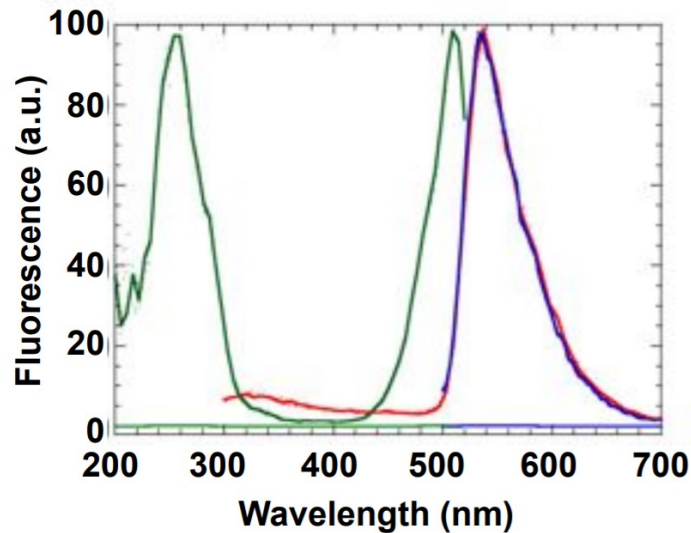
4.2. RNA Mango

4.2.1. RNA Mango Properties

RNA Mango is a high affinity RNA aptamer that amplifies the fluorescence signal of RNA, allowing the purification of fluorescently tagged RNA complexes to be tracked in real time. RNA mango can rapidly bind a series of thiazole orange fluorophore derivatives, referred to as TO1, with nanomolar affinity, while increasing the fluorescence intensity by up to 1,100-fold [42]. The amplified fluorescence signal by RNA mango enhances the visualization of single molecules under fluorescence microscopy, thus

enabling the potential for live-cell RNA imaging. Also, by inserting RNA Mango into a stem loop of the bacterial 6S RNA and biotinylating the fluorophore, the aptamer shows the capability to fluorescently label and purify biologically important RNAs at the same time [43].

The absorption and emission spectrum of RNA Mango is illustrated in Figure 4.16. It has two absorption maxima located at 260 nm and 510 nm. The maximum emission wavelength of RNA mango is 535 nm, which is a green dominant color.



RNA Mango can be excited using both 270nm deep UV light and 500nm green light. The CMOS image sensor on smartphone does not response to deep UV, thus using deep UV as excitation source is a preferred option as the acquired images will not contain exciting photons

Figure 4.16: Absorption and emission spectrum of RNA Mango

RNA Mango has a large separation in wavelengths between its first absorption maxima and emission maxima, which is known as the *Stoke shift*. The lowest detectable wavelength for both human eyes and CMOS image sensors in smartphones is around 400 nm. We can use a deep UV, which has a peak wavelength less than 300 nm, to excite RNA Mango. Consequently, the scattering of input light will not affect the measurement results significantly.

4.2.2. Experimental Setup

To quantify RNA Mango concentrations, we prepared a series of samples of RNA Mango and TO1Biotin (the dye). Dye concentration is held at 500nM, while RNA is diluted serially using 5-fold dilutions as shown in Table 4-5. A 0 M RNA sample was prepared as a control to measure the fluorescence of the dye alone.

Table 4-5: Molarities of each serially diluted RNA Mango sample

Serial Number	RNA Molarity (nM)
1	500
2	100
3	20
4	4
5	0.8
6	0.16
7	0.032
8	0 (control)

To excite the RNA Mango, we used a deep UV LED with peak wavelength at 278nm for the light source, which makes it undetectable by the smartphone camera. The UV LED is mounted on an aluminum-based board for better heat dissipation and, thus, has a different shape than the cyan LEDs used in previous experiments. The UV LED is powered at its nominal voltage at 8V. Due to its relatively high cost, only one deep UV LED is used for the light source of the hardware system.

A new enclosure was designed to accommodate the UV LED, sample container and detector as shown in Figure 4.17. The same quartz cuvette as with previous methods was used to hold the RNA mango sample because of its excellent transparency to deep UV light (less than 12% absorption at 270nm). We used the same right angle setup for the light source and cuvette to minimize excitation light captured by the image detector. Once the top cover and phone are properly placed, the entire enclosure should isolate any external backlight. For camera setting, we used a fixed ISO setting and exposure time (ISO: 2000, Exposure time: 1/1000s) while acquiring images.

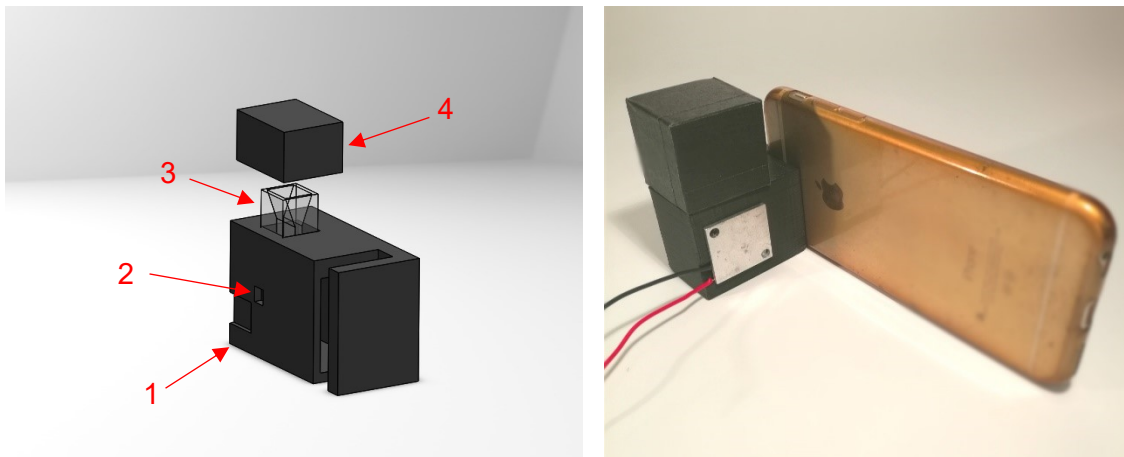


Figure 4.17: Hardware setup for RNA Mango experiment; each part is labeled and explained in Table

Table 4-6: Illustration of each part in Figure 4.17

Label	Name	Description
1	Dark Box Enclosure	Positioning cuvette and smartphone
2	UV LED Hold	A special hold for 280nm UV LED light entrance
3	Cuvette with RNA Mango	Quartz cuvette, allowing transmission of deep UV
4	Top Cover	Block external backlight from the system

4.2.3. Experimental Results

RNA mango glows green-yellowish light when it is excited by deep UV. The captured image is shown in Figure 4.18.

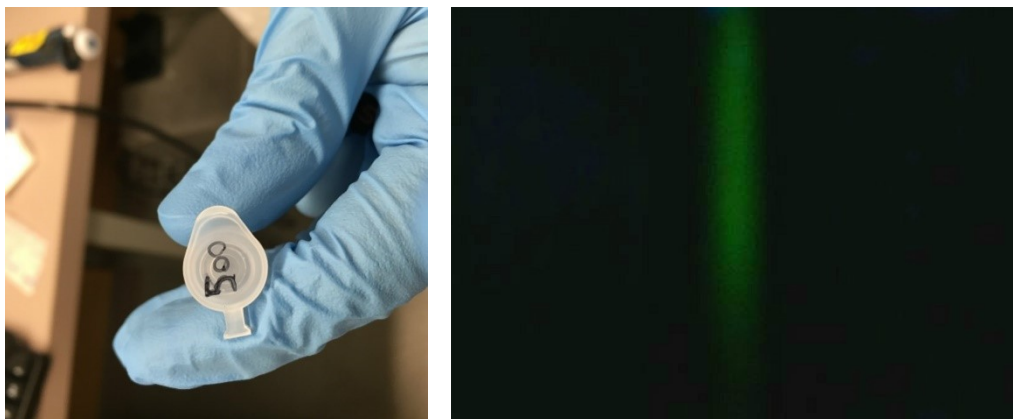


Figure 4.18: Detected image of a 500nM RNA Mango sample

Following the same image processing steps, we computed the average pixel values within the region of interest; these pixel values are further converted to G/B ratio and Grey Scale, as shown in Figure 4.19 and Figure 4.20. The engineering performance of the two measurement approaches is listed in Table 4-7.

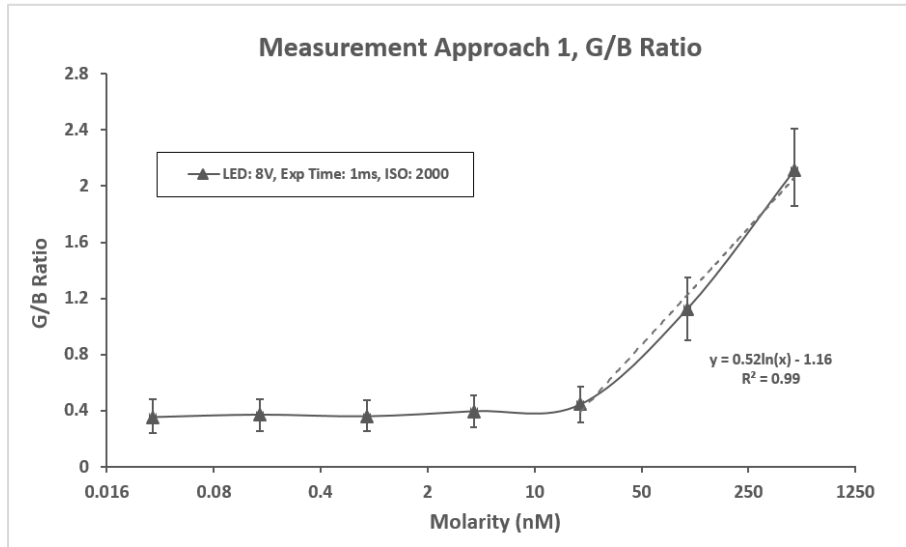


Figure 4.19: G/B ratio vs. molarity measured at 22°C (RNA Mango)

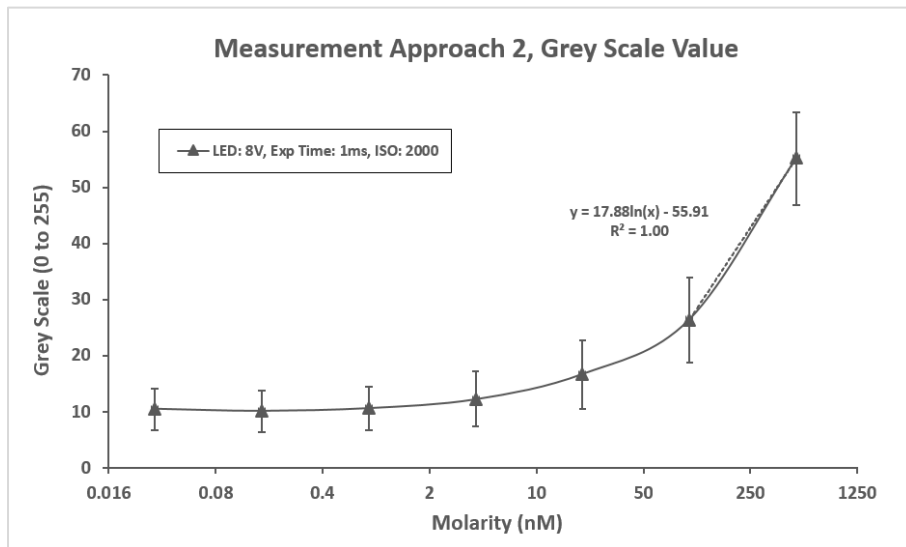


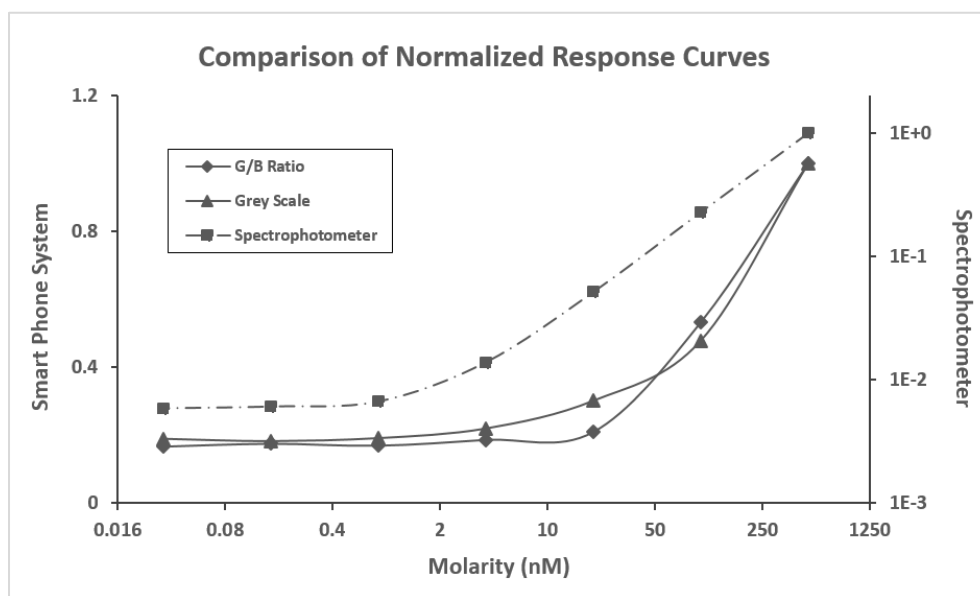
Figure 4.20: Grey scale value vs. molarity measured at 22°C (RNA Mango)

Table 4-7: Results summary of two measurement approaches (RNA Mango)

	G/B Ratio	Grey Scale
Detection Limit	20 nM	20 nM
Max Repeating Error	68.4%	75.3%
Average Repeating Error	53%	65%
Sensitive Range	> 20 nM	> 100 nM
Sensitivity	0.52/5-fold	17.88/5-fold

4.2.4. Comparison

Samples were tested for fluorescence using the device made for iPhone imaging as well as a 96 well plate reader (SpectraMax M5). The plate reader samples were excited at 495nm and emission was read at 535nm with a cut-off low pass filter (allowing pass of lower frequency or higher wavelength) at 515nm. In Figure 4.21, we merged the plot of G/B ratio, Grey scale and the plate reader in one plot for comparison.



The axis scale for smartphone system is Log-Linear scale for plater reader it is Log-Log scale.

Figure 4.21: Comparison of response curves of the smartphone based system and spectrophotometer

The plot shows that spectrophotometer is able to detect lower RNA mango concentrations than using the smartphone imaging device. The main reason of spectrophotometer's advantage on detection limit is also due to the photomultiplier tube which dramatically amplifies the intensity of output light. Nevertheless, in range of 10nM

to 10 μ M, the smartphone imaging device exhibits higher accuracy and smaller repetition error in terms of quantifying concentrations of RNA mango.

4.3. Summary

In this chapter we analyzed the performance of the smartphone-based imaging device to quantify the concentration of fluorescent materials. Selected fluorescent sample assays include fluorescein and RNA Mango. A dedicated hardware system for standard cuvettes was designed to provide an ideal environment for placement of optic components and detection of fluorescence signals. Image acquisition was done with smartphone cameras. The acquired images were further processed by Matlab and ImageJ to generate meaningful data and plots that can be used to estimate the concentration of the sample solution. These results were evaluated with respect to detection limit, sensitivity, repeatability and accuracy. The comparison of these parameters with those from commercial plate readers, show that the commercial instruments offer higher sensitivity and lower detection limit. However, the smartphone imaging system, although less sensitive, exhibited superior repeatability and accuracy while quantifying the concentrations of the solutions within its sensitive range.

Chapter 5.

Scattering-based Measurements

5.1. Methods

5.1.1. Types of Mixtures

In this context, mixture refers to a material in liquid state that is made by physically mixing multiple substances that do not chemically react with each other. Mixtures can be classified as homogeneous mixtures and heterogeneous mixtures. Homogeneous mixtures have the same composition in every part of the mixture, therefore, the physical properties are identical throughout. In contrast, the components of heterogeneous mixtures are not uniformly distributed throughout the mixture. Based on homogeneity, the sample can be classified as a solution, a colloid or a suspension. The characteristics of these different sample classifications are listed in Table 5-1. Suspensions are settleable mixtures, meaning the solute actively precipitates out of solution. Suspensions are physically unstable and, therefore, are not included in our experiments.

Table 5-1: Physical properties of solution, colloid and suspension

	Solution	Colloid	Suspension
Homogeneity	Homogenous	Semi-homogenous	Heterogeneous
Particle Size	<3 nm	3-3000 nm	>3000 nm
Settleability	Non-settleable	Non-settleable	Settleable

In homogenous solutions the diameter of dissolved particles is usually less than 3 nm, which is much smaller than the wavelength of visible light. When light passes through the solution, these particles are too small to cause any obstacles to the traversing beam of light, thus, solutions appear transparent. Samples reported in Chapter 4 are all homogenous solutions.

Colloids are treated as semi-homogenous mixtures because particles in colloids cannot be completely dissolved but are evenly distributed throughout the liquid. The sizes of these particles are usually bigger than 3nm, which is in a comparable range to the wavelength of visible light. Therefore, in colloids, the probability of incident photons

colliding with these particles is much higher than in solutions. Collision will refract the incident light photons, thus causing light to scatter. This phenomenon is also known as the *Tyndall Effect* [43]. The Tyndall Effect allows the interaction between photons and particles to be visualized, which gives the possibility of quantifying the concentration of colloid mixtures using our smart phone imaging system.

An example in Figure 5.1 shows the Tyndall Effects of different concentrations of water-diluted milk. The only variable that changes in this example is the concentration of the milk, and higher concentrations appears cloudier than lower concentrations.



Figure 5.1 [44]: Scattering effects of milk at different concentrations

5.1.2. Light Interactions with Colloidal mixtures

Generally, absorption and scattering may occur when light interacts with a colloid that contains multiple chemical constituents. Absorption occurs when the incoming photons have the same vibrational frequency as the particles that absorb these photons, or absorbers. The energy of radiation that is absorbed by the absorbers is transformed into vibrational energy, which is eventually converted to heat. Once a photon is absorbed, it will not be released in the form of light, causing the intensity of incident light to be attenuated. Absorption is wavelength dependent since materials made up of atoms and molecules can have different vibrational frequencies, and these atoms and molecules are only absorptive to certain frequencies of electromagnetic radiation. Scattering deflects or

diffuses the path of photons, and this type can be classified as Rayleigh scattering or Mie scattering depending on the size of the scatterers. If the diameter of the scatterers is much smaller than the wavelength of incident light, Rayleigh scattering is dominant. In Rayleigh scattering, light is uniformly deflected, and the intensity observed from all directions are almost the same. For larger scatterers with sizes comparable to the wavelength of incident light, Mie scattering begins to dominate. In Mie scattering, light forms a forward lobe which produces stronger light intensity in the forward direction.

The size of particles in colloid is in range of 3 to 3000 nm and, therefore, satisfies the condition for Rayleigh and Mie scattering. For a polychromatic light source containing radiation of multiple wavelengths, mathematical modelling of scattering is very challenging because most equations and formulas developed are based on monochromatic light only [45]. Nevertheless, the system ensures that all hardware setup, such as light source spectrum, beam path, camera setup, incident angle and observing angle, are all identical while measuring the same substance. A quantitative relationship between the intensity of scattered output light and sample concentration can be approximated using the color-based methods as illustrated in Section 3.4.

5.1.3. Quantification Methods

Measuring the concentrations of biological samples by Absorbance

A common and effective technique to quantify the concentration of biological cultures in microbiology is to measure the absorbance or optical density (OD) of the sample. Measurements of OD are usually conducted using Spectrophotometers or power meters. As illustrated in Section 2.1.2, a spectrophotometer quantifies absorbance by comparing the intensity of the light beam that passes through the liquid sample with the original intensity of the beam before entering the liquid. The optical density OD is then calculated by:

$$OD = \frac{-\log_{10}\left(\frac{I_{out}}{I_{in}}\right)}{L} \quad (27)$$

Where

I_{OUT} and I_{IN} are the intensities of output light and input light

L is the thickness of the sample

The proportional relationship between absorbance and the concentration of photon absorbing species in the sample make it possible to estimate the concentration of cells in a much faster way than the traditional microscopic cell counting method [46]. Figure 5.2 shows the growth of a bacterial culture in which the population and different growth phases are quantified by monitoring the absorbance.

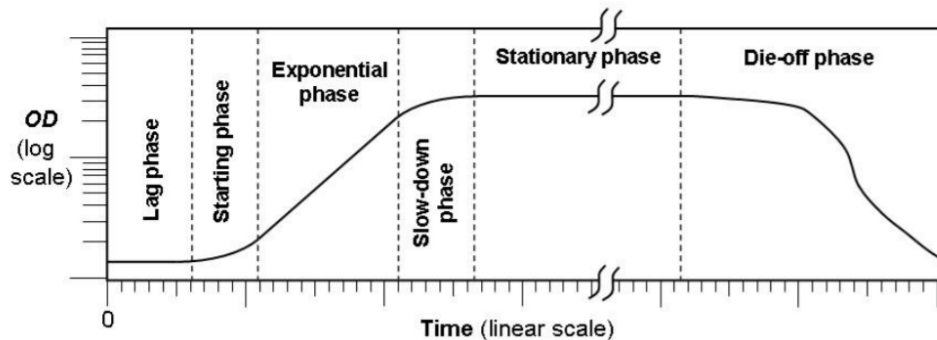


Figure 5.2 [47]: Phases in a bacterial culture measured with OD

Measuring the concentrations of biological samples using our Imaging System

The current hardware and enclosure of the smartphone imaging system is designed for right-angle illumination setup to maximize the amount of emission light received by the image detector. For consistency, the same hardware and algorithm described earlier was used in this experiment. When comparing fluorescence-based measurements and scattering based measurements, the main difference is the presence of the stoke shift. For fluorescence-based measurements, the process of absorption and reemission takes place, thus, the output light has a different spectrum compared to the input light. For scattering based measurements, output scattered light is caused by physical collisions between photons and particles in the liquid, thus, the spectrum of the output light is the same as that of the input beam, though the magnitude can vary. Considering the spectroscopic properties of colloids, a presumption can be made that the smartphone imaging system would also be

capable of measuring and quantifying the concentration of colloids using the same hardware setup, imaging acquisition and processing techniques as illustrated in Chapter 3.

5.2. Homogenized Milk

5.2.1. Material Properties

Over 95% of the fat in milk exists in the form of droplets or globules. In raw milk, the size of these fat globules can range from 0.1 to 15 μm [48]. Some of these globules are large enough leading to the development of large clusters and cream, which reduces the shelf-life of milk. To increase milk's shelf-life, a process called homogenization is applied. The homogenization process emulsifies milk to reduce the fat globules to uniform and smaller sizes in range of 0.5-2 μm , which are too small to form cream [49].

Homogenized milk is a colloidal solution, more specifically, an oil-in-water emulsion that contains fat globules, casein micelles and other soluble substances such as proteins, lactose, vitamins and minerals. A microscopic view of the homogenized milk is shown in Figure 5.3. The big droplets are undissolved fat globules suspended in the solution. The smaller dark dots stick around the fat globules are casein micelles, and their approximated sizes range from 50nm to 300nm according to the scale shown on the image.

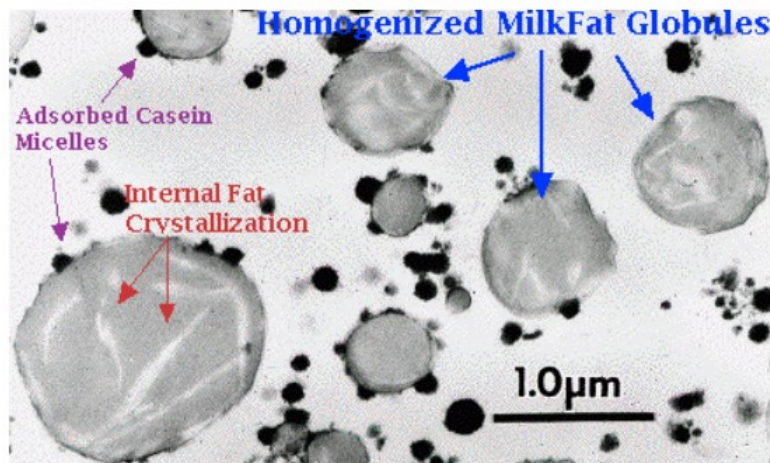


Figure 5.3 [50]: Microscopic view of fat particles in homogenized milk

5.2.2. Experimental Setup

Sample Preparation

The milk samples used in this experiment were freshly produced homogenized milk from Dairyland (a milk producer in Canada). We chose partly skimmed milk (2% fat) as the sample to be tested, which corresponds to 20g/L of fat based on the nutrition facts provided by the producer. The fat percentage of the milk sample was serially diluted using a 5-fold dilution (Table 5.2). All samples are placed into 1 mL quartz cuvettes for testing.

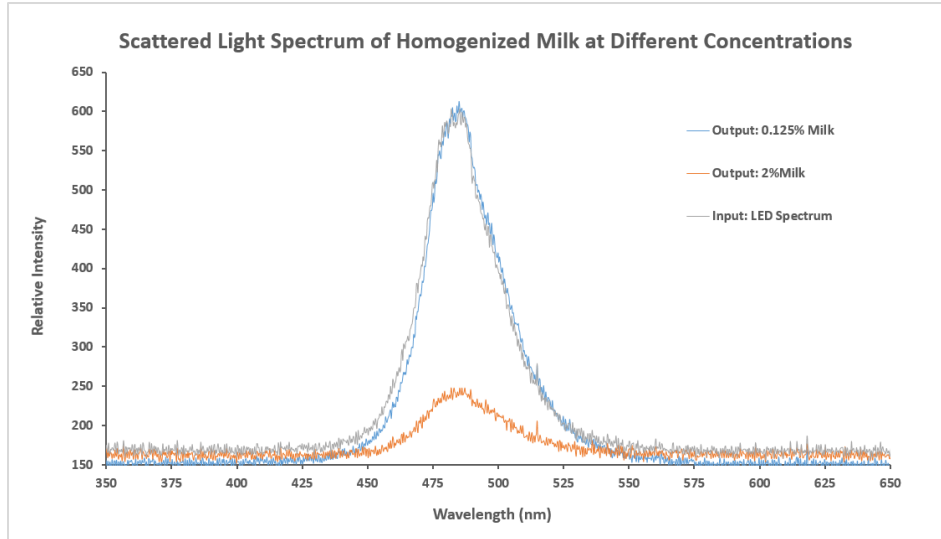
Table 5-2: Concentrations of serially diluted homogenized milk samples

Serial Number	5-Milk Fat Conc. (mg/L)
1	4000
2	800
3	160
4	32
5	6.4
6	1.3
7	0 (Water control)

5.2.3. Experimental Results

Measurements using a Spectrometer

First, we used a spectrometer with a right-angle setup to measure the scattered light intensity for the different concentrations of milk fat. Measurement data are plotted in Figure 5.4, which shows that the spectrum of input and output light has no phase shift, only a change in magnitude. When the concentration exceeds a certain value, the large number of fat particles that can act as scatterers have a higher probability of blocking the exiting photons. Therefore, the output light intensity ceases to increase. This concentration value can be treated as the upper detection limit of the spectrometer.



Using a spectrometer (model: SPM-002-E), we measured the scattered light of 0.125% milk (blue curve) and 2% milk samples (orange curve). The spectrum of the scattered light has no phase shift but only changes in magnitude. Noticeably, the magnitude of 2% milk spectrum is less than 0.125% since the large number of fat particles block the exiting photons. The upper detection limit of our system can be determined based on the condition that the scattered light magnitude begins to show an inverse proportionality to the concentration of milk

Figure 5.4: Scattered light spectrum of homogenized milk at 0.125% and 2%

Measurements using our Imaging System

The experiments in this chapter used the same hardware system as in fluorescence-based measurements. For consistency, iPhone 6 was again used as the image detector for the experiment. We manually focused on the middle dark region of the enclosure to provide a constant pixel reference for all images. The ISO setting and exposure time were fixed to 2000 and 1ms respectively during image acquisition. The entire imaging process will be repeated 5 times to allow computing the error bars. In this stage that experiments are conducted manually and consuming vast time, we did not attempt for larger number of tests, though more repeating times would provide more accurate data for statistics.

Images acquired at each concentration are processed using the same techniques explained in Chapter 3: regions of interest are manually selected using ImageJ, and in the selected region we computed the G/B ratio and grey scale value. The G/B ratio at each milk concentration (approach 1) is plotted in Figure 5.5 and grey scale values verses milk concentrations (approach 2) are plotted in Figure 5.6.

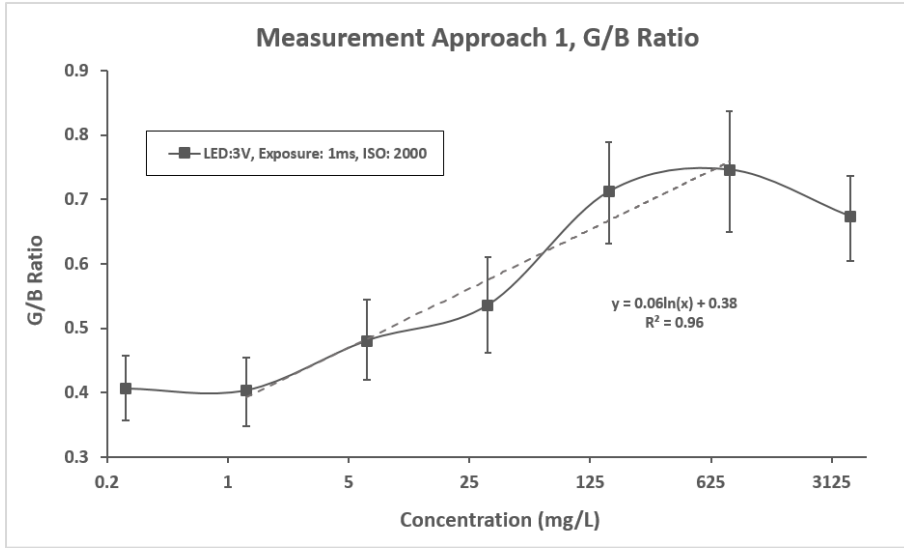


Figure 5.5: G/B ratio vs fat concentrations of milk, measured at 22°C (2% Milk)

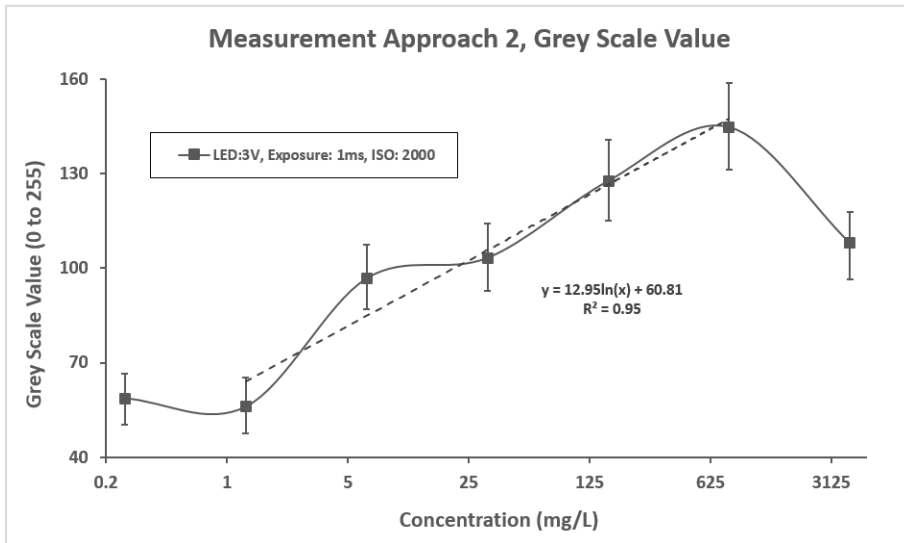


Figure 5.6: Grey scale value vs fat concentration of milk, measured at 22°C (2% Milk)

The test results of each measurement approach in this milk experiment are summarized in Table 5-3. The repeating error with G/B ratio approach is slightly better, but has much lower sensitivity than using grey scale approach. Unlike fluorescence, the scattered light in this experiment is in phase with the spectrum of input cyan LED, of which the spectrum can be effectively sensed by both Green and Blue pixels of the smartphone image sensor. If the system uses the ratio of Green and Blue pixel values to measure the

concentration change, the response curve could be relatively flat. On the other hand, the phase shift of output light spectrum has less effects to the grey scale approach, since it is mainly affected by the magnitude of the spectrum instead of phase.

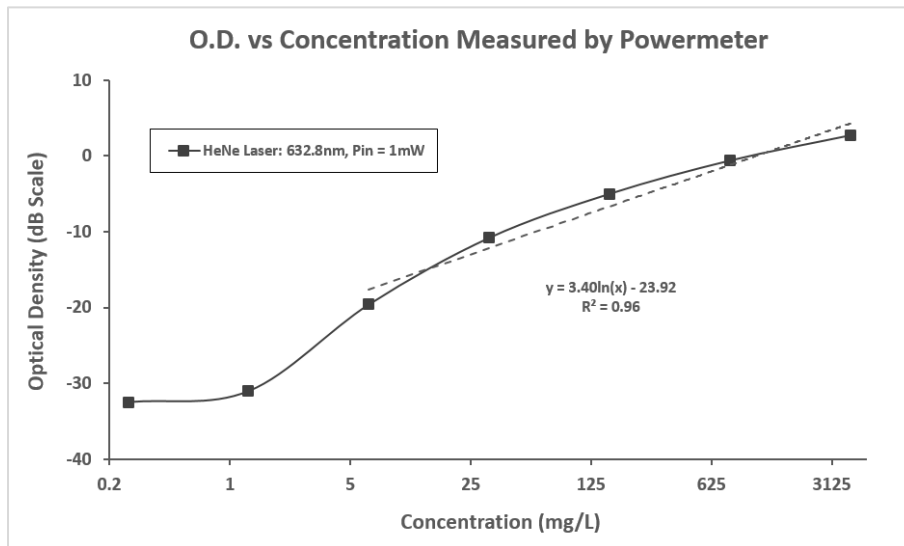
Table 5-3: Results compared by two measurement approaches (2% Milk)

	G/B Ratio	Grey Scale
Detection Limit	1.28-800 mg/L	1.28-800 mg/L
Max Repeating Error	27.7%	27.8%
Average Repeating Error	24.9%	25.4%
Sensitive Range*	1.28 – 800 mg/L	1.28 – 800 mg/L
Sensitivity	0.06/5-fold	12.95/5-fold

Both Maximum Repeating Error and Average Repeating Error are computed based on 5 test results of the same experimental setup and procedure

Measurements using a Power Meter

We also replicated the experiment and measured the concentration of fat in the milk samples using a power meter. This setup was comprised of a dark room, a 0.5mW@632nm Ne-He laser (REO, Model: 31004) that illuminates the sample from one side of the quartz cuvette, and a power meter (Newport DPM, Model: 815) aligned from the opposite side of the cuvette. The intensities of both incident light and output light at each concentration were recorded, and their ratios were plotted against sample concentrations. In Figure 5.7, the response curve of a power meter measuring system is plotted in logarithmic scale, and its performance, including detection limit and sensitivity, is characterized in Table 5-4.



The vertical axis of the curves is in decibel (dB) scale, which is calculated as $10 \cdot \log(P_{out}/P_{in})$. Using this scale, we can use curve fitting method to determine a linear trendline with a constant

slope for the response curve, which is 3.40 as shown in figure. Error bars are not shown in the plot for clarity of the figure.

Figure 5.7: Optical density vs fat concentration of milk measured by powermeter

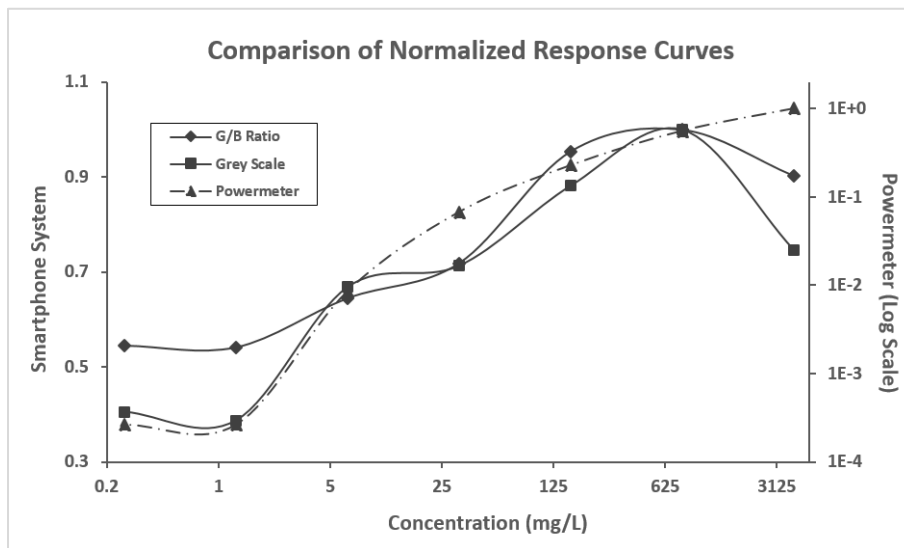
Table 5-4: Measurement results obtained by powermeter (2% Milk)

Power Meter	
Detection Limit	6.4-4000mg/L
Max Repeating Error	75.8%
Average Repeating Error	46%
Sensitive Range*	6.4 – 4000mg/L
Sensitivity	3.40dB/fold-5

Both Maximum Repeating Error and Average Repeating Error are computed based on 5 test results of the same experimental setup and procedure

5.2.4. Comparison

In Figure 5.8, all response curves are normalized and placed in a single plot for clearer comparison.



The response curves of the smartphone system and powermeter (Model: DPM-815) are scaled such that their maximum value is 1; this allows them to be fitted in the scale from 0 to 1 for better comparison the two systems. It should be noted that power meter uses log scale in vertical axis.

Figure 5.8: Comparison of response curves of the smartphone based system and power meter (fat concentration in homogenized milk)

By comparing the plots, powermeter measurement is more sensitive than the smartphone device and it can measure milk sample with higher concentrations. However, in the range from 10nM to 10uM, the smartphone imaging device gives more accurate and

precise results in terms of quantification of fat concentrations in milk (25% of average repeating error of our system, and 46% of average repeating error of the power meter).

5.3. Saccharomyces Cerevisiae

5.3.1. Material Properties

Saccharomyces cerevisiae (or *S. cerevisiae* in short), also known as brewing yeast, is a type of yeast strain that has been intensively studied. *S. cerevisiae* is a unicellular eukaryotic organism that has a single nucleus enclosed within a membrane. As it shares many properties with animal and plant cells, such as cell structure and life cycle, and is easily cultivated, *S. cerevisiae* is widely accepted as a model organism for the study of eukaryotes [51]. Figure 5.9 shows the microscopic view of *S. cerevisiae* cells in a colloidal solution. The cells are spherical or egg shaped, and their average size is approximately 5 μm in diameter, which satisfies the condition of particle size of colloids. As a colloid where particles are evenly distributed, these cells are large enough to cause deflection of a light beam and, therefore, produce a scattering effect.

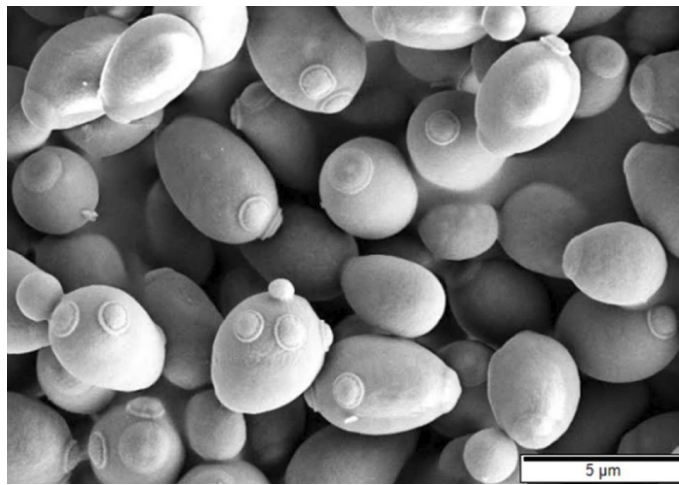


Figure 5.9 [52]: *Saccharomyces cerevisiae* under electronic microscope

Yeast cells can divide and grow rapidly when conditions such as temperature, sugar concentrations and pH of the growth medium are optimal [53]. A typical growth curve of yeast cells in yeast extract peptone dextrose is shown in Figure 5.10. This curve shows the four different yeast growth phases: lag, log, deceleration and stationary. In lag phase, no

growth occurs since the newly introduced yeast cells are adjusting to the environment. In the log phase, cells will grow and divide rapidly, which results in an exponential increase of the colloid concentration. After multiple hours of rapid growth, the mixture reaches a saturated density and the growth process begins to decelerate (deceleration phase), culminating in the maintenance of a steady concentration level (stationary phase).

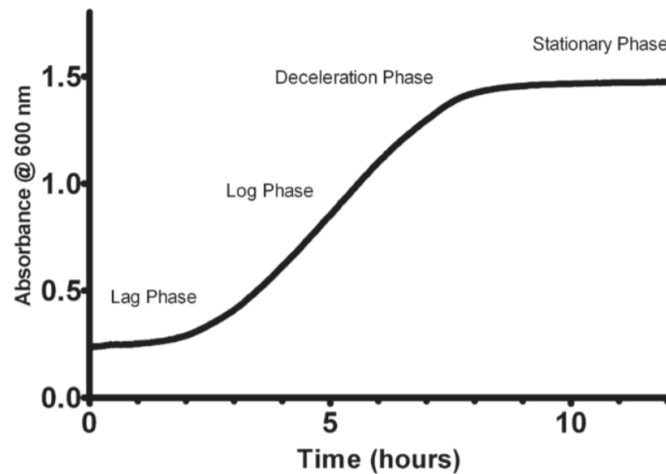


Figure 5.10 [54]: Typical yeast growth curve, measured by absorbance at 600nm red laser beam

5.3.2. Experimental Setup

Given the growth characteristics of *S. cerevisiae* cells in a suitable growth media, the concentration being measured generally does not remain constant across time. In a typical growth curve, the speed of cell growth changes and replication is particularly fast in log phase. Measuring in cell concentrations while cells are still replicating and growing should be avoided since the established database could map to wrong values. To solve this problem, the growth speed of cells should be kept as slow as possible during measurement by ensuring that the entire process from assay preparation to data acquisition is completed before the yeast enter the log phase of their growth curve.

The stock solution was obtained by mixing 230 mg of dry *S. cerevisiae* powder with 10 mL of deionized, distilled water. Once thoroughly mixed, the mixture is then transferred into 1mL quartz cuvettes for serial dilutions. Table 5-5 gives the density of the mixture after each dilution, which reflects the relative amount of *S. cerevisiae* cells.

Table 5-5: Concentration of serially diluted yeast samples

Serial Number	Yeast Conc. (mg/L)
1	23000
2	4600
3	920
4	184
5	36.8
6	7.36
7	1.47
8	0.29

Similar to the experiment in Section 5.2, we used a cyan LED as the input light source. For camera settings, ISO and exposure time are fixed at 2000 and 1ms, respectively. The total time for acquiring all image data was within 10 minutes, which precedes the stage of rapid cell growth and replication. The experiment was conducted at room temperature.

5.3.3. Experimental Results

Measurement results for *S. cerevisiae* using the G/B ratio and grey scale approaches are plotted in Figure 5.11 and Figure 5.12, respectively. The response curves exhibit similar shapes as in the homogenized milk experiment. From 7.36 mg/L to 4600 mg/L, our system shows a linear response to the changing of yeast concentrations. For more concentrated sample (e.g. 23 g/L), collisions among photons and scatterers take place more dramatically which prevent light photons exit from the colloid. Once the system response curve reached to a point where the concentration and system output values (G/B ratio or grey scale value) begin to show negative correlation, it indicates the upper detection limit of the system. The lower detection limit can also be easily found at the turning point where the curve slope transit from positive to zero.

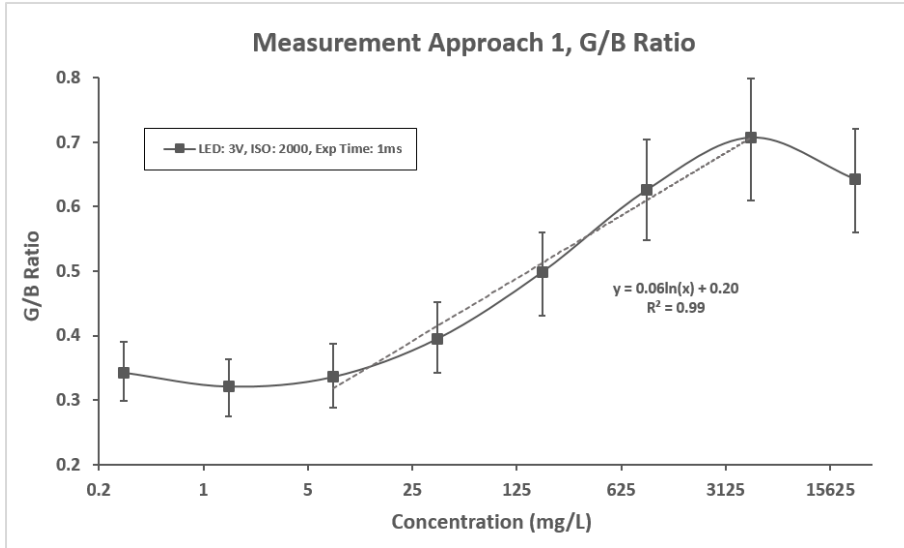


Figure 5.11: G/B ratio vs. concentration, measured at 22°C (Yeast)

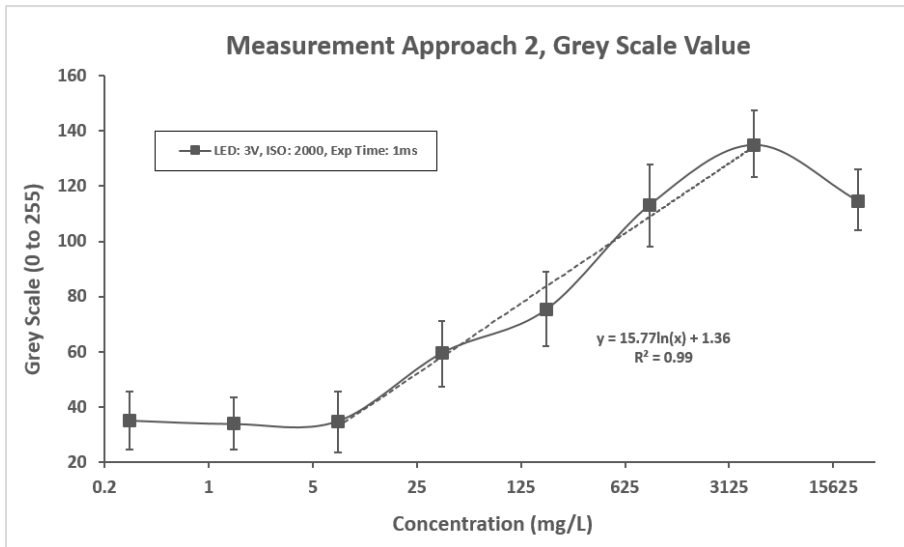


Figure 5.12: Grey scale value vs. concentration, measured at 22°C (Yeast)

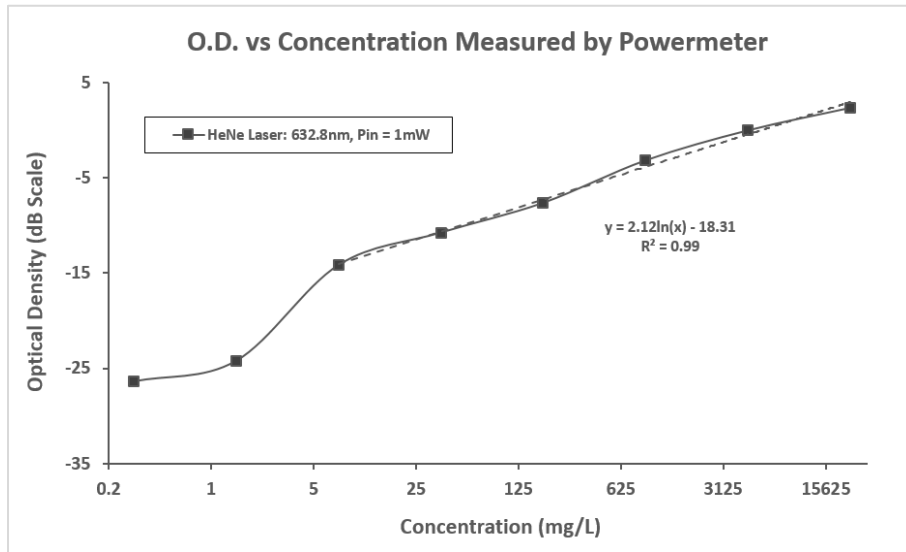
From Figure 5.11 and Figure 5.12, the upper and lower detection limit and other parameters such as sensitivity and repetition errors can be quantified in Table 5-6.

Table 5-6: Results compared by two measurement approaches (Yeast)

	G/B Ratio	Grey Scale
Detection Limit	7.36-4600 mg/L	7.36-4600 mg/L
Max Repeating Error	39.4%	29.3%
Average Repeating Error	27.8%	31.6%
Sensitive Range*	7.36 – 4600 mg/L	7.36 – 4600 mg/L
Sensitivity	0.06/5-fold	15.77/5-fold

5.3.4. Comparison

Again, we measured the same yeast sample using powermeter setup. The same 632nm Ne-He Laser was used as the input light incident from one side of the cuvette and output light power was measured on the opposite side of the cuvette. The logarithm of the power ratio at each concentration was taken as the system output reading, and the response curve was plotted in Figure 5.13. The same test was repeated 5 times.



The vertical axis uses decibel scale, which is calculated as: $10 \cdot \log(P_{out}/P_{in})$. Using curve fitting method, the slope of the linear fitted trendline is 2.12 with R^2 equal to 0.99.

Figure 5.13: OD vs concentration, measured at 22°C

Table 5-7: Measurement results obtained by powermeter (Yeast)

	Power Meter
Detection Limit	7.36-23000mg/L
Max Repeating Error	81%
Average Repeating Error	51%
Sensitive Range*	7.36 – 23000mg/L
Sensitivity	2.12dB/fold-5

Both Maximum Repeating Error and Average Repeating Error are computed based on 5 test results using the same experimental setup and procedure.

In the end, we compared the response curve of our device to the power meter measurement system. The curves are scaled such that they can merge into a single plot, as shown in Figure 5.14.

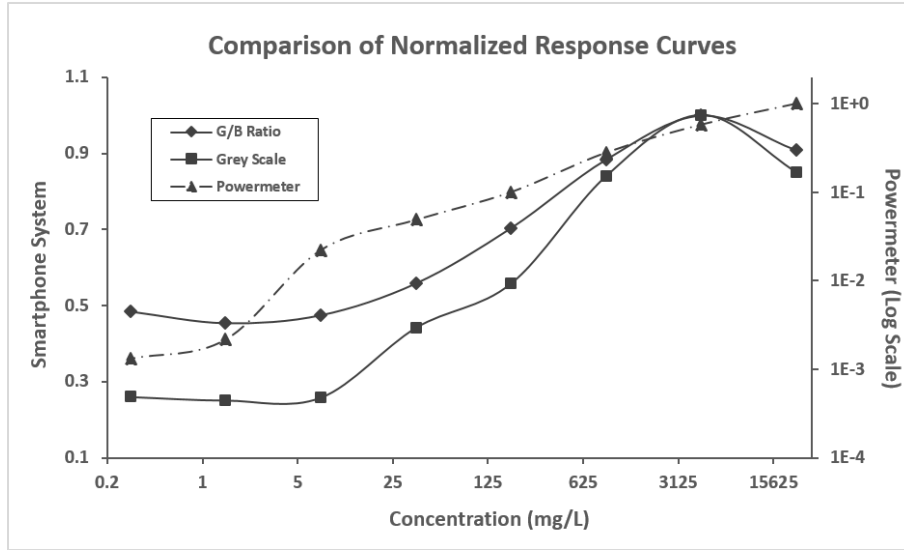


Figure 5.14: Comparison of response curves of the smartphone based system and power meter (yeast)

As expected, our system shows the advantage on the measurement accuracy and precision in a certain concentration range of yeast cells but is less sensitive to the changing of concentrations.

5.4. Summary

In this chapter, we demonstrated that the implementation of the smartphone-based imaging device can be also applied to the measurement of the concentration of non-fluorescent materials, given the precondition that these materials are present in colloidal states and the particle sizes are within the range of 3-3000 nm. The main goal in this chapter was to explore the possibility of using of the scattering property of light. When the particles of the colloid scatter light, the trajectory of photons, will be changed, which causes a change in the proportion of incident photons that hit the image detector compared to a clear liquid. For colloids with higher concentrations, more particles are presented in the sample, thereby increasing the photon detection probabilities. As a result, our system will detect a larger output signal. Using the sample methodology illustrated in Chapter 3, we conducted experiments on homogenized milk and yeast. Engineering performance such as detection limit, sensitivity and precision are characterized based on experimental results. The experimental results showed that our smartphone device is more accurate and precise for

quantifying the colloid concentrations in certain range, but is less sensitive and has narrower detection limit range than using a traditional Laser-Power meter setup.

Chapter 6.

Conclusion and Future Work

6.1. Conclusion

In this project we explored the concept of using smartphones as the sensor to detect and quantify the concentration of several biological samples. Our studies focused on fluorescent materials and colloidal mixtures. A portable and compact hardware system was built to accomplish the following essential requirements of the experiment:

- Provide secure housing for standard cuvettes
- Eliminate light interference from the external environment
- Create a right-angle layout for excitation and emission light
- Fix the position of the observing smartphone

Procedures for image acquisition and data processing were also established for the system to generate precise and consistent results throughout experiments. From the collected measurement results of each experiment, we constructed a database which allows the estimation of chemical concentrations of samples, interpreted from acquired image data.

To compare the performance of our system, all experiments conducted were also replicated using commercial instruments such as microplate readers, spectrophotometers and power meters. As expected, commercial instruments demonstrated better performance, particularly with respect to the detection limit and sensitivity of concentration changes. However, the smartphone-based imaging system exhibited relatively good ranges of detection limits and sensitivities and performed better than commercial instruments with regards to its repeatability. Our demonstrated device is small, portable and inexpensive, which makes it remarkably suitable for quick tests and experiments conducted in areas where electrical power is unreliable or not available.

6.2. Future Work

The proposed smartphone imaging system is a comprehensive device that involves hardware design, image acquisition and data processing. This research could be expanded in the following by future projects by exploring:

- **Choices of light source:** Our system used cyan LEDs and deep UV LEDs as the only candidates of light source. LEDs are inexpensive, and several choices are available for different wavelengths and intensities. On the other had, it is also worthy to investigate the performance of semiconductor lasers as the light source since they produce high intensity collimated light. Semiconductor lasers are also becoming economical. For fluorescence measurement, using a laser as the input light source can produce stronger fluorescence signal, thus, potentially increasing the detection limit of the system. However, using a laser might require specialized circuits to enable intermittent excitation and measurement to avoid photobleaching.
- **Candidate samples:** In this thesis, we demonstrated the entire experimental process, from setup to final quantification of fluorescein, RNA mango, homogenized milk and *Saccharomyces cerevisiae*. In the future, we could construct a database for more fluorophores that have significance in chemistry and molecular biology.
- **Data collection:** Appendix D outlines the preliminary prototype of the modified version of the smartphone imaging device. This prototype is designed to allow continuous and automated operation of the system. While collecting data, the smartphone should be set to video recording mode. In this manner, the efficiency of data collection can be rapidly increased, and the final data processing can be implemented on frame images of the video. With more sample data feeding into the statistical modelling of the system, and perhaps employing other data mining techniques, the device can evolve into a more accurate and precise instrument.

References

- [1] Patrik Cerwal, Peter Jonsson, Stephen Carson, "Ericsson Mobility Report," Ericsson, 2017.
- [2] C. Matasaru, *Mobile Phone Camera Possibilities for Spectral Imaging*, CIMET, 2014.
- [3] Zhu H, Sikora U, Ozcan A, "Quantum dot enabled detection of Escherichia coli using a cell-phone," *The Analyst*, vol. 137, p. 2541, 2012.
- [4] Qingshan Wei, Hangfei Qi, Wei Luo, Derek Tseng, So Jung Ki, Zhe Wan, Zoltán Göröcs, Laurent A. Bentolila, Ting-Ting Wu, Ren Sun, and Aydogan Ozcan, "Fluorescent Imaging of Single Nanoparticles and Viruses on a Smart Phone," *ACS Nano*, vol. 7, pp. 9147-9155, 9 September 2013.
- [5] X. Amouretti, "Impact of HTS on Multidetector Microplate Readers and Benefits For Life Science Research Laboratories," 1 August 2006. [Online]. Available: <https://www.americanlaboratory.com/913-Technical-Articles/19675-Impact-of-HTS-on-Multidetector-Microplate-Readers-and-Benefits-For-Life-Science-Research-Laboratories/>. [Accessed 14 February 2018].
- [6] "Multimode Plate Readers," PerkinElmer Inc, Waltham, 2011.
- [7] J. Geisler, "Choosing the Best Detection Method: Absorbance vs. Fluorescence," 7 May 2015. [Online]. Available: <https://www.biocompare.com/Bench-Tips/173963-Choosing-the-Best-Detection-Method-Absorbance-vs-Fluorescence/>. [Accessed 2 June 2018].
- [8] P. Bouguer, *Essai d'optique sur la gradation de la lumière*, Paris: Claude Jombert, 1729, pp. 16-22.
- [9] María-Leonor Pla, Sandra Oltra Crespo, María-Dolores Esteban, Santiago Andreu, Alfredo Palop, "Comparison of Primary Models to Predict Microbial

Growth by the Plate Count and Absorbance Methods," *BioMed Research International*, 2015.

- [10] R Krishna, T.J.Unsworth, R.Edge, Reference Module in Materials Science and Materials Engineering,, Elsevier, 2016.
- [11] "Hyperphysics," [Online]. Available: <http://hyperphysics.phy-astr.gsu.edu/hbase/atmos/blusky.html#c1>. [Accessed 23 June 2018].
- [12] "Widefield fluorescence microscopy: What you need to know," Scientifica, [Online]. Available: <https://www.scientifica.uk.com/learning-zone/widefield-fluorescence-microscopy#>. [Accessed 2 Aug 2018].
- [13] Meiresonne, Nils & Alexeeva, Svetlana & van der Ploeg, Rene & Blaauwen, Tanneke, "Detection of Protein Interactions in the Cytoplasm and Periplasm of Escherichia coli by Förster Resonance Energy Transfer," *BioProtoc*, vol. 8, no. 2, 2018.
- [14] J. H. Hardesty, "Spectrophotometry and the Beer-Lambert Law: An Important Analytical Technique in Chemistry," 2010. [Online]. Available: <http://www.collin.edu/chemistry/Handouts%202009/Beer's%20Law.pdf>. [Accessed 30 June 2018].
- [15] Heidi Hofer, Joseph Carroll, Jay Neitz, Maureen Neitz, David R. Williams, "Organization of the Human Trichromatic Cone Mosaic," *The Journal of Neuroscience*, vol. 25, no. 42, pp. 9669-9679, 2005.
- [16] J. K. Bowmaker, H. J. A. Dartnall, "Visual pigments of rods and cones in a human retina," *Physiol*, vol. 298, pp. 501-511, 1980.
- [17] Adrian Ford, Alan Roberts, "Colour Space Conversions," 11 August 1998. [Online]. Available: <https://poynton.ca/PDFs/coloureq.pdf>. [Accessed 21 June 2018].

- [18] D. RD, "A nonlinear model for transient responses from light-adapted wolf spider eyes.," *The Journal of General Physiology*, vol. 50, pp. 1993-2030, 1967.
- [19] "National Center for Biotechnology Information," PubChem Compound Database, [Online]. Available: <https://pubchem.ncbi.nlm.nih.gov/compound/16850>. [Accessed 10 July 2018].
- [20] "Brandtech," [Online]. Available: <https://www.brandtech.com/wp-content/uploads/cuvettegraph.pdf>. [Accessed 4 July 2018].
- [21] "Comparison with Quartz and other Plastic Cuvettes," [Online]. Available: <https://www.brandtech.com/wp-content/uploads/cuvettegraph.pdf>. [Accessed 9 July 2018].
- [22] "An Introduction to Fluorescence Spectroscopy," PerkinElmer, Beaconsfield, 2000.
- [23] Smith DS, Kostov Y, Rao G, Gryczynski, Malicka J, Gryczynski Z, Lakowicz JR, "First observation of surface plasmon-coupled emission due to LED excitation.," *Journal of Fluorescence*, vol. 15, pp. 895-900, 2005.
- [24] Jeff W Lichtman, Jose-Angel Conchello, "Fluorescence microscopy," *Nature Methods*, vol. 2, no. 12, p. 914, 2005.
- [25] "Texas Instrument," 2013. [Online]. Available: <http://www.ti.com/lit/ds/symlink/lm2577.pdf>. [Accessed 4 May 2018].
- [26] K. R. Spring, "Fluorescence Microscopy," in *Encyclopedia of Optical Engineering*, Marcel Dekker, 2003, p. 550.
- [27] DeRose, Paul C., "Recommendations and Guidelines for Standardization of Fluorescence Spectroscopy," National Institute of Standards and Technology, Gaithersburg, 2007.
- [28] "Fluorescein, Oregon Green and Rhodamine Green Dyes—Section 1.5," ThermoFisher, [Online]. Available:

<https://www.thermofisher.com/ca/en/home/references/molecular-probes-the-handbook/fluorophores-and-their-amine-reactive-derivatives/fluorescein-oregon-green-and-rhodamine-green-dyes.html#head1>. [Accessed 2 May 2018].

- [29] DAVE LITWILLER, DALSA, "CMOS vs. CCD: Maturing Technologies, Maturing Markets," Photonics Media, August 2005. [Online]. Available: https://www.photonics.com/a22471/CMOS_vs_CCD_Maturing_Technologies_Maturing. [Accessed 9 July 2018].
- [30] Wong, H. P; Chang, R. T; Crabbe, E; Agnello, P. D, "CMOS active pixel image sensors fabricated using a 1.8-V, 0.25- μm CMOS technology," *IEEE Transactions on Electron Devices*, vol. 45, no. 4, pp. 889-894, 1998.
- [31] "Inside the iPhone 6 and iPhone 6 Plus," chipworks, 2 October 2014. [联机]. Available: <https://www.chipworks.com/about-chipworks/overview/blog/inside-iphone-6-and-iphone-6-plus-part-3>. [访问日期: 22 September 2018].
- [32] C. Thomas, "How smartphone cameras work – Gary explains," 8 May 2017. [Online]. Available: <https://www.androidauthority.com/smartphone-cameras-explained-767029/>. [Accessed 31 May 2018].
- [33] T. Schiesser, "Know your smartphone: a guide to camera hardware," 28 July 2014. [Online]. Available: <https://www.techspot.com/guides/850-smartphone-camera-hardware/>. [Accessed 12 June 2018].
- [34] Hiscocks, Peter D., "Measuring Luminance with a Digital Camera," 14 February 2014. [Online]. Available: <https://www.ee.ryerson.ca/~phiscock/astronomy/light-pollution/luminance-notes-2.pdf>. [Accessed 9 April 2018].
- [35] Antonie J.W.G. Visser, Olaf J. Rolinski, "BASIC PHOTOPHYSICS," PHOTOBIOLOGICAL SCIENCES ONLINE, 2016. [Online]. Available: <http://photobiology.info/Visser-Rolinski.html#TOP>. [Accessed 9 May 2018].

- [36] Markus Sauer, Johan Hofkens, Jörg Enderlein, Handbook of Fluorescence Spectroscopy and Imaging: From Ensemble to Single Molecules, Wiley-VCH Verlag GmbH & Co. KGaA, 2011, p. 15.
- [37] Dragoş MIHAI, Eugen STRĂJESCU, "FROM WAVELENGTH TO RGB FILTER," *The Scientific Bulletin Series D*, vol. 69, no. 2, p. 82, 2007.
- [38] "Fluorescence SpectraViewer," ThermoFisher, [Online]. Available: <https://www.thermofisher.com/ca/en/home/life-science/cell-analysis/labeling-chemistry/fluorescence-spectraviewer.html>. [Accessed 14 February 2018].
- [39] J. Van Houten, R. J. Watts, "Temperature dependence of the photophysical and photochemical properties of the tris(2,2'-bipyridyl)ruthenium(II) ion in aqueous solution," *Journal of American Chemical Society*, vol. 98, no. 16, pp. 4853-4858, 1976.
- [40] Y. H. & A. K. H. & T. S. Wong, "Honey-Induced Protein Stabilization as Studied by Fluorescein Isothiocyanate Fluorescence," *The Scientific World*, no. 1, 2013.
- [41] P. E. K.-S. E. A. H. M. T. K. K. N. Jason J. Nichols, "The Use of Fluorescent Quenching in Studying the Contribution of Evaporation to Tear Thinning," *Investigative Ophthalmology and Visual Science*, vol. 53, no. 9, pp. 5426-5432, 2012.
- [42] Dolgosheina EV, Jeng SC, Panchapakesan SS, Cojocaru R, Chen PS, Wilson PD, Hawkins N, Wiggins PA, Unrau PJ., "RNA mango aptamer-fluorophore: a bright, high-affinity complex for RNA labeling and tracking," *ACS Chemical Biology*, vol. 9, no. 10, pp. 2412-20, 2014.
- [43] E. O. Kraemer, S. T. Dexter, "The Light-Scattering Capacity (Tyndall Effect) and Colloidal Behavior of Gelatine Sols and Gels," *The Journal of Physical Chemistry*, vol. 31, no. 5, pp. 764-782, 1927.

- [44] "Scattered in Blue," 26 April 2013. [Online]. Available: <http://thestandardmodel.blogspot.com/2013/04/when-i-was-child-i-often-wonder-why-sky.html>. [Accessed 2 June 2018].
- [45] Quangsang Vo, Peng Feng, Wei Biao, "Study on Properties of Light Scattering Based on Mie Scattering Theory for Suspended Particles in Water," in *Optics Frontier—The 6th International Conference on Information Optics and Photonics*, 2014.
- [46] Brian C. Matlock, Richard W. Beringer, David Ash, Michael W. Allen, A. Freddie Page, "Analyzing Differences in Bacterial Optical Density Measurements between Spectrophotometers," ThermoFisher Scientific.
- [47] F. Widdel, "Theory and Measurement of Bacterial Growth," 5 June 2010. [Online]. Available: <https://www.mpi-bremen.de/Binaries/Binary307/Wachstumsversuch.pdf>. [Accessed 28 March 2018].
- [48] "Using Laser Diffraction to Measure the Size and Stability of Dairy Emulsions," Malvern Panalytical, 31 May 2017. [Online]. Available: <https://www.azom.com/article.aspx?ArticleID=13760>. [Accessed 19 March 2018].
- [49] Jukkola A, Rojas OJ, "Milk fat globules and associated membranes: Colloidal properties and processing effects.," *Advances in Colloid and Interface Science*, vol. 245, pp. 92-101, July 2017.
- [50] H. D. Goff, *Milkfat Structure - Fat Globules*, University of Guelph Food Science.
- [51] ZHOU Jia, KANG Ya-Ni, "A model organism for cellular aging research: *Saccharomyces cerevisiae*," *Chinese Bulletin of Life Sciences*, vol. 25, no. 5, pp. 511-517, 2013.
- [52] M. Murtey, P. Ramasamy, "Sample Preparations for Scanning Electron Microscopy – Life Sciences," in *Modern Electron Microscopy in Physical and Life Sciences Milos Janecek*, IntechOpen, 2016, p. 163.

- [53] F. NoéArroyo-López, SandiOrlić, AmparoQuerol, EladioBarrio, "Effects of temperature, pH and sugar concentration on the growth parameters of *Saccharomyces cerevisiae*, *S. kudriavzevii* and their interspecific hybrid," *International Journal of Food Microbiology*, vol. 131, no. 2-3, pp. 120-127, 2009.
- [54] H, Alsuheim & Vojisavljevic, Vuk & Pirogova, Elena. (2012). Alsuheim, H. Vojisavljevic, V. and Pirogova, "Effects of non-thermal microwave exposures on the proliferation rate of *saccharomyces cerevisiae* yeast," in *WC2012 World Congress on Medical Physics and Biomedical Engineering*, Beijing, 2012.

Appendix A.

Designing a Microplate-based Imaging System

A standard microplate has 96 wells thus allowing 96 samples to be tested by a single experiment. To fully make use of the sample wells, most microplate-based sensing instruments have adopted the 180-degree photometry mechanism, which indicates that input light source illuminates the assay from bottom and the output light can be picked up from top of the plate. In this mechanism, output light is a mixture of the signal of interest, which is usually the fluorescence signal, and background noise from input light source. Before the output light reaches to the amplifying photodetector, a sharp-edge low pass filter or monochromator must present beforehand to eliminate the unwanted portion. The 180-degree optical setup allows experiments to be conducted efficiently, however, it also requires many supplementary parts during operation.

Alternatively, we designed a microplate reader using 90-degree geometry for optical setup. The preliminary prototype is exhibited in Figure A.1. This model allows a smartphone camera to detect the signal directly from observation hole on top of the device. Furthermore, the dimension of the entire unit is 30cm x 30cm x 15cm, with gross weight less than 1kg and the whole system can be powered by a single 9V battery. The above specifications satisfy the basic requirements for a stand alone portable device. However, while running, the system consumes about 2W electrical power to drive the mechanical parts, which requires a re-chargeable high capability lithium battery.

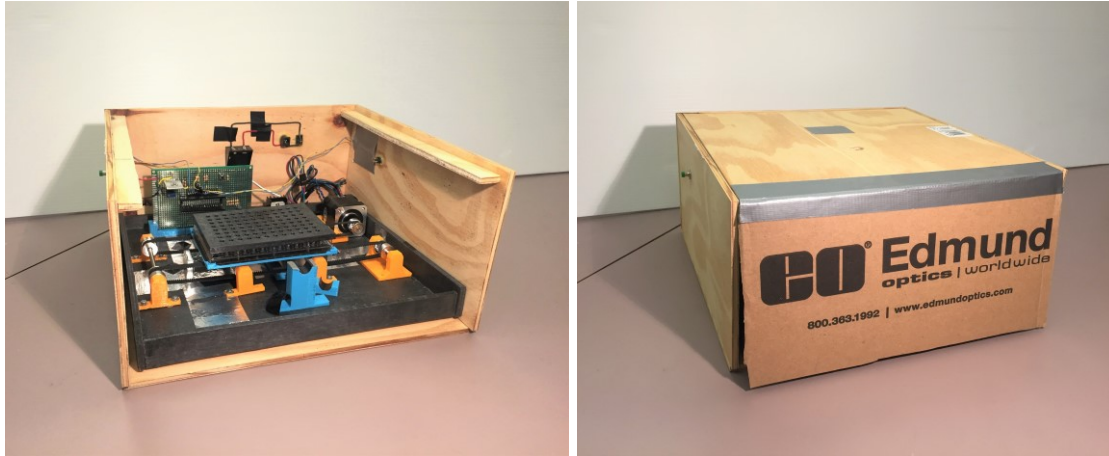


Figure A.1: Preliminary prototype of a customized smartphone based 96 well plate reader

Details of the inner compartment of the device can be better visualized in Figure mm. It contains a motor controlled linear stage allowing the 96 well plate move back and forth. The input light source module is placed horizontally on one side of the plate creating a right-angle to the observation direction from top. With this setup, background noise picked up by the detector is minimal (see Section 3.3.2 for detailed explanations), therefore creating the possibility to monitor the output signal directly with a smartphone camera. However, the trade-off with the right-angle setup is to omit the rest 7 rows during each experiment, making the efficiency lower than traditional setup. Moreover, a plate mask is designed to reduce the interference between adjacent wells.

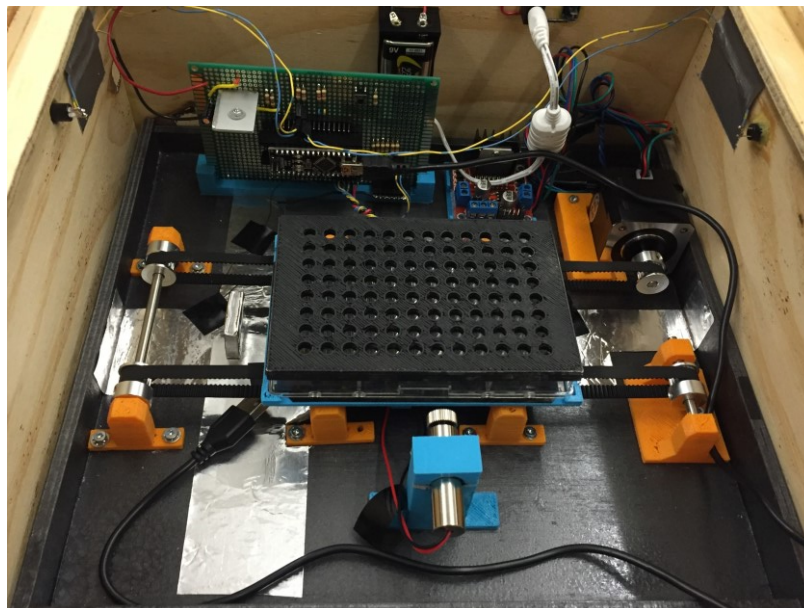


Figure A.2: Customized plate mask

Well Position Index	Molar Concentration
1	100mM
2	10mM
3	1mM
4	100uM
5	10uM
6	1uM
7	100nM
8	10nM
9	1nM
10	100pM
11	10pM
12	water

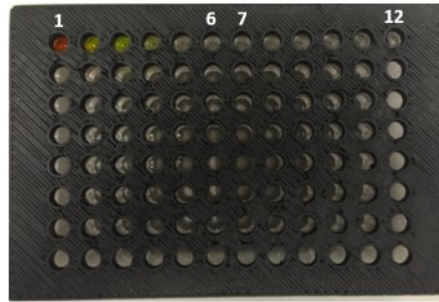


Figure A.3: Fold-10 serial dilution of fluorescein, starts from 100mM

Appendix B.

Determining the Optimized System Parameters for Image Acquisitions

To investigate the behavior of G/B ratio and grey scale value measurement approaches under different LED power, ISO setting and exposure time, three sets of tests were conducted, and the results are plotted in Figure 1-3 respectively. In each test, the fluorescence intensities of a 1 μ M and a 10 μ M fluorescein sample are measured using two approaches under the test condition that only one quantity of the three changes and the other two remain fixed. The images are acquired with iPhone 6s.

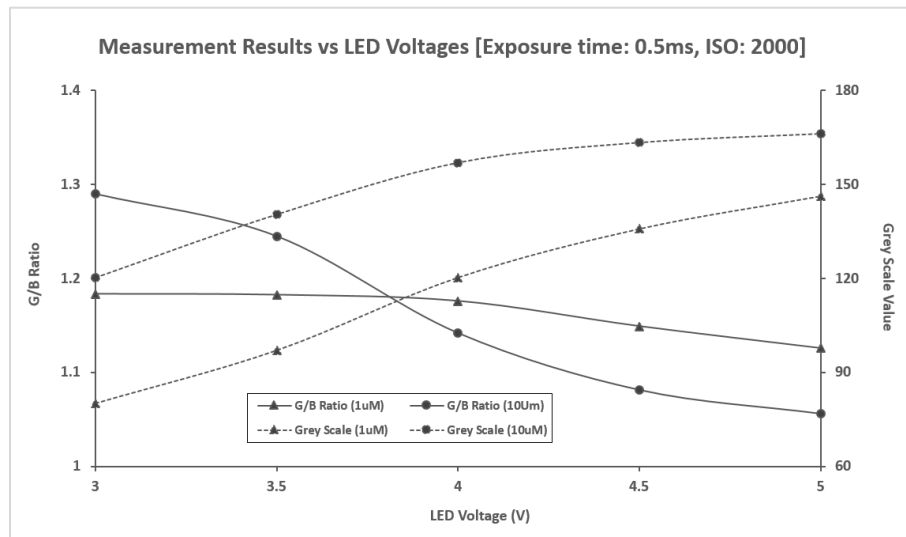


Figure B.1: System output reading vs. LED intensity, exposure time and ISO setting are fixed

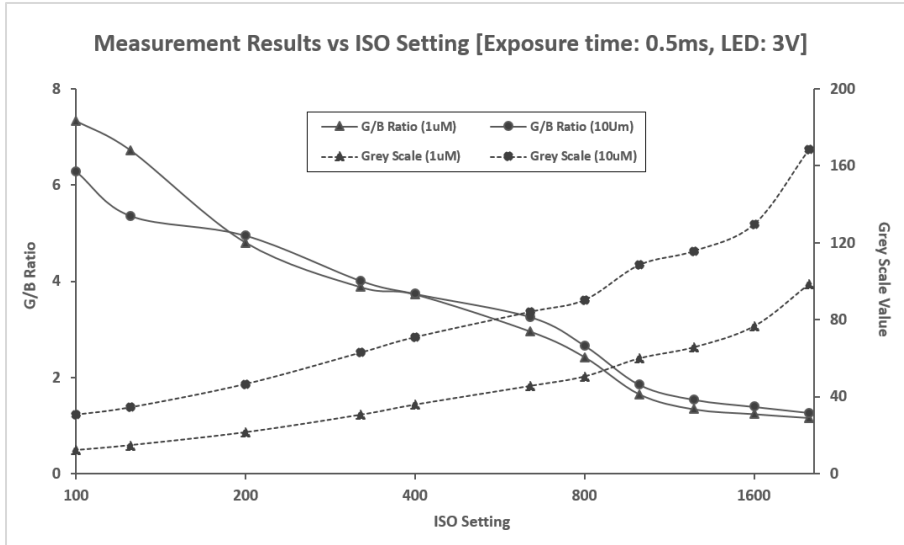


Figure B.2: System output reading vs. ISO setting, exposure time and LED intensity are fixed

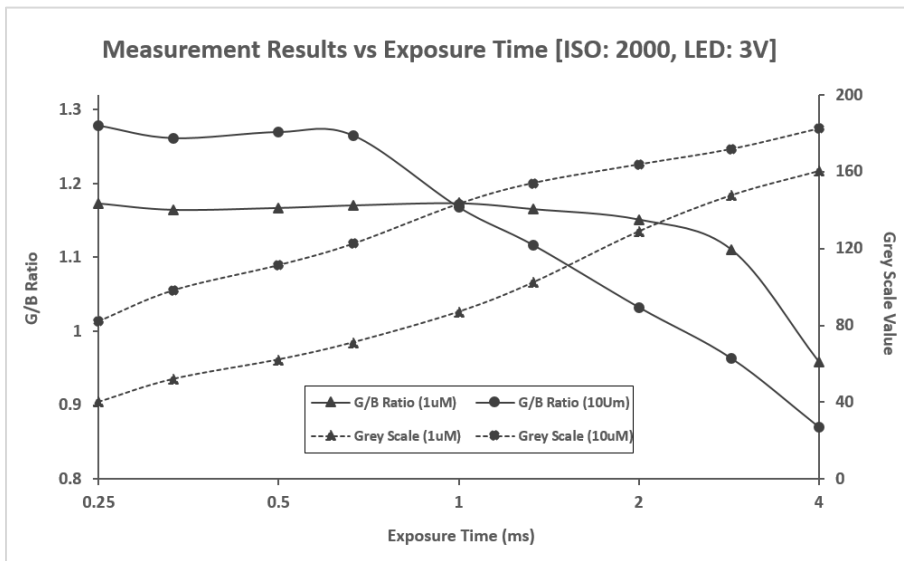


Figure B.3: System output reading vs. exposure time, LED intensity and ISO setting are fixed

Increasing any system parameters will result a larger irradiance received by the image sensor, therefore we observed a positive relationship between grey scale value and any of the system parameter setting. To minimize measurement errors, the system parameters including LED intensity, ISO and exposure time must be strictly fixed to global constant values for all measurements using this approach.

The other measurement approach, G/B ratio, is more immune to the changing of parameter setting. While taking the ratio of two most responsive color channels, the change of photonic energy received by each color channel can be significantly canceled. From the three plots above, the following settings are appropriate range for this measurement approach.

{LED: 3V, ISO Setting: 2000, Exposure Time: 0.25ms to 0.6ms}

Appendix C.

Calibration of Spectral Sensitivity of iPhone 6

An optical experiment was conducted to approximate the spectral sensitivity of the smartphone camera (iPhone 6). The experimental setup is illustrated in Figure C.1 (a). The laser was a tunable laser (WhiteLase micro) and emitted a monochromatic beam to a cardboard (screen1). The wavelength of the beam was tuned from 405nm to 705nm with 20nm interval. Since the laser intensity is relatively high which can easily saturate the color channels, we used a glass slide which was placed in 45 degrees to the beam path to reflect a small portion of light onto another cardboard (screen2), as shown in Figure C.1(b), the light dot on the reflected beam is much weaker.

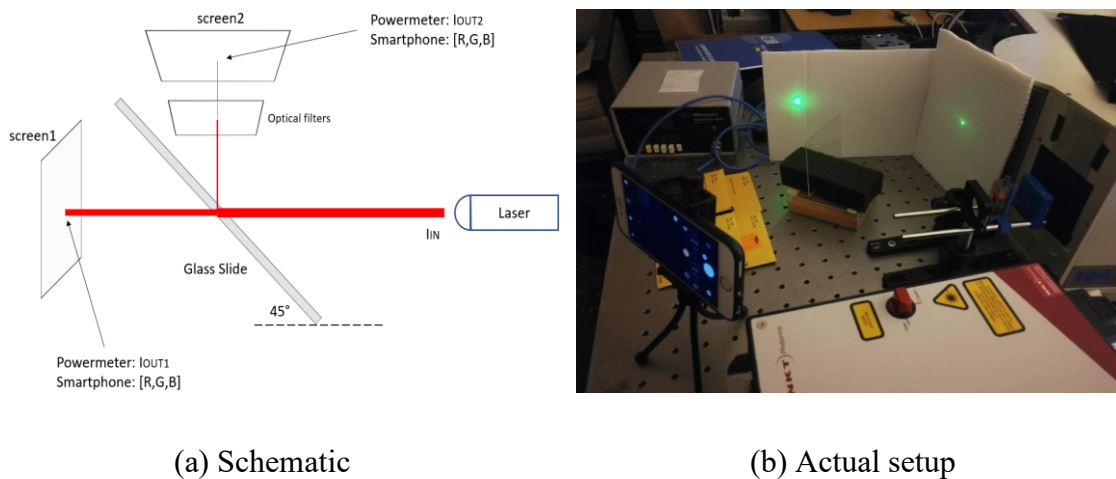


Figure C.1: Setting up the smartphone spectral sensitivity test

Power intensity is another parameter need to be considered. Since the Laser does not produce uniform intensity across the wavelengths, we used different combinations of neutral density filters with different optical densities (OD) to equalize the intensity at each wavelength. In practice, the intensity at each wavelength is kept at $25 \pm 5\mu\text{W}$, and the combination of ODs are listed in Table C.1.

Wavelength (nm)	Intensity (uW)	Optical Filter Combination
405	23.8	OD1+OD0.4
425	27.4	OD1
445	24.6	OD1
465	22.9	OD1
485	26.3	OD0.4+OD0.4
505	19.7	OD0.4+OD0.4
525	19.2	OD0.4
545	30.4	N/A
565	27.7	N/A
585	26.4	N/A
605	28.2	N/A
625	30.2	N/A
645	21.9	N/A
665	22.5	OD0.4
685	25.9	OD0.4
705	28.3	OD0.4

Experimental Setup:

The experimental setup parameters are listed as followings:

Tuner: SuperK VARIA

Laser: WhiteLase micro (laser) 400 to 2000nm

Smartphone: iPhone 6

Camera setting: ISO:32, exposure time: 1ms (to prevent saturation)

Other apparatus: Use glass slide to split the light.

Using this setup and measurement data, the spectral sensitivity of iPhone 6 from 400nm to 700nm is plotted in Figure C.2.

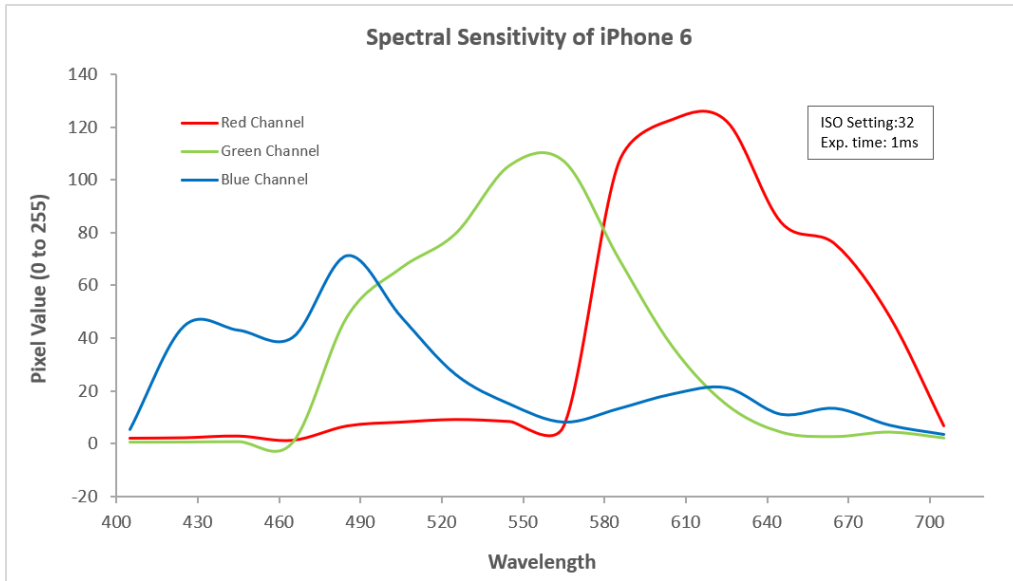


Figure C.2: Spectral sensitivity plot of iPhone 6

Additional, we plotted the channel ratio and grey scale value in Figure C.3 and Figure C.4 respectively. As shown in Figure C.3, using G/B ratio, the sensitivity reaches maximum at around 550nm, which overlaps the spectrum of fluorescent light of the sample, thus can be mainly use for fluorescence measurement. In Figure C.4, the sensitivity using Grey Scale method is relatively flat and uniform across the entire visible range, therefore will be mainly used for absorption/scattering based measurement mentioned in Chapter 5.

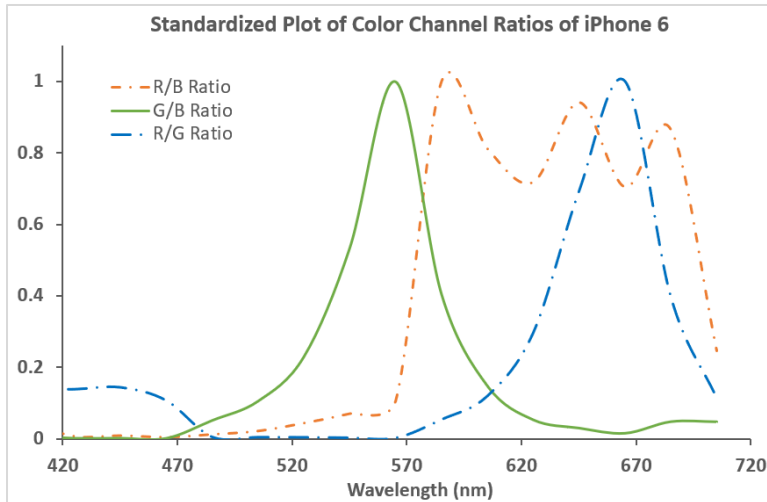


Figure C.3 Channel ratio plot versus wavelength

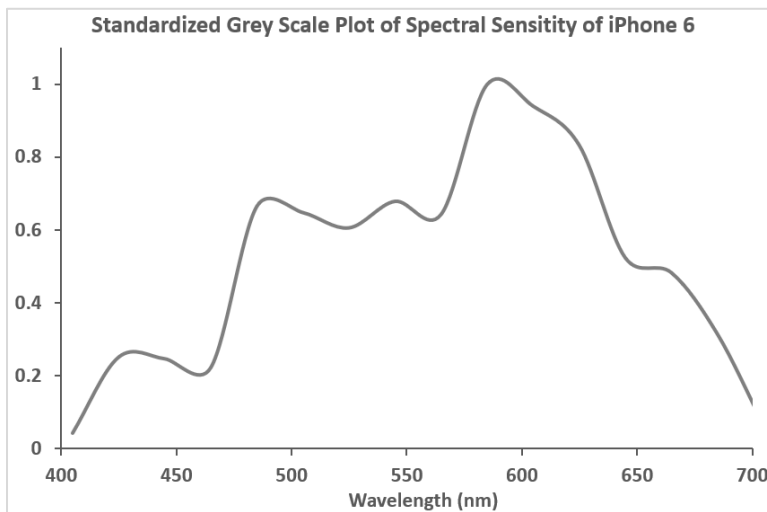


Figure C.4 Grey Scale Value plot versus wavelength

Appendix D.

Design of Automated Smartphone Imaging System

Figure D.1 shows the model for a cuvette-based imaging system. This device is mainly composed by four parts: a rotation disk, a cylindrical housing, top cover and control electronics. The rotation disk has rooms for 8 standard cuvettes. Light interference among adjacent cuvettes can be eliminated by the isolator placed in between. Rotation is precisely controlled by the stepper motor and the control electronics placed underneath. The disk rotates 45 degrees for each step. Both disk and control electronics are securely mounted onto the cylindrical housing. Light source, which is made as a replaceable module, is also installed on the side wall to form a right-angle illumination-detection layout. During operation, the system will be covered by the top cover to completely block external backlight, and a smartphone that is set to video recording mode will be placed onto the top cover.

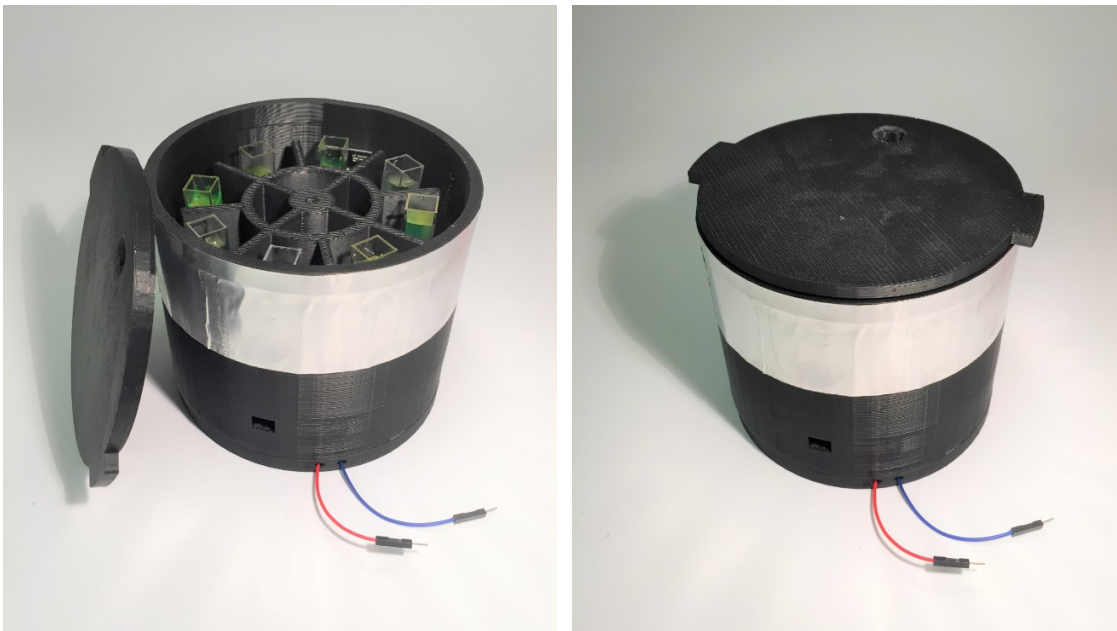


Figure D.1: A preliminary prototype of cuvette based smartphone imaging device